A DYNAMIC FLOTATION MODEL FOR REAL-TIME CONTROL AND OPTIMISATION

by

Daniël Jacobus Oosthuizen

Submitted in partial fulfillment of the requirements for the degree

Philosophiae Doctor (Electronic Engineering)

in the

Department of Electrical, Electronic and Computer Engineering

Faculty of Engineering, Built Environment and Information Technology

UNIVERSITY OF PRETORIA

February 2023

SUMMARY

A DYNAMIC FLOTATION MODEL FOR REAL-TIME CONTROL AND OPTIMISATION

by

Daniël Jacobus Oosthuizen

Promoter:	Prof. I.K. Craig
Co-promotor:	Prof. J.D. le Roux
Department:	Electrical, Electronic and Computer Engineering
University:	University of Pretoria
Degree:	Philosophiae Doctor (Electronic Engineering)
Keywords:	Flotation, model predictive control, modelling, moving horizon estimator, observability, optimisation, process control, process optimisation, simulation, state and parameter estimation

Froth flotation models that are developed for circuit design applications are often not suitable for model-based dynamic control and optimisation applications. For real-time control and optimisation applications dynamic models of the key flotation mechanisms are required, as these use real-time measurements to update internal model states and estimate model parameters in real-time.

The development of a dynamic froth flotation model is described, based on a combination of fundamental mass and volume balances, fundamental steady-state froth models and empirical models for bubble size and air recovery. The model outputs are defined to correspond with real-time measurements that are commonly available on industrial flotation circuits, including measurements from froth imaging devices in combination with measurements of levels, flow rates, densities and grades.

The flotation model is analysed for state observability and controllability, and it is shown that the model states and parameters can be estimated from real-time process measurements that are commonly available on industrial flotation circuits. The ability to estimate process parameters in real-time opens up opportunities for improved process control and optimisation by compensating for a specific flotation

mechanism rather than the combined effect of multiple flotation mechanisms. The speed of response can also be improved when more accurate models are maintained by continuously updating model parameters.

The flotation model, a state and a parameter estimator and model predictive controller are combined to simulate the potential benefits of using a non-linear model-based approach with state and parameter estimation capabilities in a dynamic control and optimisation application on flotation circuits. The strategy is shown to reject typical process disturbances effectively in the presence of process noise and outperforms a linear non-model based control strategy by a significant margin.

OPSOMMING

'N DINAMIESE FLOTTASIE MODEL VIR INTYDSE BEHEER EN OPTIMERING

deur

Daniël Jacobus Oosthuizen

Promotor:	Prof. I.K. Craig
Medepromotor:	Prof. J.D. le Roux
Departement:	Elektriese, Elektroniese en Rekenaar-Ingenieurswese
Universiteit:	Universiteit van Pretoria
Graad:	Philosophiae Doctor (Elektroniese Ingenieurswese)
Sleutelwoorde:	Flottasie, modelvoorspellende beheer, modellering, optimering, prosesoptimering, prosesbeheer, simulasie, skuiwendehorisonberaming, toestand- en parameterberaming, waarneembaarheid

Skuimflottasie modelle wat vir aanlegontwerpdoeleindes ontwikkel is, is dikwels nie geskik vir dinamiese modelvoorspellende beheer- en optimeringstoepassings nie. Dinamiese modelle van die belangrikste flottasie meganismes word benodig vir intydse beheer- en optimeringstoepassings, omdat hulle intydse meting gebruik om interne modeltoestande en -parameters intyds by te werk.

Die ontwikkeling van 'n dinamiese skuimflottasie model word beskryf, gebaseer op 'n kombinasie van fundamentele massa- en volumebalanse, fundamentele bestendigetoestand-skuimmodelle en empiriese modelle om borrelgroottes en die behoud van lug te beskryf. Die modeluitsette is gedefinieer om ooreen te stem met intydse metings wat algemeen beskikbaar is van flottasiekringe, insluitende metings van skuimbeeldingsapparate, saam met metings van vlakke, vloeitempo's, digthede en grade.

Die toestandwaarneembaarheid en -beheerbaarheid van die flottasie model is ondersoek, en daar is aangedui dat die modeltoestande en -parameters beraam kan word op grond van intydse prosesmetings wat algemeen beskikbaar is op industriële flottasiekringe. Die vermoë om prosesparameters intyds te beraam, skep geleenthede om prosesbeheer en -optimering te verbeter deur te kompenseer vir 'n

spesifieke flottasiemeganisme eerder as vir die oorkoepelende effek van veelvuldige flottasiemeganismes. Die reaksietyd kan ook verbeter word wanneer meer akkurate modelle in stand gehou word deur modelparameters deurlopend by te werk.

Die flottasie model, ’n toestand- en parameterberamer en ’n modelvoorspellende beheerder is gekombineer om die potensiële voordele van ’n nie-lineêre modelgebaseerde benadering met toestand- en parameterberamingsvermoëns te simuleer as ’n dinamiese toepassing vir skuimflottasiekringe. Daar is aangetoon dat die strategie tipiese prosessteuringe effektief verwerp in die aanwesigheid van prosesruis, en ’n lineêre nie-modelgebaseerde beheerstrategie beduidend oortref.

ACKNOWLEDGEMENTS

Special thanks is due to my supervisors, Prof. Ian Craig and to Prof. Derik le Roux for their guidance, feedback and support throughout this work.

I would like to thank Dr Kathryn Hadler and Prof. Jan Cilliers from Imperial College London for sharing information and making the industrial data used in this study available. This shaped a key part of this research that would not have been possible otherwise.

I'd like to acknowledge Capstone Editing for providing copyediting and proofreading services of a high standard.

To my wife, Tina, and children, Karla and Jacobus: Thanks for your patience, support and the endless supply of coffee, which is always accompanied with a smile.

Finally, I wish to thank our Heavenly Father for the talents, opportunities and the people who have been part of this journey with me and throughout my life.

LIST OF ABBREVIATIONS

HMPC	hybrid model predictive controller
MHE	moving horison estimator
MPC	model predictive controller
PAR	peak air recovery
PDF	probability density function
PGMs	platinum group minerals
PI	proportional integral
PID	proportional integral derivative

TABLE OF CONTENTS

LIST OF FIGURES

LIST OF TABLES

CHAPTER 1 INTRODUCTION

1.1 BACKGROUND

Mineral processing plants typically include unit-processes for crushing, grinding, classification, separation and refining the mined ore. The crushing and grinding units reduce the ore size, with the aim of liberating valuable minerals from the bulk or gangue minerals. Crushing and grinding units often operate in a closed-loop configuration with classification units, such as screens or hydrocyclones, where coarse materials are recycled for further crushing or grinding, while fine materials are processed in downstream separation processes, such as flotation or leaching. The ideal size distribution of the ore sent to the separation process depends on the ore mineralogy and the separation process that is used. For more complex ore types, multiple stages of separation and regrinding may be required, with regrind mills between different flotation units (Wills and Napier-Munn, 2006). The flotation process can be followed by leaching, smelting or refining unit processes, lumped together under the heading *refining* in Figure 1.1.

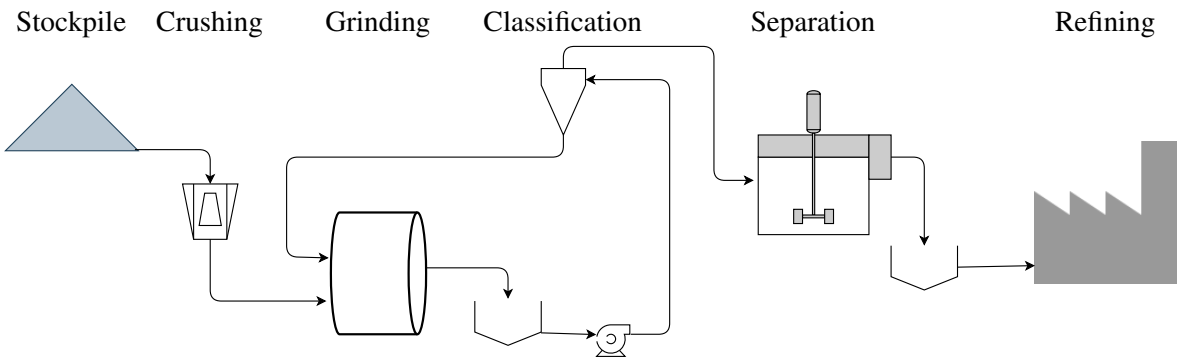

Figure 1.1. Unit processes in a mineral processing plant.

Froth flotation is a versatile mineral processing technique that utilises differences in surface properties to separate valuable and undesired (gangue) minerals. These differences in surface properties can be

enhanced using different reagents. Since the first froth flotation applications in the 1880s, flotation machines have grown in size and efficiency to meet increasing production demands and process ores with more complex mineralogy and declining feed grades. The range of froth flotation applications is no longer limited to the original objective of treating hydrophobic sulphide ores of copper, lead and zinc but now include platinum, nickel, coal and oxidised minerals. Without froth flotation, it would not have been economically viable to process many of the low-grade and complex ore types that are mined today (Wills and Napier-Munn, 2006; Gaudin, 1957).

A schematic diagram of a froth flotation cell is shown in Figure 1.2. A pulp containing liberated minerals is mixed with reagents and transferred to a flotation cell, where it is brought in contact with air bubbles that are injected at the bottom of the flotation cell. The surface properties of hydrophobic minerals result in these minerals attaching to the air bubbles that rise to the top of the flotation cell through the mechanism of 'true flotation', and a layer of froth forms at the top of the flotation cell with a higher concentration of the desired hydrophobic minerals than the pulp. Through the mechanism of 'entrainment', the rising stream of bubbles entrains pulp (containing the desired and gangue minerals) as part of the liquid trapped between the bubbles. Froth characteristics—such as froth stability, bubble size distribution, froth depth and, in some cases, wash water—can be manipulated to reduce the contamination due to entrainment in the froth. 'Entrapment' of unwanted gangue minerals still occurs, where mineral particles that are not attached to a bubble remain trapped within the froth structure and report to the concentrate stream. Weakly floatable gangue minerals could also report to the froth layer through the mechanism of 'true flotation', and imperfect liberation results in individual particles—containing both desired and undesired minerals—reporting to the froth layer. The froth layer overflows into a concentrate launder, from where it can either report to the final concentrate stream or be processed further in other flotation units. The stability of the froth layer as described by the air recovery (the fraction of air injected into the flotation cell that overflows as part of the concentrate stream) plays an important role in optimising the operation of individual flotation cells (Wills and Napier-Munn, 2006; Gaudin, 1957; Hadler, Smith and Cilliers, 2010a).

The objectives of the flotation process are to produce a concentrate of a desired grade (with an acceptable level of impurities) and minimise the amount of valuable minerals lost to the tailings stream. A single flotation cell can usually not meet both these requirements. Banks of multiple flotation cells, with concentrate flows and recycle streams in different configurations, are required to provide adequate cleaning of the concentrate and scavenge any remaining valuable minerals from the pulp before the

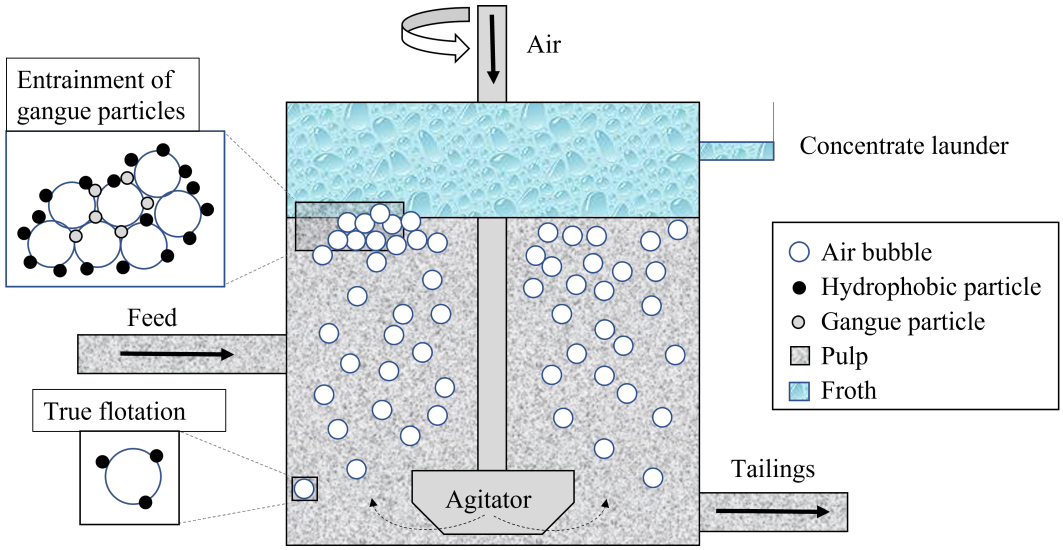

Figure 1.2. Schematic diagram of a flotation cell.

final tailings stream is disposed of in a tailings storage facility. The design of the flotation circuit and the operation of the individual units are complex processes, which require an understanding of flotation mechanisms, interactions between units, the effect of different manipulated variables on the process, and the economic impact of the control actions that are taken (Wills and Napier-Munn, 2006; le Roux, Steinboeck, Kugi and Craig, 2017).

Figure 1.3 illustrates the concept of different grade-recovery curves for a single flotation cell, with grades plotted on the x-axis and recovery plotted on the y-axis. The ore mineralogy and degree of liberation dictate the maximum concentrate grade that can be achieved. For example, the maximum copper concentrate grade that can be achieved for chalcopyrite ($CuFeS_2$) as an ore mineral is approximately 34.5% (Wills and Napier-Munn, 2006), assuming perfect liberation. The feed grade determines the lower boundary on the concentrate grade, which would be reached when the feed bypasses the concentrator and reports directly to the concentrate stream. Recovery refers to the fraction of the total desired mineral or element contained in the ore that is recovered to the concentrate. Theoretically, given infinite time, perfect liberation, an ideal size distribution and a suitable reagent mixture, 100% of the desired element can be recovered in the concentrate at the maximum grade as dictated by the ore mineralogy. The dotted line in Figure 1.3 can thus be considered a 'theoretical optimum grade-recovery curve'. On an industrial flotation cell, a 'practical grade-recovery curve' will always achieve a lower recovery at the same grade as the 'theoretical optimum grade-recovery curve', as the pulp residence time in the flotation cell (largely determined by the feed flow rate) will be finite and some slow floating

or non-liberated minerals will not be recovered. The 'practical grade-recovery curve' that is achieved is not only a function of the feed rate and size distribution but also of other operating parameters that include reagents, froth depth, air addition rate and pH of the pulp. Therefore, the aim of a flotation control and optimisation strategy should be to stabilise the process at a grade that will produce the most economical return for the throughput and select operating parameters that will result in a 'practical grade-recovery curve' with the highest mineralogical efficiency (Wills and Napier-Munn, 2006). Where the pulp or concentrate from one flotation cell flows to another cell, the grade and recovery ranges of the downstream cell would be a function of the feed from the upstream cell and hence, the operating parameters of the upstream cell.

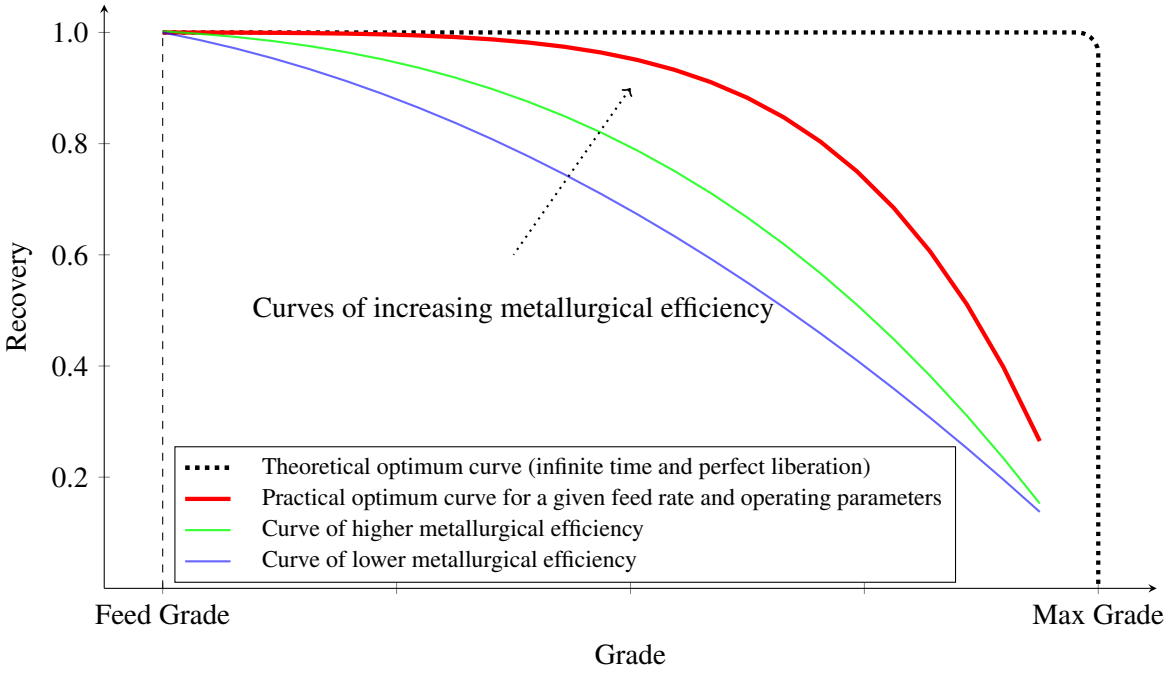

Figure 1.3. Grade-recovery curves for a flotation cell.

1.2 PROBLEM STATEMENT

Flotation optimisation strategies have been applied successfully on industrial sites. In most cases, the optimisation strategies focused on optimising a limited set of variables—often a single variable—without taking interactions between variables and non-linearities into account. Maldonado, Sbarbaro and Lizama (2007) calculated the optimum flotation cell level profile down a bank of flotation cells, but modelled the concentrate flow rates as a linear function of froth depth. In other studies, Shean, Hadler and Cilliers (2017) and Hadler and Cilliers (2009) optimised the air recoveries of individual flotation cells by finding the peak in air recovery from the non-linear response of each flotation cell, but did not manipulate the levels of flotation cells. Saffy, Mashakane and Hopstadius (2019) described

a dynamic grade optimisation strategy that used linear controllers to manipulate both flotation cell level and air setpoints without explicitly considering non-linearities in air recovery. While these strategies (Maldonado *et al.*, 2007; Shean *et al.*, 2017; Hadler and Cilliers, 2009; Saffy *et al.*, 2019) can drive the flotation process closer to an optimum operating point for a given set of operating conditions, a model-based approach that combines the effect of multiple manipulated variables and takes non-linearities into account is likely to outperform each strategy when it is used in isolation.

An aspect that negatively impacts the performance of controllers and optimisers is the long-term reliability of the models that are used. Phillpotts, Whitehead and Ramatsoma (2021) highlighted that flotation characteristics change rapidly over time and that a slow optimum-seeking algorithm may not be able to optimise air recovery. Gradual changes in process characteristics over time could partially explain why flotation control and optimisation strategies based on froth image-processing often show promise during a trial period but fail to deliver long-term benefits (Aldrich, Marais, Shean and Cilliers, 2010). Flotation models used in design and optimisation strategies (Bascur and Herbst, 1985) usually have parameters that need to be fitted to empirical models, which require extensive sampling campaigns beyond the scope of the routine sampling that is performed on flotation circuits. With rapid changes in process and feed characteristics, any strategy that depends on empirical parameters runs the risk of a degradation in performance until another sampling campaign is performed to update parameters. It is thus important that a flotation model used for dynamic optimisation does not depend on infrequent sampling campaigns to update the model parameters but has the ability to adapt its parameters based on measurements that are available in real time.

The definition of the objective function as part of an optimisation strategy is a critical component of the optimisation strategy. Examples are available in the literature where subtle variations in the objective function—for example, maximising concentrate grade vs. minimising tailings grade—can have a major impact on the resulting performance (Maldonado *et al.*, 2007; Seguel, Soto, Krommenacker, Maldonado and Becerra Yoma, 2015). Rather than defining optimisation objectives in terms of derived measurements, a model directly modelling the physical quantities that need to be optimised is preferable and needs to be developed.

1.2.1 Context of the problem

It is accepted in industry that a flotation circuit needs to be stabilised before optimisation can be attempted. Several examples of industrial applications where a model-based approach to level stabilisation was implemented have been documented. Simple models can be used to compensate for interactions between interconnected flotation cells to avoid the effect of a disturbance in an upstream cell from propagating to downstream cells. Industrial applications where aeration rates to flotation cells, pulp level setpoints and reagent addition rates are manipulated to obtain a desired concentrate mass pull or grade in a concentrate or tailings stream are well documented. In most cases, models used in grade or mass pull applications are empirical due to complex, non-linear and often time-varying relationships (Jämsä-Jounela, Dietrich, Halmevaara and Tiili, 2003; Schubert, Henning, Hulbert and Craig, 1995; Saffy *et al.*, 2019).

Air recovery provides a mechanism to optimise individual flotation cells by taking non-linearities in froth characteristics into account. For concentration processes, an inverse relationship exists between mineral grades and recoveries. This relationship is often exploited by grade and recovery control strategies, by trading off grade for recovery to achieve a desired product specification. However, multiple combinations of aeration rates, pulp levels and reagent addition rates exist that will result in the same grade but at different recoveries. Higher recoveries at the same grade are equivalent to shifting the operating point to a more efficient grade-recovery curve rather than moving along a sub-optimal grade-recovery curve. Industrial experiments have proven that operation at the peak air recovery point maximises recovery for a given grade and, hence, optimises flotation performance in a flotation cell. The peak air recovery point has been shown to vary over time, and peak-seeking strategies to identify the peak air recovery point and operate at that point has only been applied in experimental environments (Hadler *et al.*, 2010a; Wills and Napier-Munn, 2006; Oosthuizen, le Roux and Craig, 2021; Hadler and Cilliers, 2009; Phillpotts *et al.*, 2021; Shean *et al.*, 2017).

Different approaches have been taken to optimise sections of flotation circuits. Maldonado *et al.* (2007) and Seguel *et al.* (2015) used a model-based approach to optimise the flotation cell level profile down a flotation bank. Different circuit configurations and operating points can be compared using simulation packages such as the JK Sim Float (Schwarz, Alexander, Whiten, Franzidis and Harris, 2006), which is based on steady state models and relies on data that are collected from sampling campaigns. Bascur and Herbst (1985) modelled the transfer of particles between the pulp and froth phases based on empirical and phenomenological models and applied the models in industrial implementations. Image

processing has been used in experimental trials to classify and control froth characteristics but has not delivered long-term benefits (Aldrich *et al.*, 2010). Flotation plants would often have well-defined targets on grade and recovery that can be automated, as described by Saffy *et al.* (2019). However, the targets are typically fixed based on design specifications and are often not adjusted automatically when the feed composition changes or other operating conditions change.

The mineral concentration in flotation cells and froth characteristics vary dynamically due to variations in feed rates and compositions, selective flotation and the transfer of pulp between flotation cells. Froth stability has been shown to change dynamically over a short time span (Phillpotts *et al.*, 2021) and depends on the mineral content in the froth. None of the techniques described above uses a comprehensive flotation model covering non-linear aspects, such as air recovery, to dynamically optimise the flotation operation. In addition, most of the methods that have been described above rely on extensive sampling campaigns to fit model parameters before the model can be used for optimisation. Previously developed optimisation models are potentially only valid over a limited operating range and require frequent refitting of model parameters to ensure that they remain representative of the actual flotation process.

1.2.2 Research gap

No dynamic froth flotation model for dynamic control and optimisation applications is currently available, that:

- include interactions between the froth and pulp phases in a flotation cell
- include interactions between different flotation cells in a flotation circuit
- include non-linear froth dynamics related to air recovery
- adapt to variations in ore characteristics rather than rely on sampling campaigns for model fitting.

1.3 RESEARCH OBJECTIVE AND QUESTIONS

The objective of this study is to develop a dynamic froth flotation model that can be used in dynamic control and optimisation applications of flotation circuits. To meet this objective, the flotation model must meet the following criteria:

- A dynamic model is required that takes interactions between flotation cells and between different phases inside the flotation cell into account.

- The flotation model must not rely on extensive modelling campaigns to fit model parameters but adapt its model parameters based on real-time measurements that are typically available on industrial flotation installations.
- The model must include non-linearities in froth characteristics and include these non-linearities in the optimisation problem.

Four research questions need to be answered to meet this objective:

- Which key dynamics in the froth flotation process need to be included in a simple dynamic flotation model for real-time process control and optimisation purposes?
- What instrumentation, which is commonly available, or can readily be obtained, on industrial flotation circuits can provide continuous real-time measurements?
- Which process states and model parameters can be estimated from such a dynamic model, using commonly available real-time measurements or measurements that can readily be obtained in real time?
- What potential benefit can be derived by implementing a dynamic flotation model in a dynamic control and optimisation application?

1.4 APPROACH

A literature study is conducted to identify:

- the key flotation variables and interactions that need to be included in a dynamic flotation model,
- flotation models that are available in the literature, that can potentially be included in a dynamic froth flotation model, and
- real-time measurements that are commonly available on industrial flotation circuits.

A dynamic flotation model is developed by combining existing models available in the literature. Where suitable models are not available, new models are derived. The objectives of developing a dynamic model that does not depend on sampling campaigns to estimate model parameters form an integral part of the selection of a model structure and sub-models.

The model development is followed by a state observability and controllability analysis. The state observability analysis also includes the identifiability of model parameters to confirm that model

parameters can be estimated from real-time measurements that are commonly available on industrial flotation circuits. The state controllability analysis determines if the model inputs can be used to drive the model states to desired setpoints.

Once the model has been developed, model parameters are fitted to ensure that model outputs correspond with measurements that have been obtained on an industrial flotation plant. Non-linear characteristics of the model outputs are highlighted to indicate potential areas where the use of the model could be beneficial. The flotation model with parameters fitted on industrial data is used as a simulator of the plant in subsequent work.

Finally, a model predictive controller (MPC) is designed to evaluate the benefit of using a non-linear flotation model as part of a model-based control strategy, compared to a linear classical control strategy, as is often used in industry.

1.5 HYPOTHESES

The focus of this work is summarised in two hypotheses:

- Key parameters that characterise different flotation mechanisms can be estimated in real-time, using only measurements from instrumentation that are commonly available on industrial flotation circuits.
- A model-based automatic control strategy with real-time estimates of key flotation parameters would outperform a non-model-based control strategy with fixed parameters, by consistently achieving a higher recovery at the same grade.

1.6 RESEARCH GOALS

This work has two main goals:

- to develop a dynamic froth flotation model that can be used in control and real-time optimisation applications
- to demonstrate the benefits of using a model-based approach to flotation optimisation by comparing it to classical control techniques.

1.7 RESEARCH CONTRIBUTION

Many froth flotation models available in the literature have been applied successfully in laboratory, pilot plant or industrial applications. Comprehensive flotation models covering interactions between different phases in the flotation process and between interacting cells are often aimed at plant design and thus use steady-state models. Other models only focus on a single aspect of froth flotation (e.g., froth characteristics or the floatability of hydrophobic particles through the mechanism of true flotation) without taking variability in other phases of froth flotation into account. The third limitation of existing models is that the models often rely on data obtained from extensive sampling campaigns, and these data may not be readily available on a real-time basis. As process conditions and feed materials change over time, model accuracy tends to deteriorate, until such time that a follow-up sampling campaign is conducted that allows models to be updated.

The contribution of this thesis is to develop a dynamic froth flotation model that includes key flotation mechanisms in the pulp and froth phases. The model will only use real-time measurements that are commonly available on industrial flotation circuits to update its modelled parameters to ensure that the model is representative of actual plant characteristics at all times.

1.8 RESEARCH OUTPUTS

The result of a literature survey on froth flotation models, measurements that are available on industrial flotation plants, and the use of model-based control in froth flotation has been published in the following:

- Oosthuizen, D. J., Craig, I. K., Jämsä-Jounela, S. L. and Sun, B. (2017). On the current state of flotation modelling for process control, *IFAC-PapersOnLine*, **50**(2): 19–24.

As part of the model development, simulation studies were done to compare different approaches to include floatability characteristics in a flotation model and show the potential benefits of using a non-linear flotation model in optimisation applications. The results of these simulation studies have been published in:

- Oosthuizen, D. J. and Craig, I. K. (2018). Flotation modelling based on floatability distributions regressed from routine data, *IFAC-PapersOnLine*, **51**(21): 105–110.

- Oosthuizen, D. J. and Craig, I. K. (2019). Predicting optimal operating points by modelling different flotation mechanisms, *IFAC-PapersOnLine*, **52**(14): 60–65.

A description of the flotation model that was developed for this thesis, including state observability and state controllability analyses, has been published in:

- Oosthuizen, D. J., le Roux, J. D. and Craig, I. K. (2021). A dynamic flotation model to infer process characteristics from online measurements, *Minerals Engineering*, **167**: Article 106878.

The design of an MPC controller that uses the model described in Oosthuizen *et al.* (2021) and a study of the potential benefits of the non-linear MPC over classical control strategies has been submitted as:

- Oosthuizen, D. J., le Roux, J. D. and Craig, I. K. A model predictive control strategy to maximise flotation recovery by dynamically adapting to variability in air recovery (submitted to *Minerals Engineering*).

1.9 OVERVIEW OF THE STUDY

Chapter 2 covers a literature review on flotation modelling and control applications and types of instrumentation that are commonly available on industrial flotation plants. In Chapter 3, the flotation model is developed using existing sub-models from the literature where available and by deriving new models where required. Chapter 4 shows the state observability and controllability analyses of the flotation model to confirm that model parameters and states can be estimated from measurements commonly available on industrial flotation plants. An MPC design using the flotation model described in Chapter 3 is shown in Chapter 5. Chapter 5 also shows simulation results to compare the performance of the MPC controller to a classical controller implementation. In Chapter 6, the results are summarised and discussed, and concluding remarks are given.

CHAPTER 2 LITERATURE REVIEW

2.1 INTRODUCTION

The origins of froth flotation can be traced back to the 1880s (Gaudin, 1957). Froth flotation was patented in 1906 and column flotation was patented in the early 1960s (Finch and Dobby, 1990; Wills and Napier-Munn, 2006). Froth flotation has been modelled extensively to include factors such as the chemical reactions (King, 1982), how different size classes participate in the process (Lynch, Johnson, Manlapig and Thorne, 1981) and the physical processes, such as particle-bubble collision (Finch and Dobby, 1990). Collaboration between industry and academia—in programs such as AMIRA P9—has enabled efforts to be focussed on the topic, and significant progress has been made during the past 25 years in understanding the intricacies of the froth flotation process. As a result, many of the principles described earlier have been integrated into comprehensive simulators, such as the simulators described by Schwarz *et al.* (2006) and Bouchard, Desbiens and Del Villar (2014).

Despite the rich modelling framework available, the number of successful industrial implementations of model-based control and optimisation strategies (other than basic level control, as described by Schubert *et al.* (1995)) remains scarce (Shean and Cilliers, 2011). Reasons for the limited number of industrial implementations include a lack of instrumentation, a lack of reliable dynamic models and inadequate regulatory control (Bergh and Yianatos, 2011). The issues of the lack of suitable dynamic models and insufficient instrumentation to interface with the models cannot be separated and need to be addressed simultaneously.

Model-based controller implementations often fall into disuse after some time due to the models not being robust over a large range of operating conditions (Shean and Cilliers, 2011). The use of empirical models that have been fitted over a limited operating range has similar limitations and requires frequent recalibration when the operating points shift (Bouchard, Desbiens, del Villar and Nunez, 2009). In

the absence of real-time measurements to update these models automatically, or at least to alert the operator of the need for recalibration, the accuracy of the models would deteriorate to a point where control strategies based on the inaccurate models would fail.

The aim of this chapter is to identify the key variables required in flotation control applications, identify existing models that take these key variables into account and consider to what extent real-time measurements required by these models are commonly available on froth flotation plants or are being developed and can potentially be made available on industrial sites in future. The focus is on long-term continuous control of industrial processes rather than short-term pilot plant campaigns.

Section 2.2 discusses the key variables that need to be included in a froth flotation model. Section 2.3 investigates the instrumentation that is commonly available on industrial flotation circuits and considers instrumentation that has been developed but that is not commonly available in industry. Section 2.4 discusses different froth flotation models that are available in the literature and their use in model based controller implementations. Concluding remarks are made in Section 2.5.

2.2 KEY VARIABLES IN FLOTATION MODELLING

A number of authors have listed the key variables that are required in the control of froth flotation processes for example, Finch and Dobby (1990), Lynch *et al.* (1981), Bergh and Yianatos (2011) and Laurila, Karesvuori and Tiili (2002). There is, to a large extent, agreement on the set of variables that needs to be considered. As inputs, or manipulated variables, the following variables can be used to drive the process in a desired direction:

- reagent additions
- pulp level setpoints
- air flow rate setpoints
- froth wash water rate (most common in columns).

Lynch *et al.* (1981) also included reagent addition valve locations and the selection of concentrate streams to combine in concentrate hoppers, but these form part of circuit design parameters rather than real-time control parameters. This highlights how the model structure, and input and output variables are determined by the intended purpose of the model and that a model suitable for flotation circuit design may not be suitable for dynamic control applications.

Depending on the circuit configuration, feed characteristics are either considered disturbances or manipulated variables, as indicated by Lynch *et al.* (1981). Bergh and Yianatos (2011) considered pulp flow a manipulated variable rather than a disturbance, which would also be the case in integrated grinding and flotation control applications (Conradie, Bascur, Aldrich and Nieuwoudt, 2003; le Roux *et al.*, 2017). The following feed properties can be classified as manipulated variables or disturbances:

- pulp density
- volumetric feed flowrate
- fineness of grind.

The main outputs of the flotation process that capture the economic performance are grade and recovery. Lynch *et al.* (1981) also included concentrate density and concentrate flow rate in the outputs that are referred to as *performance variables*, as the total concentrate mass that is produced affects profitability.

Process states have a direct influence on the economic outputs of the process. Process states can be manipulated by changing one or more of the manipulated variables and are also affected by disturbances and states in other flotation cells. The following states, also referred to as *intermediate variables* by Lynch *et al.* (1981), need to be considered:

- froth depth
- gas holdup
- bias superficial velocity (mostly columns)
- superficial air velocity
- feed, tailings and concentrate flow rates
- mineral concentrations in all intermediate streams (grades)
- densities of all streams.

The largest discrepancy between the variables described by Bergh and Yianatos (2011) and Laurila *et al.* (2002) is in the variables that are considered disturbances. Bergh and Yianatos (2011) only included the first three disturbances listed below (including two of the feed properties listed one the previous

page, that could either be considered disturbances or manipulated variables (Lynch *et al.*, 1981), while Laurila *et al.* (2002) included all the variables in the list:

- feed size distribution
- feed grade (minerals concentration in feed)
- feed density
- feed mineralogy (fineness of crystallisation, minerals)
- electrochemical potentials (Eh, pH)
- particle properties (size distribution, shape and degree of liberation)
- froth properties (speed, bubble size distribution and stability).

A possible reason for Bergh and Yianatos (2011) not mentioning e.g. mineralogy and liberation is that their focus is on dynamic process control compared to the more general approach adopted by Laurila *et al.* (2002) that includes circuit design. The importance of electrochemical potential is also dependent on the minerals being processed and whether multiple minerals that are sensitive to variations in pH are selectively being floated. The importance of froth properties in flotation optimisation has been confirmed in experimental trials conducted by Hadler and Cilliers (2009), Hadler *et al.* (2010a), Smith, Hadler and Cilliers (2010) and Phillpotts *et al.* (2021).

The dimensions and complexity of a flotation model need to be considered for real-time control and optimisation applications. Bergh and Yianatos (2011) managed to explain 92% of the variance in a flotation process with a reduced parameter set model, by using only six latent variables obtained through principle component analysis. This confirms that a model with a small parameter set could still provide sufficient accuracy for control purposes, but the model complexity that is required to capture process dynamics with sufficient accuracy is likely to be process dependent (Laurila *et al.*, 2002). Shean and Cilliers (2011) confirmed that all the variables that have been listed in this section are not necessarily required to obtain good control performance but that their impact needs to be considered. Simplifying assumptions have been proposed—for example, that the feed distribution and density would not vary significantly if the grinding circuit control was effective (Wills and Napier-Munn, 2006). Such simplifying assumptions can potentially be used to simplify models without degrading controller performance, provided that upstream processes do not invalidate the simplifying assumptions.

2.3 INSTRUMENTATION ON INDUSTRIAL FLOTATION CIRCUITS

Reliable real-time measurements are an essential aspect of model based control strategies to ensure their long-term use (Hodouin, Jämsä-Jounela, Carvalho and Bergh, 2001). Instrumentation that is commonly found on industrial flotation circuits is described in Section 2.3.1, while other types of instrumentation referred to in the literature, which have been used in experimental or laboratory environments, are listed in Section 2.3.2.

2.3.1 Commonly available instrumentation

Laurila *et al.* (2002) provide a list of measurements that may be available on a flotation plant and highlight their limitations.

2.3.1.1 Pulp levels

Pulp levels in flotation cells or banks are commonly measured using a float with a target plate and ultrasonic level transmitter. Level measurements based on hydrostatic pressure or direct ultrasonic measurements are also available but are often troublesome or sensitive to variations in density.

2.3.1.2 Volumetric pulp flow rate

Pulp flow rates are typically measured using magnetic flow meters. The presence of suspended air bubbles cause inaccuracies, and the location and orientation of a flow meter are critical in obtaining reliable and accurate measurements. The volumetric feed flow rate from a conditioning tank to the first flotation cell in a section is often measured, but pulp flow rates between interconnected flotation cells are usually not measured due to mechanical constraints.

2.3.1.3 Pulp density

Density can be measured using X-ray fluorescence (XRF) devices or, alternatively, nuclear density meters. The installation of a density measurement device is critical to prevent the inaccuracies caused by bubbles. Density measurements are common in the feed to a flotation circuit, but not between flotation cells.

2.3.1.4 Concentrate flow rate

The direct measurement of concentrate flow rates in open channels are often not viable, and flow rates inferred from ultrasonic level transmitters in open channels with known dimensions are not accurate. Where the concentrate is pumped from a concentrate hopper, magnetic flow meters can be used to

measure the flow rate but any water addition to flotation cells or the concentrate hopper needs to be accounted for.

2.3.1.5 Concentrate density

The accuracy of concentrate density measurements is often problematic due to the presence of bubbles. Density measurements on the outflow from concentrate hoppers have been successfully used in mass pull-based control strategies, as reported by Singh, Louw and Hulbert (2003) and Gomes-Sebastiaõ, Hearne, Lam, Van der Spuy, Thompson and Vines (2018).

2.3.1.6 Air flow rate

A number of air flow measurement techniques are available that are generally considered accurate. A limitation is that the combined air flow rate to a bank of cells is often measured but not the flow to each cell, as described by Hadler *et al.* (2010a).

2.3.1.7 pH

pH measurements are often problematic due to contamination of the electrode. In some cases, conductivity probes can be used as a substitute.

2.3.1.8 Chemical or mineralogical analysis

Wills and Napier-Munn (2006) stated that the key to effective flotation control is real-time chemical analysis. Real-time XRF analysers can provide assays on several elements and the solids content, but the sampling delay varies between 15 seconds and one minute and, depending on the number of samples analysed, the cycle time can vary between five and 15 minutes (Laurila *et al.*, 2002). Visual and near-infra-red reflectance spectroscopic analysis can complement XRF devices and provide grade analyses at a much higher frequency (Shean and Cilliers, 2011).

2.3.1.9 Particle size analysis

The particle size distribution in pulp streams is commonly measured on industrial plants using laser scattering and diffraction, ultrasonics or distance measurement techniques (Coghill, Millen and Sowerby, 2002). An industrial particle size analyser is described by Kongas (2003), and a prototype using ultrasonic spectrometry combined with a gamma-ray gauge is described by Coghill *et al.* (2002). Laser scattering and diffraction techniques can be sensitive to air bubbles, particle shapes and particle reflectivity.

2.3.1.10 Froth image analysis

Flotation cameras differ in complexity and in the number of features that are extracted from the froth images. Aldrich *et al.* (2010) list features such as bubble size, shape, colour, velocity, burst rate, and mineral loading, while the froth height above the lip can also be included, as described by Phillpotts *et al.* (2021). Air recovery, α, has been defined by Hadler, Smith and Cilliers (2010b) as a function of froth velocity, v_f, froth height above the lip, h, the width of the lip where the froth overflows, w, and the inlet air flow rate, Q_a, as

$$\alpha = \frac{v_f \cdot h \cdot w}{Q_a}. \tag{2.1}$$

The measurements required to calculate α can be obtained reliably on industrial flotation circuits.

It is important to note that flotation circuits are often sparsely instrumented. The fact that measurement devices are available does not imply that every process stream would be instrumented. Flow rates and on-stream analyses are often only available on critical streams such as the final concentrate and final tailings streams, and pH measurements are often only available in the conditioning tank (Laurila *et al.*, 2002). The aim of Section 2.3 is to provide an indication of the types of instrumentation that are available and can be installed, should it be justified.

2.3.2 Other instrumentation

2.3.2.1 Bubble size in pulp

The McGill bubble sizer (Hernandez-Aguilar, Gomez and Finch, 2002) and the Anglo bubble sizer (Naik and Drunick, 2007) are used to characterise the operation of froth flotation cells and to detect faults on cells that are not performing as expected (Malinga, Turrer, Nascimento, Russo, Gonzaga, Silva, Machado and Sweet, 2018). Both devices use a submerged tube in the pulp, which is connected to a sloped viewing chamber, to view bubbles inside the pulp phase. The bubbles are photographed, and the images are processed to calculate the bubble size distribution. There is also room to use other measurements in soft-sensor applications. Vinnett, Yianatos and Alvarez (2014) showed a linear relationship between J_g and bubble size over typical operating ranges for J_g, which allows for simple models to be derived to estimate the bubble size in the pulp.

2.3.2.2 Superficial gas velocity

Superficial gas velocity, J_{g_k} into cell k can be calculated from the volumetric air flow rate into cell k, Q_{air_k} and the surface area of the flotation cell k, A_k as

$$J_{g_k} = \frac{Q_{air_k}}{A_k}. \tag{2.2}$$

Where Q_{air_k} is not measured, manual sampling devices have been used to calculate J_{g_k} based on the displacement of water by air in a tube suspended in the pulp (Savassi, Alexander and Johnson, 1997).

2.3.2.3 Gas hold-up

Gas hold-up is commonly measured using a differential pressure sensor (Finch and Dobby, 1990; Yianatos, Moys, Contreras and Villanueva, 2008) or using differential conductivity between an aerated and de-aerated chamber, as shown by Nesset, Hernandez-Aguilar, Acuna, Gomez and Finch (2006). In addition, Vinnett, Ledezma, Alvarez-Silva and Waters (2016) listed radioactive tracers and electrical resistance tomography as alternative approaches to estimate gas hold-up—each technique with its limitations. Vinnett *et al.* (2016) developed a soft sensor for gas hold-up based on J_g and the measured pulp bubble size distribution. The linear relationship between J_g and gas hold-up (Finch and Dobby, 1990) can also be used to develop soft sensors for gas hold-up.

2.3.2.4 Bubble loading

Devices to directly measure bubble loading and techniques to estimate bubble loading are discussed by Moys, Yianatos and Larenas (2010). All the devices that are discussed rely on manual intervention to obtain a measurement. The measurement devices capture bubbles that are loaded with hydrophobic particles. After a period of time, the solid particles that were previously attached to the bubbles, and the bubble volume are measured to calculate the bubble loading.

2.3.2.5 Froth Recovery

Rahman, Ata and Jameson (2013) described a device to measure froth recovery by collecting both particles that are dropped from the froth layer and particles that remain attached to the bubbles in the froth layer. Froth recovery is calculated periodically by manually measuring the weights of the collected samples.

2.3.2.6 Froth bubble size

In addition to the use of froth cameras to measure the top-of-froth bubble size, an instrument to measure the bubble size distribution inside the froth layer is described by Bhondayi and Moys (2014). An

additional outcome of the experiments conducted by Bhondayi and Moys (2014) is that the linear relationship between froth depth and bubble size has been confirmed.

2.3.2.7 Turbulence

Meng, Tabosa, Xie, Runge, Bradshaw and Manlapig (2016) listed various techniques that have been trialled to measure turbulence in flotation cells. None of the techniques that are listed is suitable to be used in a three phase systems. Impeller speed, impeller design, tank size, baffling, impeller size and aeration rate have been shown to affect turbulence.

2.4 MODELS AND MODEL-BASED CONTROLLERS

The flotation process involves a combination of physical and chemical reactions, with various interactions and disturbances. Generally, flotation modelling approaches can be divided into two categories: kinetic (first-principle) modelling and data-driven modelling. Kinetic modelling studies mainly include:

- flotation rate modelling—the influence of operational parameters, such as pulp density, chemical reagents, aeration rate and froth depth on the flotation rate
- mass balance modelling—mass and volume conservation in a flotation cell
- probability modelling—the probability of collision/adhesion/detachment between particles and bubbles, and the merging/bursting of bubbles.

Data-driven modelling mainly involves:

- performance evaluation—the relationship between flotation performance and froth features
- grade/recovery prediction—predicting the concentrate grade/recovery using feed characteristics and operational variables
- soft sensing—estimating key process variables (e.g. pH or pulp level) when the default instrument is not available or out of order.

A number of relevant model developments, their use in controllers and some key findings are described in the next section.

2.4.1 Fundamental models for pulp level control

Fundamental models are commonly used in froth flotation control to stabilise pulp levels down a bank of interacting cells in the presence of variations in feed rate. Despite their simplicity, flotation level control systems, such as Mintek's FloatStar (Schubert *et al.*, 1995), can significantly improve the economic performance of a flotation plant (Craig and Henning, 2000; Craig and Koch, 2003). Jämsä-Jounela (1992) described a simplified flotation model based on mass and volume balances to control a rougher flotation bank. The model parameters were obtained through an experimental industrial campaign. The level (L_k) response of a flotation cell (k) can be calculated from the difference between the pulp inflow from an upstream ($Q_{T_{k-1}}$) cell and the pulp outflow from the cell (Q_{T_k}) as

$$\frac{dL_k}{dt} = \frac{Q_{T_{i-1}} - Q_{T_i}}{A_k}, \tag{2.3}$$

assuming a constant cross-section area (A_k) over the range that the flotation cell level (L_k) is expected to vary.

Jämsä-Jounela *et al.* (2003) improved the model shown in (2.3) by taking the structure of flotation cells and valve sizing into account. Various control strategies for pulp level control, including proportional integral (PI) control, feed-forward control, decoupling control and multivariable control, have been tested and compared using this model (Kämpjärvi and Jämsä-Jounela, 2003).

2.4.2 Models considering the pulp and froth phases

Grade or mass pull-based control strategies, as described by Singh *et al.* (2003), require that the froth phase be considered in addition to pulp levels. To model the froth phase as part of a froth flotation model, a mass balance forms the core of the model to track mass flows between the feed, tailings and concentrate streams. Depending on the complexity of the model and the data that is available to fit model parameters, the mass balance may be performed on specific species in a stream—for example platinum group minerals (PGMs), chromite and gangue (Du Preez, Crundwell and Knights, 2013)—or further divided into floatability classes per species based on granulometry (typically, size classes) (Putz and Cipriano, 2015). Oosthuizen and Craig (2018) investigated how different floatability profiles affect the accuracy with which grades and recoveries can be estimated in a bank of flotation cells.

Bascur (2005) developed a detailed phenomenological flotation model. The model links the particle/bubble and water transport mechanisms and the hydrodynamic characteristic of a flotation cell, and describes the behaviour of particles with different mineralogical composition and particle sizes

under a wide range of steady-state and dynamic operating conditions. This model provides a detailed understanding of flotation operations at the expense of increasing complexity.

Deglon, Sawyerr and O'Connor (1999) used a flotation model with attachment and detachment rate constants in combination with a bubble population balance model to explain inconsistencies in flotation behaviour. While the focus was the effect of energy input (agitation) on flotation kinetics—mainly for scale-up—an optimum in the resultant flotation rate constant was illustrated as a function of specific energy and bubble surface area flux (S_b). In related research Safari and Deglon (2018) describes how flotation kinetics is affected by the counteracting effects of increased particle-bubble collisions versus decreased stability, as specific energy input (and potentially S_b) increases.

Bergh and Yianatos (2013) developed a simulator for rougher flotation banks and calibrated it using experimental data. The simulator was initially used in parallel to the existing control system to evaluate the effect of changes in operating conditions. It was later redesigned to act as an expert system, but this functionality has only been tested in a simulated environment. Other industrial implementations of expert systems (Kewe, Moffat and Schaffer, 2014) and optimisation strategies (Baas, Hille and Karageorgos, 2007) are often rule-based, with limited detail provided on the underlying models. Bergh and Yianatos (2013) modelled the mass transfer between the pulp and froth phase by defining a global cell recovery (R_G) based on collection zone recovery (R_C) and froth recovery (R_f), as defined in

$$R_G = \frac{R_C \cdot R_f}{1 - R_C(1 - R_f)}. \tag{2.4}$$

Yianatos *et al.* (2008) used a similar approach. Although (2.4) can be simplified by lumping the froth (R_f) and collection zone (R_C) recoveries together, Du Preez *et al.* (2013) noted that a more detailed model is likely to improve their results, which were based on a single-parameter model. The complexity of the equations describing the collection zone and froth recoveries shows some variation between the models by Bergh and Yianatos (2013) and Yianatos *et al.* (2008). Bergh and Yianatos (2013) modelled R_C as a function of the pulp residence time, flotation rate constants and the maximum achievable recovery. R_f was modelled using two equations. The first is a function of bubble load, superficial gas rate, concentrate mass flow, cell dimensions, and concentrate and bubble load grades. The other is a function of a froth stability parameter, froth depth, gas hold-up, superficial gas velocity and maximum froth recovery. Empirical models were fitted for both R_C and R_f to model the reduction in the flotation rate distribution and the reduction of froth stability when moving down a bank of flotation cells. Gangue recovery was modelled by Bergh and Yianatos (2013) and Yianatos *et al.* (2008)

based on water recovery, which is a function of superficial gas rate, froth depth and froth stability. The model fit used by Yianatos *et al.* (2008) required an extensive sampling campaign, including grade and mass data per size class on all streams, density (per stream), and air hold-up, bubble loading and grade, and aeration rates for each cell.

The compartment model described by Savassi (2005) included similar elements as (2.4) but with the contributions from true flotation and entrainment to overall recovery explicitly included in a single equation. Savassi (2005) defined R_G as

$$R_G = \frac{k_{cz} \cdot \tau_{cz} \cdot R_f \cdot (1 - R_w) + ENT \cdot R_w}{(1 + k_{cz} \cdot \tau_{cz} \cdot R_F) \cdot (1 - R_w) + ENT \cdot R_w}, \tag{2.5}$$

where k_{cz} is the collection zone recovery (flotation rate for the collection zone) and τ_{cz} is the residence time in the collection zone. Similar to (2.4), R_f refers to froth recovery, and ENT and R_w refer to the degree of entrainment and water recovery to the concentrate stream, respectively. Alves Dos Santos, Savassi, Peres and Martins (2014) showed how phenomenological models could be used as part of (2.5) to model entrainment, water recovery and froth recovery.

2.4.3 Froth depth profiling

Maldonado *et al.* (2007) used phenomenological models in a dynamic programming application to optimise the froth level profile for a bank of flotation cells. Seguel *et al.* (2015) used the same model but with a different cost function (maximising overall Cu recovery compared to minimising the sum of the squared Cu grades in the tailings flows). In both cases, the model used a single flotation rate constant per species. The flotation rate constant was modelled as a function of froth depth, residence time and pulp grade and was fitted using industrial data. The concentrate flow rate was calculated as a function of froth depth, and the rest of the model was based on mass balances. Although the model was not used in a real-time control application, it could potentially be used as a simulator running parallel to the plant. The importance of how the objective function is defined was highlighted in the work by Maldonado *et al.* (2007) and Seguel *et al.* (2015), where subtle changes in the objective function had a major effect on the system performance.

2.4.4 Model based controller implementations

Maldonado, Desbiens and del Villar (2009) implemented an MPC strategy to control a flotation column pilot plant. A conductivity probe was installed inside the pilot plant column, and gas hold-up in the collection zone and the wash water bias rate was calculated from conductivity measurements. A

2x2 model was implemented using an MPC controller, with the outputs defined as the gas hold-up and bias rate and the inputs as the wash water feed rate and aeration rate. Empirical models (fitted from operational data) were defined in the MPC controller. Upper and lower limits for both the gas hold-up and bias rate were included in the controller, based on a desired operating range and expected constraints within which the process needs to operate.

Putz and Cipriano (2015) used a hybrid MPC (HMPC) strategy on a simulator to control the final tailings grade of a flotation circuit subject to level constraints. The hybrid functionality was used to include scenarios where the pulp overflows and when the froth flow rate is zero, in addition to normal operation. The core of the model was a mass balance performed on a number of defined granulometries (size classes) for each species considered. The pulp levels in cells were calculated using a similar approach as described in (2.3), including valve dynamics and the effect of the relative heights of interacting cells. Collection rates (per granulometry class) define the mass transfer between the pulp and froth phases, while a drainage rate determines the mass transfer between the froth and pulp phases. Although the model included parameters such as air hold-up (in the level calculation) and reagent addition, no attempt was made to manipulate aeration rate or reagent addition for control purposes.

An example of an industrial MPC controller implementation on a copper rougher circuit was described by Brooks and Munalula (2017). Froth velocities (calculated from camera images) were controlled as part of the control strategy by manipulating air addition, cell pulp level setpoints and the frother dosage rate. The controller had limits configured on the concentrate and tailings grades. The MPC controller's objective function was configured to maximise recovery by maximising froth velocities. Empirical linear models were configured for the controller based on step-test data.

2.4.5 Peak air recovery

It has been shown that both grade and recovery are maximised when flotation cells are operated at their peak air recoveries (Smith *et al.*, 2010). A fundamental model has been developed to calculate air recovery based on froth film characteristics (Neethling and Cilliers, 2008). However, a controller that was implemented to operate a pilot scale flotation cell at its peak air recovery point used a peak-seeking strategy without including any models (Shean *et al.*, 2017).

2.4.6 Observations from modelling and controller implementations

Remes, Kongas, Saloheimo and Jämsä-Jounela (2005) came to an important conclusion regarding the role of stabilisation in the presence of measurement accuracies and sampling delays. Remes *et al.* (2005) developed a dynamic flotation model to study the influence of measurement accuracy and sampling frequency of real-time XRF analysers on the economical performance of the flotation process. It was shown that, to reduce the error caused by the measurement delay, fast basic measurement and control are necessary to complement process analysers and keep the process stable until the next assay arrives.

The benefit of a fundamental model over empirical models was demonstrated in a study by Zheng, Franzidis and Johnson (2006), who compared various empirical water recovery models to the fundamental water recovery model by Neethling, Lee and Cilliers (2003). Although the empirical models managed to model specific circuits reliably, only the fundamental model was able to model various circuits over a wide range of operating conditions. For this reason, fundamental models are preferred over empirical models, subject to constraints on model complexity and the ability to measure a sufficient number of the variables used in fundamental models.

2.4.7 Control strategies based on image analyses

Due to the close relationship between visual froth surface features and flotation performance, research has been done on the use of flotation cameras as soft sensors for grades to provide measurements at a faster rate than what can be provided by XRF analysers. Significant progress has been made in understanding froth behaviour and quantifying the impact of manipulated and disturbance variables on froth characteristics, such as the effect of reagent dosage on bubble size (Zhu, Gui, Yang, Xu and Wang, 2014). He, Yang, Wang, Gui and Wei (2013) utilised a probability density function (PDF) of the froth colour texture unit number to characterise froths based on colour and texture. A nonparametric estimation method based on the fixed normal kernel basis was proposed to describe this distribution. Xu, Chen, Xie, Yang and Gui (2015) proposed a comprehensive network-based texture extraction and classification method for froth imaging to extract the distinctive froth texture features in different production states. Liu and MacGregor (2008) developed a control strategy to achieve desired froth image properties that are related to froth stability by manipulating reagent addition rates. Zhu, Gui, Liu, Xu and Yang (2016) described the use of a B-spline estimator to determine the bubble size distribution, which is, in turn, used to classify bubble size distributions with non-Gaussian features. A multi-output

least square support vector machine (MLS-SVM) was then applied to establish a dynamic relationship between the weights of the B-spline estimator and the reagent dosage rate. Based on this structure, a reagent addition control strategy was implemented to track a desired bubble size distribution.

Other soft-sensing applications using froth images have also been evaluated. Xu, Chen, Chen, Xie, Yang and Gui (2016) proposed a multi-model soft measurement method to estimate the froth layer thickness based on visual features. The froth layer thickness was established by kernel extreme learning machine (KELM) models under different working conditions.

Aldrich *et al.* (2010) concluded that despite several advances in machine vision on flotation froths, conflicting results were obtained on linking image features to froth grade and no long-term fully automated control system based on machine vision has been developed to date. However, there may be scope to use froth image properties in combination with a flotation model and other measurements to calculate grade and other flotation characteristics. Ai, Xie, Tang, Zhang and Gui (2021) and Wang, Zhou, Song, Liu and Wang (2022) showed encouraging results in calculating setpoints for pulp levels and reagent addition rates respectively, by developing process control applications that integrate machine vision, machine learning, and physical measurements on the feed to a flotation circuit.

2.5 CONCLUDING REMARKS

The motivation to develop many of the existing flotation models is to model different circuit configurations or operating practices accurately, either for circuit design purposes or to recommend changes that would improve operation. Examples of such activities are described by Schwarz *et al.* (2006). Under these circumstances, a detailed sampling campaign can often be justified to provide the data to fit a comprehensive set of model parameters. Where models are to be used in continuous automatic control and optimisation applications, extensive manual sampling campaigns are not viable on an ongoing basis, and real-time measurements need to be used to maintain model integrity. A model for continuous control and optimisation applications would thus need to be structured in such a way that available real-time measurements provide the stimuli to the process model and also maintain model integrity by estimating the model parameters where possible.

Basic froth flotation models are typically extended to characterise some behaviour that cannot be explained by existing models. While more detailed models are essential to improve model accuracy

and advance knowledge about the process, more comprehensive flotation models have a larger set of parameters that needs to be fitted initially and updated regularly to maintain model consistency. Steady-state models are required for circuit design and improvement activities, as described by Schwarz *et al.* (2006), while models for dynamic process control applications require a focus on the dynamic responses of models and the changes in process variables over time. For dynamic control purposes, some accuracy could potentially be sacrificed in exchange for fewer parameters, as feedback provides a mechanism to correct discrepancies between the model outputs and the measurements. However, it is critical to include non-linear behaviour in the model, particularly where non-linearity changes the sign of the model response—for example, as is the case with the effect of J_g on grade below or above the peak in air recovery, as described by Hadler and Cilliers (2009) and Hadler *et al.* (2010b). While the decision on which interactions to ignore are not trivial, the limited set of measurements available on industrial flotation circuits dictates that simpler models with a significantly reduced parameter set are required, to ensure that model parameters and states can be updated dynamically from real-time measurements that are commonly available on industrial flotation circuits.

Although laboratory and pilot plant scale applications can provide information that can be used to derive empirical models for use in industrial applications, the long-term reliability of these models in the presence of changing operating conditions is a concern (Bouchard *et al.*, 2009). Phenomenological models should thus take priority if they are viable, but as all models and sensors would require periodic calibration, empirical models still have an important role to play in modelling and control applications.

While this chapter has covered a small portion of the flotation models and controller implementations on froth flotation circuits described in the literature, it provides an overview of the modelling techniques commonly employed and highlights the scarcity of model-based controllers used on industrial flotation circuits. The MPC strategy described by Maldonado *et al.* (2009) was only implemented on a pilot plant, and the HMPC strategy described by Putz and Cipriano (2015) was implemented on a simulator. A review of flotation models for froth flotation control by Quintanilla, Neethling and Brito-Parada (2021) came to similar conclusions: that very few examples of industrial implementations of MPC control are available, existing models focus on phenomena that are mostly applicable to the pulp phase, and the models used in controllers are mostly empirical models that are valid over a limited operating range.

The froth flotation model that is developed in the next chapter addresses these issues by providing a flotation model for dynamic process control and optimisation applications with sufficient complexity to describe the main flotation mechanisms, without losing the ability to continuously estimate key flotation parameters, by using real-time process measurements that are commonly available on industrial flotation circuits.

CHAPTER 3 MODEL DEVELOPMENT

3.1 CHAPTER OVERVIEW

This chapter is based on Oosthuizen *et al.* (2021) and describes the development of a dynamic froth flotation model that can be used in advanced model-based control and optimisation applications. A key aspect of the model is that the main model parameters can be estimated from real-time measurements that are commonly available on industrial flotation circuits, as confirmed by the state observability and controllability analysis shown in Chapter 4. Existing models available in the literature are combined into a model structure that allows model parameters to be estimated from real-time process measurements, and where suitable models are not available, empirical relations are derived.

Dynamic froth flotation models that include interactions in the pulp and froth phases are not common in the literature (Quintanilla *et al.*, 2021), and where detailed froth flotation models are available (Bascur, 2005; Schwarz *et al.*, 2006), the number and nature of parameters used in these models often require sampling and modelling campaigns that are much more extensive (and potentially disruptive) than the routine sampling commonly conducted on flotation processes.

Sections 3.2.1 and 3.2.2 show fundamental mass and volume balance models as the core of the model to describe pulp flows between flotation cells and the flow of the concentrate streams from flotation cells into a concentrate hopper. The steady-state water recovery model of Neethling and Cilliers (2009) is shown in Section 3.2.3 as the first component of the concentrate volumetric flow rate from each cell. Section 3.2.4 describes the concentrate mass flow model as a combination of a dynamic kinetic model for true flotation (Polat and Chander, 2000) and a steady-state model for entrainment (Neethling and Cilliers, 2009). A simplification of the entrainment model is also shown. The total concentrate volumetric flow rate model is described in Section 3.2.5 as a combination of the water recovery model described in Section 3.2.3 and the concentrate mass flow models described

in Section 3.2.4. Section 3.2.6 describes top-of-froth bubble size and air recovery models and the derivation of linear relationships based on data that were collected on an industrial flotation circuit (Hadler *et al.*, 2010a). Section 3.3 compares the modelled inputs, disturbances, states and outputs to the key variables identified in Chapter 2 to confirm that the key variables are included in the model that is derived in this chapter, and that model outputs correspond with measurements that are commonly available on industrial flotation circuits. The parameters fitted to the empirical models (Section 3.2.6) are described in Section 3.5. A steady-state simulation of the model using operating ranges from an industrial plant as described by Hadler *et al.* (2010a) is shown in Section 3.6.

3.2 MODEL DESCRIPTION

3.2.1 Volume balance

Mass and volume balances can be used to describe the transfer of pulp between flotation cells, the transfer of concentrate from flotation cells to a concentrate hopper, and also the transfer of materials between the pulp and froth phases within a flotation cell. Figure 3.1 shows the volumetric flow rates between four flotation cells and a concentrate hopper similar to the rougher section described by Hadler *et al.* (2010a).

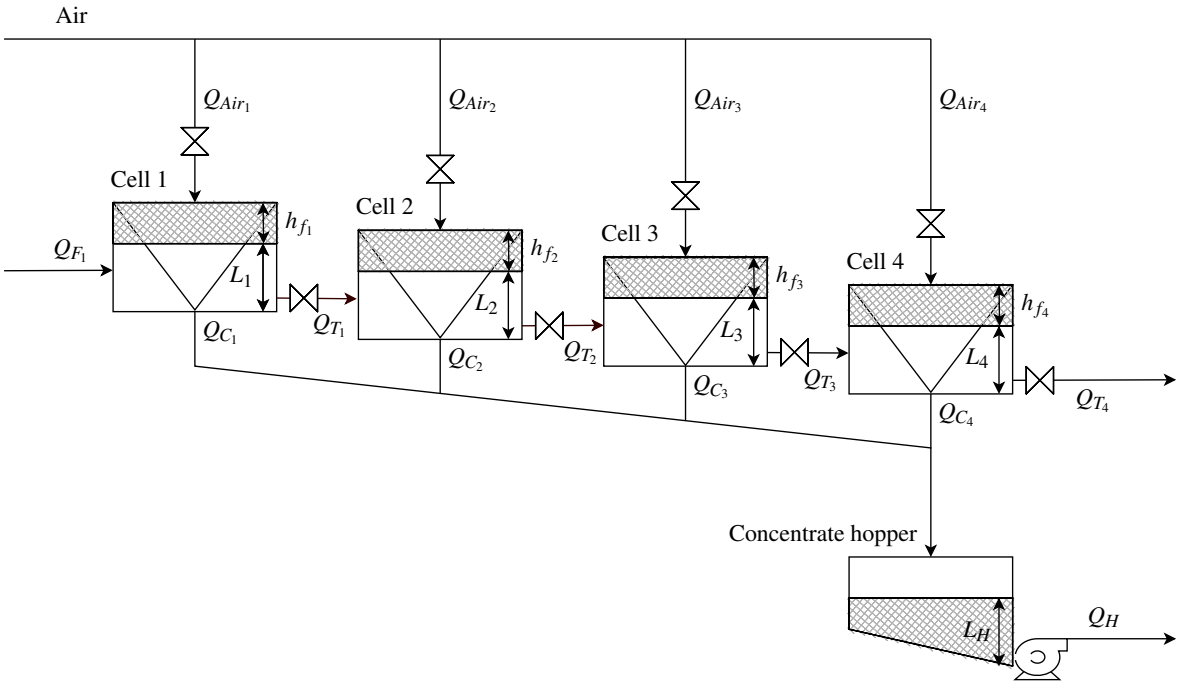

Figure 3.1. Volumetric flow rates between four flotation cells and a concentrate hopper.

The volumetric feed flow rate (Q_{F_1}) and density (ρ_{F_1}) are typically measured, and feed composition can be measured using an XRF device. For each cell k, a volume balance is defined as

$$\frac{dV_k}{dt} = A_k \frac{dL_k}{dt} = Q_{F_k} - Q_{T_k} - Q_{C_k}\,, \tag{3.1}$$

where Q_{F_k} is the volumetric feed flow rate to cell k, Q_{T_k} is the volumetric tailings flow rate from cell k, Q_{C_k} is the volumetric concentrate flow rate from cell k, A_k is the surface area of cell k and L_k is the pulp level in cell k. It is assumed that the flotation cell surface area, A_k, is uniform over its typical operating range.

The tailings flow rate from cell k is the feed flow rate to cell $k+1$ ($Q_{T_k} = Q_{F_{k+1}}$). Jämsä-Jounela *et al.* (2003) modelled the tailings flow rate, Q_{T_k}, from flotation cell, k, as

$$Q_{T_k} = C_{v_k} z_k \sqrt{L_k - L_{k+1} + h_k}\,, \tag{3.2}$$

where C_{v_k} is a constant that characterises the flow through the tailings valve with valve opening z_k, and h_k is the physical difference in height between cells k and $k+1$. It is assumed that a stabilisation controller as described by Schubert *et al.* (1995) is available to stabilise flotation pulp levels, L_k, by manipulating valve positions, z_k, to achieve the tailings flows rates, Q_{T_k}, from each flotation cell, k.

For the concentrate hopper with level L_H, and surface area A_H, the volume balance includes the concentrate inflows from all N contributing cells ($Q_{C_1} + Q_{C_2} + \ldots + Q_{C_N}$) and the outflow from the hopper (Q_H) as

$$\frac{dV_H}{dt} = A_H \frac{dL_H}{dt} = Q_{C_1} + Q_{C_2} + \ldots + Q_{C_N} - Q_H\,. \tag{3.3}$$

3.2.2 Mass balance

The rate of change in mass in each flotation cell, $\frac{d}{dt}M_k^{i,j}$ is calculated from the mass balance:

$$\frac{d}{dt}M_k^{i,j} = \dot{M}_{F_k}^{i,j} - \dot{M}_{T_k}^{i,j} - \dot{M}_{C_k}^{i,j}\,, \tag{3.4}$$

where $\dot{M}_{F_k}^{i,j}$ and $\dot{M}_{T_k}^{i,j}$ are the mass flow rates into and out of flotation cell k, respectively, and $\dot{M}_{C_k}^{i,j}$ is the mass flow rate out of flotation cell k via the concentrate stream. The feed mass flow rate, $\dot{M}_{F_k}^{i,j}$, into cell k is calculated from the feed volume, feed density and feed composition as

$$\dot{M}_{F_k}^{i,j} = Q_{F_k} \frac{SG_l\, SG_s\, C_{w_k}}{100\, SG_s - (SG_s - SG_l)\, C_{w_k}}\, G_{F_k}^{i,j}\,, \tag{3.5}$$

where Q_{F_k} is the volumetric feed flow rate into flotation cell k, C_{w_k} is the percentage solids by weight of the pulp flowing into cell k, SG_s and SG_l are the specific gravities of the ore and liquid, respectively, and $G_{F_k}^{i,j}$ is the feed grade of mineral species i and mineral class j to cell k. Equation (3.5) will be used to calculate the mass flow rates to the first flotation cell in the rougher circuit. The mass flow rates of different mineral species, i, are modelled separately to distinguish between desired (usually floatable) minerals containing the elements that the flotation circuit aims to recover and other gangue or undesired minerals. In addition, each species can be divided into multiple classes, j, where each class could have different floatability characteristics (Oosthuizen and Craig, 2018) and/or different size distributions affecting entrainment. The symbols are described in Table 3.1.

Table 3.1. Mass balance symbols.

Variable	Unit	Description
i	-	Superscript for mineral species (e.g. gangue or valuable mineral)
j	-	Superscript for mineral class with different floatability or size
k, H	-	Subscript for unit (flotation cell k, or hopper, H)
Δ	-	Subscript for concentrate C, tailings T, and feed F
$M_k^{i,j}$	kg	Accumulated mass of species i and class j, in cell k
$\dot{M}_{\Delta_k}^{i,j}$	kg/h	Mass flow rate associated with a specific cell, k
Q_{Δ_k}	m^3/h	Volumetric flow rate associated with a specific cell, k
C_{w_k}	%	Percentage solids by weight in the slurry feed to cell k
SG_s	-	Specific gravity of the bulk solids
SG_l	-	Specific gravity of the liquids

For the flotation cells, the tailings mass flow rate from cell k equals the feed flow rate to cell $k+1$ ($\dot{M}_{F_{k+1}}^{i,j} = \dot{M}_{T_k}^{i,j}$). The tailings mass flow rates from each cell can be calculated as the tailings volumetric flow rate $\dot{M}_{T_k}^{i,j}$ multiplied by the concentration of each species $M_k^{i,j}$ inside the flotation cell, as

$$\dot{M}_{T_k}^{i,j} = \frac{M_k^{i,j}}{L_k A_k} Q_{T_k}, \tag{3.6}$$

where the pulp volume of cell k is given by the pulp level, L_k, multiplied by the surface area, A_k, of cell k.

For the concentrate hopper, a similar approach can be followed, with the change in the mass of mineral species, i, and mineral class, j, in the concentrate hopper given by

$$\frac{d}{dt}M_H^{i,j} = \sum_{k=1}^{N} \dot{M}_{C_k}^{i,j} - \frac{M_H^{i,j}}{L_H A_H} Q_H \,. \tag{3.7}$$

The first term in (3.7) is the total inflow of mineral species i and mineral class j into the concentrate hopper, as the sum of the concentrate mass flow rates $\dot{M}_{C_k}^{i,j}$ from N contributing cells. The second term in (3.7) is the mass outflow rate of each mineral species, i, and mineral class, j, from the concentrate hopper, as a function of the mineral species in the hopper, $M_H^{i,j}$, the volumetric flow rate out of the hopper, Q_H, and the concentrate volume in the hopper, as a function of the hopper surface area, A_H, and the hopper level, L_H.

The hopper mass pull rate is given by

$$\dot{M}_H^{Tot} = \sum_{i=0}^{m} \sum_{j=0}^{n} \frac{M_H^{i,j}}{L_H A_H} Q_H \,, \tag{3.8}$$

where m and n are the number of modelled mineral species and classes, respectively.

3.2.3 Water recovery to the froth phase

The first component of the concentrate volumetric flow rate from each cell, Q_{W_k}, can be calculated from the steady-state water recovery model given by Neethling and Cilliers (2009). For a two-phase system, Neethling and Cilliers (2003) showed that froth depth or froth residence time are not the main causes of reduced water recovery observed when the froth height increases (Wang, Peng and Runge, 2016; Zheng *et al.*, 2006) but rather the increase in bubble size associated with deeper froths. Neethling and Cilliers (2003) showed that water recovery has an inverse squared relation to bubble diameter, with the proportionality constant determined by the bubble shape. The model for water recovery is defined as

$$\frac{Q_{W_k}}{A_k} = \begin{cases} \dfrac{{J_{g_k}}^2 \lambda_{out}}{k_1} (1 - \alpha_k) \alpha_k & 0 < \alpha_k < 0.5 \\ \dfrac{{J_{g_k}}^2 \lambda_{out}}{4k_1} & \alpha_k \geq 0.5 \end{cases} , \tag{3.9}$$

where J_{g_k} is the superficial gas velocity for cell k, and α_k is the air recovery for cell k.

The Plateau border length (λ_{out}) per volume of froth as used in (3.9) is defined as

$$\lambda_{out} \approx \frac{6.81}{{D_{BF_k}}^2} \,, \tag{3.10}$$

where D_{BF_k} is the mean top of froth bubble diameter for cell k. It is assumed for (3.10) that the bubbles have similar geometry as Kelvin cells (Neethling and Cilliers, 2003). k_1 in (3.9) quantifies the opposing forces acting on a particle due to gravity and viscosity, and is defined as

$$k_1 = \frac{\rho g}{3\mu C_{PB}}, \tag{3.11}$$

where ρ is the fluid density, C_{PB} is the Plateau border drag coefficient and μ is the fluid viscosity. J_{g_k} is calculated from the aeration rate Q_{air_k} of the flotation cell and its surface area, A_k, as

$$J_{g_k} = 100\frac{Q_{air_k}}{A_k}. \tag{3.12}$$

Table 3.2 summarises the variables for the water recovery model and provides the units for each variable.

Table 3.2. Variables used in concentrate flow rate and entrainment models (Neethling and Cilliers, 2009).

Variable	Units	Description	Typical value
C_{PB}	–	Plateau border drag coefficient	50
D_{BF_k}	mm	Mean top of froth bubble diameter for cell k	10
J_{g_k}	mm/s	Superficial gas velocity for cell k	10
P_e	–	Dispersion Peclet number	0.15
Q_{air_k}	m^3/h	Volumetric air flow rate to cell k	360
d_{pmin}	μm	Particle minimum diameter	10
d_{pmax}	μm	Particle maximum diameter	150
g	m/s^2	Gravitational acceleration	9.81
h_{f_k}	mm	Froth depth	110
α_k	–	Air recovery for cell k	0.25
$\rho_s^{i,j}$	kg/m^3	Solid particle density for species i and class j	3000
ρ	kg/m^3	Fluid density	1000
μ	$Pa \cdot s$	Fluid viscosity	0.001

3.2.4 Concentrate mass flow rate

The two main flotation mechanisms governing the transfer of material between the pulp and overflowing froth phases are the true flotation of hydrophobic particles and entrainment of all particles

together with the bubble stream (Wills and Napier-Munn, 2006). True flotation is often modelled as a first-order process, while entrainment is a function of particle size, density and the upward stream of liquid (water recovery) as part of the bubble stream. The bulk of the desired mineral in the concentrate stream would typically be hydrophobic particles (due to true flotation) and the bulk of the gangue minerals in the concentrate stream would typically be entrained particles. However, both desired and gangue minerals are entrained into the froth layer, and depressants are often required as a reagent to suppress weakly floatable gangue minerals. In this work, both true flotation and entrainment are modelled for all mineral species to quantify the contribution of each mechanism to the final concentrate stream and provide insight into the effectiveness of the flotation reagents (depressants and activators). A model-based control system can optimise the true flotation and entrainment mass flows from each flotation cell by exploiting differences in the concentrations of mineral species among flotation cells and their impact on the combined grade and recovery of the concentrate stream.

3.2.4.1 True flotation model

True flotation is usually modelled using a kinetic model based on a chemical reactor analogy, as described by Polat and Chander (2000), for a batch reactor. Such a model has the general form:

$$\frac{dC_{p_k}^{i,j}}{dt} = -K^{i,j} C_{p_k}^{i,j} C_{b_k} R_{f_k}\,, \tag{3.13}$$

where $C_{p_k}^{i,j}$ represents the concentrations of particles of species i, class j in the pulp of cell k, and C_{b_k} represents the concentration of bubbles in the pulp. $K^{i,j}$ is a pseudo rate constant that depends on various parameters affecting the flotation process. $K^{i,j}$ is modelled as a distribution with different values for each species i and class j. R_{f_k} represents the froth recovery.

In this work, $K^{i,j}$ accounts for all mechanisms in the pulp related to the attachment and detachment of hydrophobic particles to air bubbles. The true flotation model of (3.13) is hence modified to include the detachment of particles in the froth phase due to bursting bubbles, by setting R_{f_k} equal to the air recovery (α_k), described in Section 3.2.3. As the attachment of particles only takes place on the surfaces of bubbles, the effect of bubble surface area flux is taken into account by replacing C_{b_k} in (3.13) with a bubble surface area flux term, as described by Runge and Franzidis (2003) as

$$S_{b_k} = 6\frac{J_{g_k}}{D_{BP_k}}\,. \tag{3.14}$$

Assuming that the operational range of the froth depth (h_{f_k}) has a negligible effect on the pulp volume, the change in mineral concentration in the cell due to true flotation ($C_{p_k}^{i,j}$) is replaced in (3.15) by a

change in the mass of each species and class ($M_k^{i,j}$) in flotation cell, k:

$$\frac{dM_k^{i,j}}{dt} = -K^{i,j} M_k^{i,j} S_{b_k} \alpha_k \,, \tag{3.15}$$

where D_{BP_k} is the Sauter mean bubble diameter in the pulp for cell, k. Table 3.3 summarises the variables for the true flotation model and provides the units for each variable.

Table 3.3. Variables used in the true flotation model.

Variable	Units	Description
$C_{p_k}^{i,j}$	kg/m^3	Concentrations of particles of species i, class j in the pulp of cell k
D_{BP_k}	mm	Sauter mean bubble diameter in pulp for cell k
$K^{i,j}$	–	Flotation rate constant for species i, class j
R_{f_k}	–	Froth recovery for cell k, assumed to be equal to α_k
S_{b_k}	s^{-1}	Bubble surface area flux for cell k

3.2.4.2 Entrainment model

The entrainment model is based on the steady-state model by Neethling and Cilliers (2009), but is simplified to lump the effect of different size classes together. The original entrainment model of Neethling and Cilliers (2009) calculates an entrainment factor, $Ent^{i,j}$, as

$$Ent^{i,j} \approx \begin{cases} exp\left(-\frac{{v_{set}^{i,j}}^{1.5} h_{f_k}}{D_{Axial}\sqrt{J_{g_k}\alpha_k(1-\alpha_k)}}\right) & 0 < \alpha_k < 0.5 \\ exp\left(-\frac{2{v_{set}^{i,j}}^{1.5} h_{f_k}}{D_{Axial}\sqrt{J_{g_k}}}\right) & \alpha_k \geq 0.5 \end{cases} . \tag{3.16}$$

$Ent^{i,j}$ in (3.16) defines the fraction of particles with a defined size, d_p, and density, $\rho_s^{i,j}$, that will be entrained for a specified J_{g_k} and froth depth, h_{f_k} (3.16). The particle settling velocity, $v_{set}^{i,j}$, in (3.16) is defined as

$$v_{set}^{i,j} \approx \frac{1}{3}\frac{g\,(\rho_s^{i,j} - \rho)\,d_p^2}{18\mu} \,, \tag{3.17}$$

for species i and class j. The axial dispersion coefficient, D_{Axial}, in (3.16) is given by

$$D_{Axial} \approx \frac{J_{g_k}^{1.5}}{\sqrt{k_1\left(\sqrt{3} - \pi/2\right)P_e}} \,, \tag{3.18}$$

where P_e is the dispersion Peclet number (Neethling and Cilliers, 2009). The variables and units for the entrainment model are defined in Table 3.2. Neethling and Cilliers (2009) noted that although $Ent^{i,j}$ does not include a term for the froth bubble size, the water recovery defined in (3.9) is dependent on D_{BF_k}, implying that the entrained mass is a function of froth depth and froth bubble size.

3.2.4.3 Simplified entrainment model

Equation (3.16) has a sharp transition between an entrainment factor of 0 and 1 over a narrow range in J_{g_k} for a particular particle size, d_p. Using a single entrainment factor with an average particle size does not provide an accurate model with a gradual increase in entrainment (of particles of different sizes) as J_{g_k} increases, and using multiple entrainment factors to model different particle sizes quickly increases model dimensions beyond practical limits. A simplified entrainment factor $Ent_{var}^{i,j}$ was consequently derived to describe the entrainment of particles as a function of J_{g_k} and h_{f_k}, based on the entrainment models described in (3.16 - 3.18). $Ent_{var}^{i,j}$ is defined as

$$Ent_{var}^{i,j} = exp(-\frac{K_{ent}^{i,j}\, h_{f_k}\, {d_{ptr}^{i,j}}^3}{{J_{g_k}}^2}), \tag{3.19}$$

where all other variables are lumped together in the single constant $K_{ent}^{i,j}$, defined as

$$K_{ent}^{i,j} = \left[\frac{1}{3}\frac{g\,(\rho_s^{i,j} - \rho)}{18\mu}\right]^{1.5} \frac{\sqrt{k_1\left(\sqrt{3} - \pi/2\right) P_e}}{\sqrt{\alpha_k(1-\alpha_k)}}. \tag{3.20}$$

The particle diameter, $d_{ptr}^{i,j}$, for which the entrainment factor equals 0.5, can be calculated from (3.19) and (3.20) as

$$d_{ptr}^{i,j} = \sqrt[3]{\frac{-\ln(0.5)\,{J_{g_k}}^2}{K_{ent}^{i,j}\, h_{f_k}}}. \tag{3.21}$$

For smaller particles, in particular, the entrainment factor changes from 0 to 1 over a fairly narrow range of superficial air velocities. Assuming that this transition occurs rapidly, and also assuming a flat size distribution profile over all size classes (on a log axis), the fraction of the material (of all size classes) that is entrained, $Ent_{Frac}^{i,j}$ can be estimated as the ratio of the size class for which 50% is entrained over the total size range, where d_{pmin} and d_{pmax} represent the minimum and maximum ranges of the size classes that are modelled, as described by

$$Ent_{Frac}^{i,j} = \frac{\ln(d_{ptr}^{i,j}) - \ln(d_{pmin})}{\ln(d_{pmax}) - \ln(d_{pmin})}. \tag{3.22}$$

A comparison of the original entrainment factor $Ent^{i,j}$ in (3.16) (Neethling and Cilliers, 2009) and the simplified entrainment factor $Ent_{Frac}^{i,j}$ in (3.22) is shown in Figure 3.2. This figure shows a good correlation over a wide range of J_{g_k}, between 0 and 1 cm/s. For the comparison shown in Figure 3.2, $d_{pmin} = 8\mu$m, $d_{pmax} = 220\ \mu$m and $\alpha_k = 0.5$ were used.

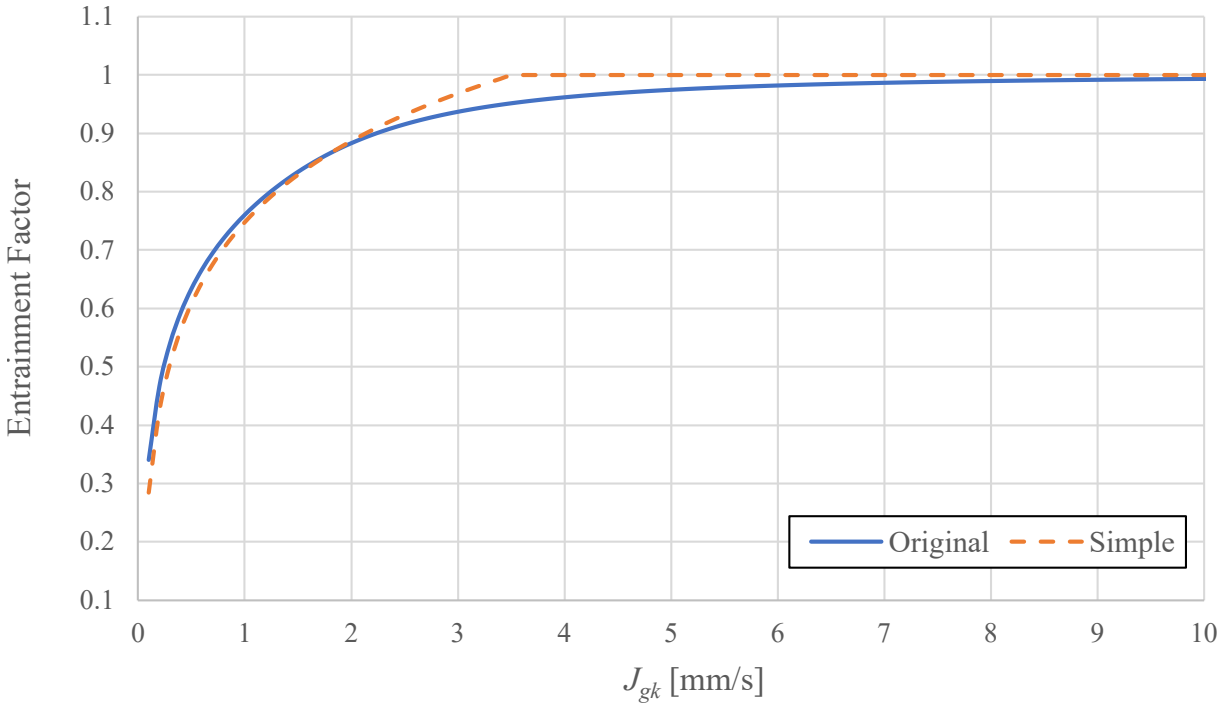

Figure 3.2. Comparison of original (3.16) and simplified (3.22) entrainment models.

3.2.4.4 Combined concentrate mass flow rate

The overall concentrate mass flow rate from each cell $\dot{M}_{C_k}^{i,j}$ includes true flotation and entrainment components. $Ent^{i,j}$ is defined as the ratio of the entrained solids concentration $C_{c_k}^{i,j}$ to the pulp solids concentration $C_{p_k}^{i,j}$, as shown in

$$Ent^{i,j} \approx \frac{C_{c_k}^{i,j}}{C_{p_k}^{i,j}}. \tag{3.23}$$

Equations (3.15), (3.23), (3.20) and (3.22) can be combined to yield

$$\dot{M}_{C_k}^{i,j} = K^{i,j} M_k^{i,j} S_{b_k} \alpha_k + Ent_{Frac}^{i,j} \frac{M_k^{i,j}}{A_k L_k} Q_{C_k}, \tag{3.24}$$

with $C_{p_k}^{i,j}$ in (3.23) defined as

$$C_{p_k}^{i,j} = \frac{M_k^{i,j}}{A_k L_k}. \tag{3.25}$$

3.2.4.5 Variables calculated from the concentrate mass flow rates

The concentrate grade from each cell k, G_{C_k}, can be calculated from (3.24) as the ratio of the desired element mass flow rate in the concentrate stream, $\dot{M}_{DC_k}$ (which may occur in a single or multiple

mineral species), relative to the total concentrate mass flow rate, as

$$G_{C_k} = \frac{\dot{M}_{DC_k}}{\sum_{i=1}^{m}\sum_{j=1}^{n}\dot{M}_{C_k}^{i,j}}. \tag{3.26}$$

An *instantaneous* recovery, R_{C_k}, can be calculated as the ratio of the desired element mass flow rate in the concentrate stream relative to the desired element mass flow rate in the feed stream $\dot{M}_{DF}$, as

$$R_{C_k} = \frac{\dot{M}_{DC_k}}{\dot{M}_{DF}}. \tag{3.27}$$

Despite the *instantaneous* recovery not taking variability in the feed composition and residence times in the flotation circuit into account, it provides a useful real-time approximation of recovery. The measured concentrate grade from the hopper, G_H, can be calculated from the ratio between the desired mass, M_{D_H}, and the total masses in the concentrate hopper as

$$G_H = \frac{M_{D_H}}{\sum_{i=1}^{m}\sum_{j=1}^{n}M_H^{i,j}}. \tag{3.28}$$

3.2.5 Combined concentrate volumetric flow rate

The first component of the concentrate volumetric flow rate from each cell was defined in Section 3.2.3 based on the steady-state water recovery model described by Neethling and Cilliers (2009). Equation (3.9) needs to be extended to also include the volumetric flow rate of minerals due to true flotation as described in Section 3.2.4.1. The volumetric concentrate flow rate for flotation cell k is given by

$$Q_{C_k} = \begin{cases} A_k \dfrac{{J_{g_k}}^2 \lambda_{out}}{k_1}(1-\alpha_k)\alpha_k + \frac{dM_k^{i,j}}{dt}/\rho_s^{i,j} & 0 < \alpha_k < 0.5 \\ A_k \dfrac{{J_{g_k}}^2 \lambda_{out}}{4k_1} + \frac{dM_k^{i,j}}{dt}/\rho_s^{i,j} & \alpha_k \geq 0.5 \end{cases}, \tag{3.29}$$

where $\frac{dM_k^{i,j}}{dt}$ is the mass flow rate of mineral species i, class j to the froth phase in cell k due to true flotation, and $\rho_s^{i,j}$ is the density of mineral species i, class j.

3.2.6 Froth stability and bubble size models

The entrainment, water recovery and true flotation models described in (3.9), (3.15), (3.22) and (3.23) use bubble size (D_{BF_k}) and air recovery (α_k) as parameters. These are dynamic parameters that vary with operating conditions and need to be modelled.

Several attempts have been made to model α_k or other measures of froth stability and the effect of the entrained and attached particles on froth stability—often with conflicting results (Ata, 2008; Tang and Tan, 1989). Zheng *et al.* (2006) and Barbian, Ventura-Medina and Cilliers (2003) reported a strong correlation between air recovery and the ratio between froth depth and $h_{froth-max}$, where $h_{froth-max}$ is an experimentally determined maximum depth that froth would grow to in a non-overflowing column. However, $h_{froth-max}$ is not constant but increases as a function of the aeration rate (Barbian *et al.*, 2003). Although different measures of froth stability are used in the literature, good correlations have been reported for some measures of bubble burst rates, dynamic froth stability and air recovery (Morar, Hatfield, Barbian, Bradshaw, Cilliers and Triffett, 2006).

The role of bubble size in froth stability was investigated by Geldenhuys and McFadzean (2019) and Gallegos-Acevedo, Espinoza-Cuadra, Perez-Garibay and Pecina-Trevino (2010). It was concluded that the top-of-froth bubble size in a non-overflowing column is determined by the bubble loading and is independent of the pulp bubble size. It was further shown that $h_{froth-max}$ follows a decaying trend with pulp bubble size. Ata (2008) performed experiments to determine the coalescence time of bubbles with varying surface coverings. It was shown that the relation between the coalescence time between two bubbles and the percentage of their surface coverage is mostly linear. Gallegos-Acevedo *et al.* (2010) obtained similar results but also showed how the average bubble size stabilised at a constant value of approximately 3 mm for high bubble loadings, while the average bubble size exceeded 5 mm at lower loadings, indicating that further coalescence was inhibited at high bubble loadings.

Neethling and Cilliers (2003) used common probability functions to determine the probability that a bubble film would fail, both in the models for bubble coalescence and in models for bubbles bursting at the top of the froth. Morar, Bradshaw and Harris (2012) used similar variables and fitted the bubble burst rate to a power function of both bubble size and bubble loading, but the sign of the power function was not consistent for all experiments. Despite agreement on the mechanisms affecting froth stability, Neethling and Brito-Parada (2018) concluded that the mechanisms for froth stability cannot be modelled with sufficient accuracy, and hence used an empirical relation to model froth stability and bubble size in combination with the fundamental water recovery model described in (3.9) - (3.11).

Empirical models of top-of-froth bubble size and air recovery were derived by Oosthuizen *et al.* (2021) based on industrial data collected by Hadler *et al.* (2010a). The steady-state top-of-froth bubble size

D_{BFSS_k} in cell k is given by

$$D_{BFSS_k} = K_{BF_{Jg}} J_{g_k} + K_{BF_\lambda} \lambda_{air_k} + D_{OS_k}, \tag{3.30}$$

where $K_{BF_{Jg}}$, K_{BF_λ} and D_{OS_k} are empirical constants, and λ_{air_k} is the average froth residence time, defined as

$$\lambda_{air_k} = \frac{h_{f_k}}{J_{g_k}}. \tag{3.31}$$

A variation on the α_k model fitted by Oosthuizen *et al.* (2021) was used to ensure that α_k has a peak in J_{g_k}, which depends on h_{f_k} (Hadler, Greyling, Plint and Cilliers, 2012). The steady-state model of air recovery, α_{SS_k} is given by

$$\alpha_{SS_k} = K_{\alpha_{J_g}} (J_{g_k} - K_{\alpha_{J_{g_k}}} - K_{\alpha_{h_f}} h_{f_k})^2 + \alpha_{OS_k}, \tag{3.32}$$

where $K_{\alpha_{J_g}}$, $K_{\alpha_{J_{g_k}}}$, $K_{\alpha_{h_f}}$ and α_{OS_k} are empirically fitted parameters. $K_{\alpha_{J_g}}$ is a negative constant to define a parabola with a peak air recovery at $J_{g_k} = K_{\alpha_{J_{g_k}}} + K_{\alpha_{h_f}} h_{f_k}$.

The top-of-froth bubble size D_{BF_k} for flotation cell k is defined as a function of D_{BFSS_k}, in (3.30) and λ_{air_k} in (3.31), as

$$\frac{d}{dt} D_{BF_k} = \frac{D_{BFSS_k} - D_{BF_k}}{\lambda_{air_k}}. \tag{3.33}$$

Similarly, the air recovery for cell k, α_k, is defined as a function of α_{SS_k}, in (3.32) and λ_{air_k} in (3.31), as

$$\frac{d}{dt} \alpha_k = \frac{\alpha_{SS_k} - \alpha_k}{\lambda_{air_k}}. \tag{3.34}$$

First order models with unity gains define the dynamic responses of superficial gas velocities (J_{g_k}) to setpoint changes (J_{gSP_k}) as

$$\frac{d}{dt} J_{gk} = \frac{J_{gSP_k} - J_{g_k}}{\tau_{J_{g_k}}}, \tag{3.35}$$

where $\tau_{J_{g_k}}$ is the first order time constant of the air valve response of cell k.

3.2.7 Model summary

The symbols used in the flotation model are shown in Table 3.4, and the estimated model parameters are shown in Table 3.5. The state equations for each flotation cell, k, are summarised in Table 3.6, and the state equations for the concentrate hopper are summarised in Table 3.7. The *Online measured* column in Tables 3.6 and 3.7 indicates if a state is measured. Additional measured model outputs (calculated from states) are shown in Table 3.8, and measured disturbances are shown in Table 3.9.

The model states in Tables 3.6 and 3.7 that are not measured need to be estimated together with the estimated parameters shown in Table 3.5.

Table 3.4. Flotation model symbols.

Variable	Unit	Description
i	-	Superscript for mineral species (e.g. gangue or valuable mineral)
j	-	Superscript for mineral class with different floatability or size
k, H	-	Subscript for unit (flotation cell k, or hopper H)
Δ	-	Subscript for concentrate C, tailings T, and feed F
A_k, A_H	m^2	Surface area of cell k or concentrate hopper H
J_{g_k}	mm/s	Superficial gas velocity for cell k
J_{gSP_k}	mm/s	Superficial gas velocity setpoint for cell k
$M_k^{i,j}$	kg	Accumulated mass of species i and class j in cell k
$\dot{M}_{\Delta_k}^{i,j}$	kg/h	Mass flow rate associated with a specific cell k
Q_{Δ_k}	m^3/h	Volumetric flow rate associated with a specific cell k
Q_{air_k}	m^3/h	Volumetric air flow rate to cell k
h_{f_k}	mm	Froth depth
λ_{air_k}	s	Average froth residence time ($\frac{h_{f_k}}{J_{g_k}}$)
τ_{Jg_k}	s	First order time constant of the air valve response of cell k

Table 3.5. Model parameters to be estimated.

Symbol	Unit	Description
$K_{BF_{J_g}}$	s	Effect of the superficial gas velocity on the mean top-of-froth bubble diameter
K_{BF_λ}	mm/s	Effect of the average froth residence time on the mean top-of-froth bubble diameter
$K_{\alpha_{J_{g_k}}}$	mm/s	Value of the superficial air velocity in cell k where air recovery is maximised when $h_{f_k} = 0$
$K_{\alpha_{J_g}}$	s^2/mm^2	Effect of the difference between J_{g_k} and J_{g0} squared on air recovery
$K_{\alpha_{h_f}}$	1/s	Effect of a change in h_{f_k} on the superficial air velocity where air recovery is maximised
α_{OS_k}	-	Offset included in steady-state air recovery equation, α_{SSk} in cell k
D_{OS_k}	mm	Offset included in the steady-state top-of-froth bubble diameter equation, D_{BFSS_k} in cell k
C_{v_k}	$m^{5/2}/h$	Valve constant for cell k
C_{PB}	-	Plateau border drag coefficient
$K^{i,j}$	-	Flotation rate-constant for species i, class j

Table 3.6. States for each flotation cell.

Symbol	Unit	Description	State equation	Online measured
D_{BF_k}	mm	Top of froth bubble diameter	$\frac{d}{dt}D_{BF_k} = \frac{D_{BFSS_k} - D_{BF_k}}{\lambda_{air_k}}$	Yes
α_k	-	Air recovery	$\frac{d}{dt}\alpha_k = \frac{\alpha_{SS_k} - \alpha_k}{\lambda_{air_k}}$	Yes*
L_k	m	Cell pulp level	$\frac{d}{dt}L_k = (Q_{F_k} - Q_{T_k} - Q_{C_k})/A_k$	Yes
$M_k^{i,j}$	kg	Masses in flotation cell	$\frac{d}{dt}M_k^{i,j} = \dot{M}_{F_k}^{i,j} - \dot{M}_{T_k}^{i,j} - \dot{M}_{C_k}^{i,j}$	No
J_{g_k}	mm/s	Superficial gas velocity	$\frac{d}{dt}J_{gk} = \frac{J_{gSP_k} - J_{g_k}}{\tau_{J_{g_k}}}$	No

* 'measured' as indicated in (2.1)

Table 3.7. States for the concentrate hopper.

Symbol	Unit	Description	State equation	Online measured
L_H	m	Hopper level	$A_H \frac{dL_H}{dt} = \sum_{k=1}^{N} Q_{C_k} - Q_H$	Yes
$M_H^{i,j}$	kg	Masses in hopper	$\frac{d}{dt} M_H^{i,j} = \sum_{k=1}^{N} \dot{M}_{C_k}^{i,j} - \frac{M_H^{i,j}}{L_H A_H} Q_H$	No

Table 3.8. Additional measured model outputs.

Symbol	Unit	Description	Output equation
G_H	-	Grade in hopper	$G_H = \frac{\sum_{j=1}^{n} M_H^{0,j}}{\sum_{i=1}^{m}\sum_{j=1}^{n} M_H^{i,j}}$
G_{T_4}	-	Grade in cell 4 tailings stream	$G_{T_4} = \frac{\sum_{j=1}^{n} M_4^{0,j}}{\sum_{i=1}^{m}\sum_{j=1}^{n} M_4^{i,j}}$
C_{w_H}	%	Percent solids by mass in the hopper	$C_{w_H} = 100 \frac{\sum_{i=1}^{m}\sum_{j=1}^{n} M_H^{i,j}}{\sum_{i=1}^{m}\sum_{j=1}^{n} M_H^{i,j} + \rho\left(A_H L_H - \sum_{i=1}^{m}\sum_{j=1}^{n} \frac{M_H^{i,j}}{\rho_s^{i,j}}\right)}$
C_{w_T}	%	Percent solids by mass in the tailings	$C_{w_T} = 100 \frac{\sum_{i=1}^{m}\sum_{j=1}^{n} M_4^{i,j}}{\sum_{i=1}^{m}\sum_{j=1}^{n} M_4^{i,j} + \rho\left(A_4 L_4 - \sum_{i=1}^{m}\sum_{j=1}^{n} \frac{M_4^{i,j}}{\rho_s^{i,j}}\right)}$

Table 3.9. Measured disturbances.

Symbol	Unit	Description
Q_{F_1}	m^3/h	Volumetric feed flow rate to cell 1
C_{w_1}	%	Feed density for flotation cell 1 (% solids by mass)
G_F^i	-	Feed grade of species i to cell 1
d_{pmin}	μm	Particle minimum diameter
d_{pmax}	μm	Particle maximum diameter

3.3 EVALUATION OF THE MODEL WITH REGARD TO THE KEY VARIABLES DEFINED IN CHAPTER 2

The model inputs, outputs, states, internal variables and disturbances that were identified in Chapter 2 are repeated in Tables 3.10 - 3.15, including a motivation where a variable was not included in the model, and a reference to the section where the model for each state and output is described. The *internal model variables* shown in Table 3.14 include variables that have been identified as key model states in Chapter 2 that can be derived from the model states defined in Table 3.13.

Table 3.10. Model inputs (manipulated variables).

Variable	Description
Modelled	
Pulp level setpoints	Pulp level setpoints are included in the model to manipulate the volume of pulp in each flotation cell and froth depth simultaneously. Refer to Section 3.2.1 and (3.1).
Air flow rate setpoints	Air flow rate setpoints are included in the model and impact a range of flotation mechanisms in the pulp and froth phases, including true flotation, entrainment, water recovery, air recovery and bubble size. Refer to Section 3.2.3, Section 3.2.4 and (3.12).
Not modelled	
Reagent addition	The model structure and parameter set allow for reagents to be included in future versions of the model. For this version, reagent addition will not be included, as the dataset used (Hadler *et al.*, 2010a) did not include variations in reagent addition rates. The effect of variations in reagent additions and other dynamics that are not modelled explicitly are lumped together in the model parameters.
Froth wash water	Froth wash water was not used on any cells of the rougher flotation circuit that was modelled, and it was hence excluded from the model.

Table 3.11. Measured disturbances (modelled).

Variable	Description
Modelled	
Feed density	The feed density is commonly measured on industrial flotation circuits using nuclear density meters or as an output from an XRF analyser and is included in the model as a measured disturbance (see C_{w_k} in (3.5)).
Volumetric feed flow rate	The volumetric feed flow rate is commonly measured on industrial flotation circuits using magnetic flow meters and is included in the model as a measured disturbance. The combination of feed density and volumetric feed flow rate is used to calculate the liquid feed flow rate to the flotation circuit (see Q_{F_k} in (3.5) for $k = 1$).
Feed grade	The feed grade is often measured on industrial flotation circuits using online XRF analysers or at a higher sampling frequency using visual and near-infrared reflectance spectroscopy. Feed grade is included in the model as a measured disturbance. The combination of feed density, volumetric feed flow rate and feed grade is used in the model to calculate the feed mass flow rate of different mineral species (see G_{F_k} in (3.5) for $k = 1$).
Feed size distribution	The model uses two data points on the feed size distribution as measured disturbances. Refer to Section 3.2.4.2 and (3.16).
Froth properties (speed, bubble size distribution and stability)	Froth properties are included as states in Table 3.13. Refer to Section 3.2.6, (2.1), (3.33) and (3.34).

Table 3.12. Measured disturbances (not modelled).

Variable	Description
Not modelled	
Electrochemical potentials (Eh and pH)	It is assumed that a stabilisation control strategy is in place to control the pH to a desired value that will favour selective flotation of minerals where it is applicable. The effect of pH and Eh on model states and outputs is not explicitly included in the model, but the effect of variations in pH would be observable through variations in the floatability of different mineral species.
Feed mineralogy (fineness of crystallisation and minerals)	No real-time measurement of crystallisation or liberation is available. Any variation will be treated as unmeasured disturbances that affect model parameters.

Table 3.13. Model states.

Variable	Description
Modelled	
Pulp levels in flotation cells and the concentrate hopper	Pulp levels are defined as model states based on the volume balance described in Section 3.2.1.
Mineral masses	The mineral masses in each flotation cell and in the concentrate hopper are modelled using the mass balance described in Section 3.2.2. The mass flows between the pulp and froth phases within each flotation cell are modelled by taking the mechanisms of true flotation (see Section 3.2.4.1) and entrainment (see Section 3.2.4.2) into account.
Froth properties (speed, bubble size distribution and stability)	The top-of-froth bubble size D_{BF_k} and air recovery α_k (as a measure of froth stability) are defined as model states in Section 3.2.6, using empirical models. Froth velocity is measured and used in the model for air recovery, as shown in (2.1).
Not modelled	
Gas holdup	Gas hold-up is not commonly measured in real time on industrial flotation circuits, and no data on air hold-up was included in the industrial dataset used in this model development. There are conflicting views as to the significance of the gas holdup as a measure of the efficiency of gas dispersion or of flotation performance (Deglon, Egya-Mensah and Franzidis, 2000). Variations in air hold-up will be considered an unmeasured disturbance, and the effect of air hold-up will be compensated by adapting model parameters over time.

Table 3.14. Internal model variables.

Variable	Description
Modelled	
Superficial air velocity	Superficial air velocity is calculated from the measured volumetric airflow rate to each flotation cell and the surface area of the cell, assuming a uniform surface area throughout the flotation cell, as defined in (3.12).
Froth depth	Pulp levels are defined as model states, as shown in Table 3.13. The froth depth is calculated as the difference between the flotation cell height and the pulp level, plus the measured froth height above the lip. For deep froth layers, a simplifying assumption that the variation in froth height above the lip is negligible compared to the total froth depth can be used. This assumption does not imply that froth depth above the lip is not used in the calculation of air recovery as described in (2.1).
Mineral concentrations in all intermediate streams (grades)	Mineral masses in each flotation cell has been defined as states in Table 3.13. Mineral grades can be calculated from the mineral masses in the pulp and froth phases.
Densities of all streams	The mass and volume balances used to model the mineral and liquid masses in the flotation cells, as described in Table 3.13, can be used to calculate densities in flotation cells and the concentrate hopper. The effect of density on model states and parameters has not been modelled explicitly due to a limited dataset.
Feed, tailings and concentrate flow rates	The concentrate volumetric flow rate is modelled based on froth properties and air addition to each flotation cell, as described in Sections 3.2.3 and 3.2.5. The volumetric feed flow rate is defined as a measured disturbance (see Table 3.11), and the tailings flow rates can be calculated from the volume balance described in Section 3.2.1 based on the measured flotation cell pulp levels, L_k.
Not modelled	
Bias superficial velocity (mostly columns)	Wash water was not modelled as it was not used for the rougher flotation circuit that was modelled.

Table 3.15. Measured model outputs.

Symbol	Description
Flotation cell and concentrate hopper levels	Levels are typically measured using a float with a target plate and ultrasonic level transmitter and are considered measured outputs for the model.
Top-of-froth bubble diameter	The Sauter mean bubble diameter can be determined from froth images, and it is assumed that froth cameras are available on each flotation cell that is modelled.
Air recovery	The air recovery of each flotation cell can be calculated from the froth velocity, froth height above the lip, aeration rate of each flotation cell and cell dimensions, as defined in (2.1), and is considered a measured model output for the model.
Concentrate hopper grade	It is assumed that grade measurements using XRF or reflectance spectroscopy are available on the outflow from the concentrate hopper.
Concentrate hopper discharge volumetric flow rate	It is assumed that a volumetric flow measurement using a magnetic flow meter is available on the concentrate hopper discharge.
Concentrate hopper discharge density	It is assumed that the concentrate hopper discharge density is measured using a nuclear density meter or as an output from an XRF device.

3.4 DATASET

The dataset used for the industrial trial described in Hadler *et al.* (2010a) was reused in this study to fit model parameters to the model described in Section 3.2. The aim of the original industrial trial described in Hadler *et al.* (2010a) was to compare the concentrate grades and recoveries when different combinations of flotation cells are operated at air addition rates (Q_{air_k}) that maximise the air recoveries (α_k) for each cell, k. Q_{air_k} to four rougher and four scavenger cells were manipulated as part of the trial. Data from the four rougher cells were used to fit the model parameters for the circuit shown in Figure 3.1.

Different cells were operated at different froth depths (h_{f_k}) and a limited amount of variation occurred in h_{f_k} during the trial, but h_{f_k} was not intentionally varied as part of the trial. A series of six experiments were conducted on an industrial copper flotation circuit — five of the experiments having data collected for eight flotation cells and one on four cells only. Real-time operational data was supplemented with a mineralogical sampling campaign on the concentrate streams of each flotation cell, image analyses to quantify froth properties on each cell, and measurements of J_{g_k} for each cell using the *Anglo Platinum bubble sizer* instrument. Variables from the dataset that were used to fit model parameters for the model described in Section 3.2 are listed in Table 3.16.

Table 3.16. Variables used to fit model parameters.

Variable	Description
Real-time operational data	
Volumetric feed flow rate to cell 1 (m^3/h)	Value of Q_{F_1} in the model.
Feed density for flotation cell 1 (% solids)	Value of C_{w_1} in the model.
Feed grade (% copper)	Feed grade of species 0 in the model (G_F^0).
Feed size (P80) (μ m)	Used to estimate d_{pmin} and d_{pmax} in the model by assuming a uniform distribution.
Rougher tailings grade (% copper)	Grade in cell 4 tailings stream (G_{T_4}).
Rougher levels (mm)	L_k in the model.
Rougher bank air flow rate (m^3/h)	Combined air flow rates (Q_{air_k}) to cells 1 and 2, and cells 3 and 4 respectively.
Survey data	
Combined concentrate grade from four rougher cells (%)	Steady-state value of G_H in the model.
Combined recovery from four rougher cells (%)	Steady-state recovery in the model.
Image analyses data	
Froth height above the lip (mm)	Used in the calculation of α_k.
Froth velocity (mm/s)	Used in the calculation of α_k.
Calculated air recovery	Calculated from the froth height above the lip, froth velocity and physical dimensions of the flotation cell as described in (2.1). α_k in the model.
Top of froth bubble diameter (mm)	D_{BF_k} in the model.
Anglo Platinum Bubble Sizer data	
Superficial gas velocity for each cell (mm/s)	J_{g_k} in the model.

3.5 MODEL PARAMETER FIT

The model parameters of the empirical models for D_{BF_k} and α_k that are described in Section 3.2.6 were fitted to the industrial data described in Hadler *et al.* (2010a). Model parameters for D_{BF_k} were determined using a least-squares fit on the data for each cell, k. α_{OS_k} and $K_{\alpha_{J_{g_k}}}$ were set to the average peak air recoveries (PAR) and J_{g_k} at PAR respectively, reported by Hadler *et al.* (2010a) for two experiments performed at PAR. The remaining model parameters for α_k ($K_{\alpha_{J_g}}$ and $K_{\alpha_{h_f}}$) were determined using a least-squares fit on the full data set. The model parameter values are shown in Table 3.17 and were fitted using the experimental results of five experiments that were reported by Hadler *et al.* (2010a).

For D_{BF_k}, an R^2 value of 0.99 was obtained, while the R^2 value for the model fit for α_k was lower but still reasonable at 0.82. The effect of outliers on the parameter fit and model statistics can potentially be reduced by removing the data points with the highest residuals from the dataset (Steyn and Sandrock, 2021). Due to the size of the dataset the full dataset was used to fit the empirical parameters shown in Table 3.17.

Table 3.17. Empirical model parameter values.

Symbol	Unit	Value	k=1	k=2	k=3	k=4
$K_{BF_{Jg}}$	s	0.529				
K_{BF_λ}	mm/s	0.313				
$K_{\alpha_{J_g}}$	s^2/mm^2	-0.0248				
$K_{\alpha_{h_f}}$	1/s	0.01				
D_{OS_k}	mm		9.79	6.35	8.55	5.93
$K_{\alpha_{J_{g_k}}}$	mm/s		7.20	7.30	7.00	6.63
α_{OS_k}	-		0.410	0.269	0.168	0.170

The dataset described in Section 3.4 did not contain any information to calibrate the valve constants, C_{v_k}, for each cell, k. As C_{v_k} is only used for level stabilisation — not for the optimisation of the flotation circuit — the values of C_{v_k} were arbitrarily chosen to provide the required tailings flow rates at valve openings of approximately 50% on all cells, to ensure adequate ranges for process control.

Data on the volumetric flow rate of concentrate to a concentrate hopper would typically be used to calibrate C_{PB}, but was not available in the dataset described in Section 3.4. Neethling and Cilliers (2009) defined the expected range of C_{PB} between 10 and 50, with a higher value of C_{PB} corresponding with higher water recovery, which in turn increases entrainment of both desired (copper) and gangue particles. An assumption was made that the main mechanism responsible for gangue minerals reporting to the concentrate stream, is entrainment (determined by C_{PB}) - not true flotation (determined by $K^{1,0}$ - the flotation rate constant for gangue minerals). An iterative procedure was hence followed to calibrate C_{PB}, $K^{0,0}$, and $K^{1,0}$ based on the dataset described in Section 3.4, by choosing $K^{0,0}$ to achieve the desired recovery of copper containing minerals, C_{PB} to achieve the desired concentrate grade (subject to the range defined by Neethling and Cilliers (2009)), and adjusting $K^{1,0}$ to achieve the desired grade when C_{PB} has insufficient range.

3.6 STEADY-STATE MODEL SIMULATION

Steady-state simulations were performed for a single flotation cell using the models described in Section 3.2 to show the dependence of the modelled variables on the controlled variables, J_{g_k} and h_{f_k} (as a function of L_{SP_k}). Operating ranges and model outputs were based on the industrial data reported by Hadler *et al.* (2010a). Simulation results of the empirical models of α_k and D_{BF_k}, as described in (3.33) and (3.34), are shown in Figure 3.3 and Figure 3.4 respectively. Concentrate water recovery was simulated based on (3.9), including the dependence of D_{BF_k} and α_k on h_{f_k} and J_{g_k}. Grade and recovery simulations are based on true flotation (3.15) and the simplified entrainment model (3.22). The same ranges that Hadler *et al.* (2010a) used for J_{g_k} and h_{f_k} were used in the simulations, and model parameters were fitted to obtain similar results for these variables, as reported by Hadler *et al.* (2010a). Note that the experimental trial conducted by Hadler *et al.* (2010a) focused on the effect of J_{g_k} on α_k and other process variables and that h_{f_k} was not varied intentionally as part of the test work.

The dependence of air recovery, α_k, on J_{g_k} and h_{f_k} is shown in Figure 3.3. The model fit for α_k resulted in a peak at $J_{g_k} \approx 8.4$mm/s. Figure 3.3 shows that maximum air recovery occurs at a lower value of J_{g_k} for shallower froths, as reported by Hadler *et al.* (2012).

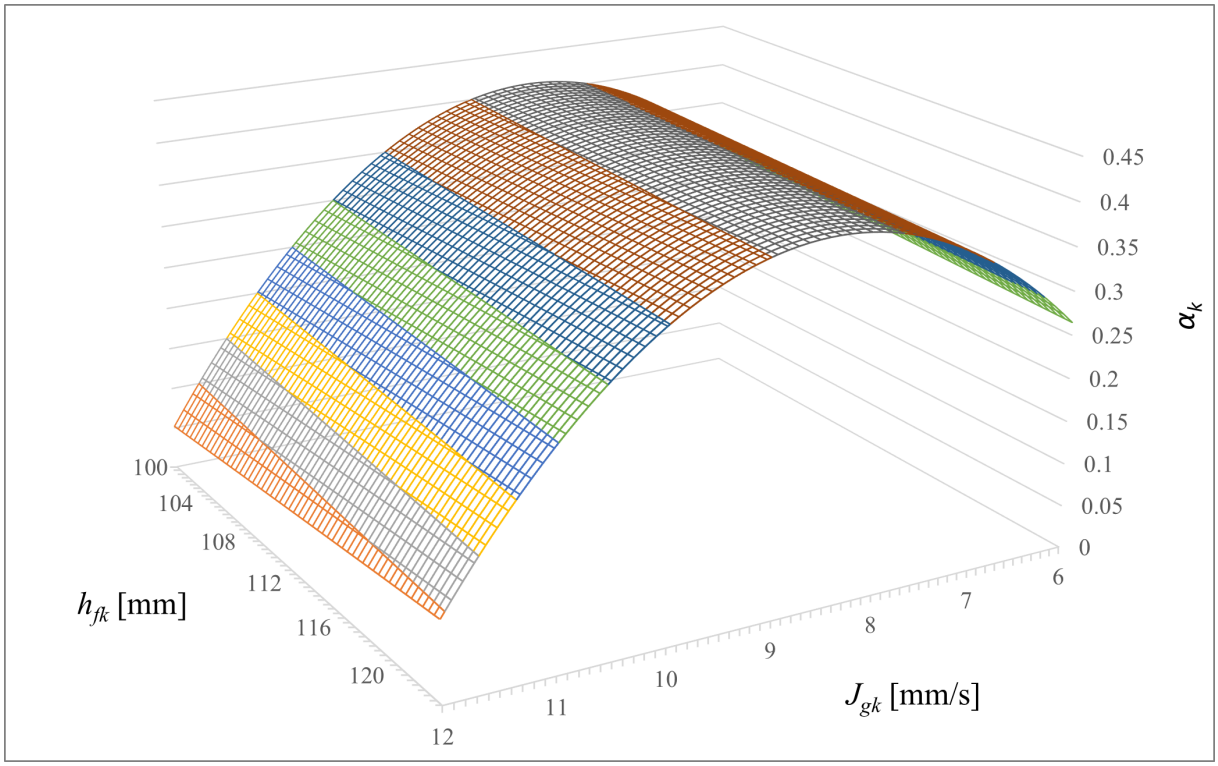

Figure 3.3. Air recovery, α_k, (3.34) as a function of J_{g_k} and h_{f_k}.

A plot of the top-of-froth bubble size, D_{BF_k}, is shown in Figure 3.4. An increase in h_{f_k} results in an increase in D_{BF_k} due to an increase in froth residence time λ_{air_k} with h_{f_k}. D_{BF_k} is defined as a linear function of J_{g_k} and λ_{air_k} (3.15). However, λ_{air_k} is inversely proportional to J_{g_k}, resulting in the non-linear response between J_{g_k} and D_{BF_k}.

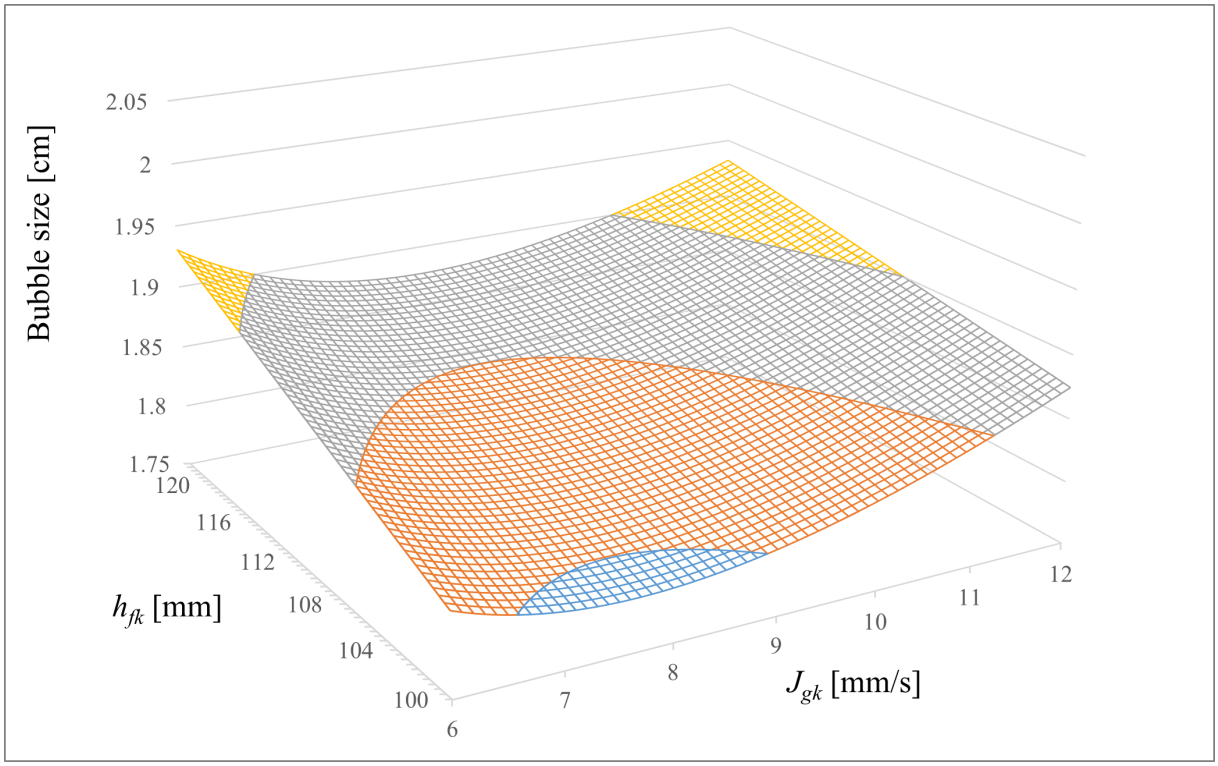

Figure 3.4. Top-of-froth bubble size, D_{BF_k}, (3.33) as a function of J_{g_k} and h_{f_k}.

The effect of J_{g_k} and h_{f_k} on true flotation is shown in Figure 3.5. An increase in J_{g_k} increases the bubble surface area that is available for hydrophobic particles to attach to. The effect of air recovery α_k on true flotation is clear from the correlation between α_k and true flotation.

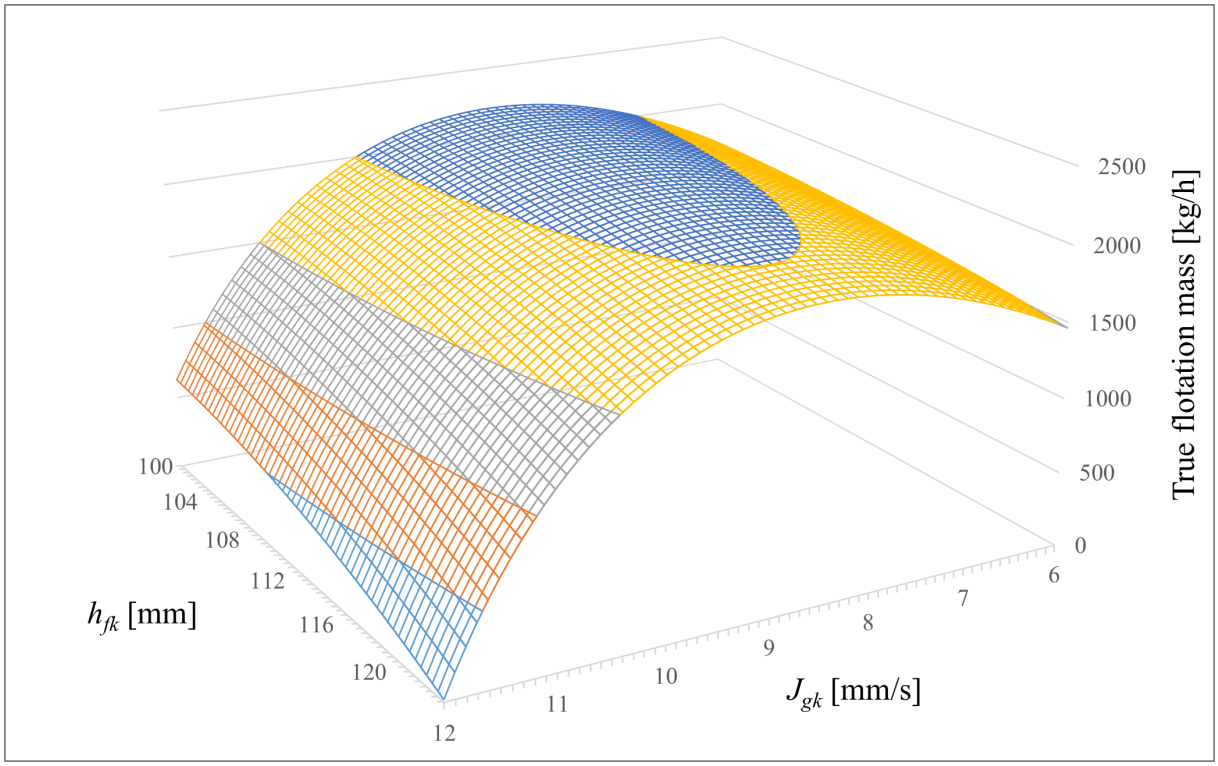

Figure 3.5. True flotation, $\frac{dM_k^{i,j}}{dt}$, (3.15) as a function of J_{g_k} and h_{f_k}.

Water recovery, Q_{C_k}, has a quadratic dependence on J_{g_k} and an inverse dependence on bubble size, which results in some interesting variations in entrainment over a range for J_{g_k} and h_{f_k}, as shown in Figure 3.6. Similar to the trend of the air recovery, α_k, shown in Figure 3.3, water recovery also has a peak, but the peaks in α_k and Q_{C_k} occur at different values of J_{g_k}.

The entrainment of gangue and copper-containing particles are strongly correlated with water recovery, Q_{C_k}. The entrained gangue mass flow rate and the mass flow rate of copper-containing minerals due to entrainment are shown in Figures 3.7 and 3.8. The reason that the peak in the entrainment of copper-containing minerals shown in Figure 3.8 does not correspond with the peak in the water recovery, Q_{C_k}, shown in Figure 3.6 is that the concentration of copper-containing minerals in the flotation cell was higher at high values of J_{g_k} due to α_k reducing true flotation, while the concentration of gangue minerals remained relatively constant. For the rougher flotation section that was modelled in this chapter, the mechanism of entrainment contributed a negligible fraction to the total mass flow rate of copper-containing minerals compared to the mechanism of true flotation.

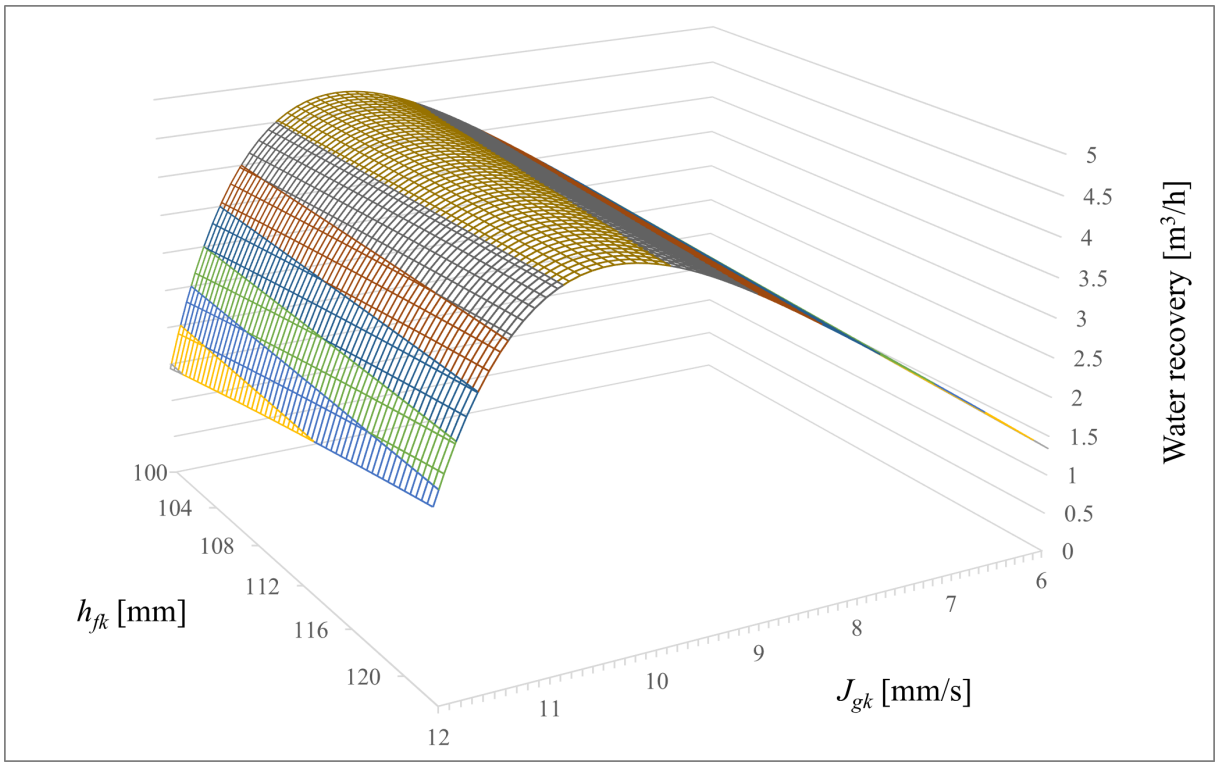

Figure 3.6. Water recovery, Q_{C_k}, (3.9) as a function of J_{g_k} and h_{f_k}.

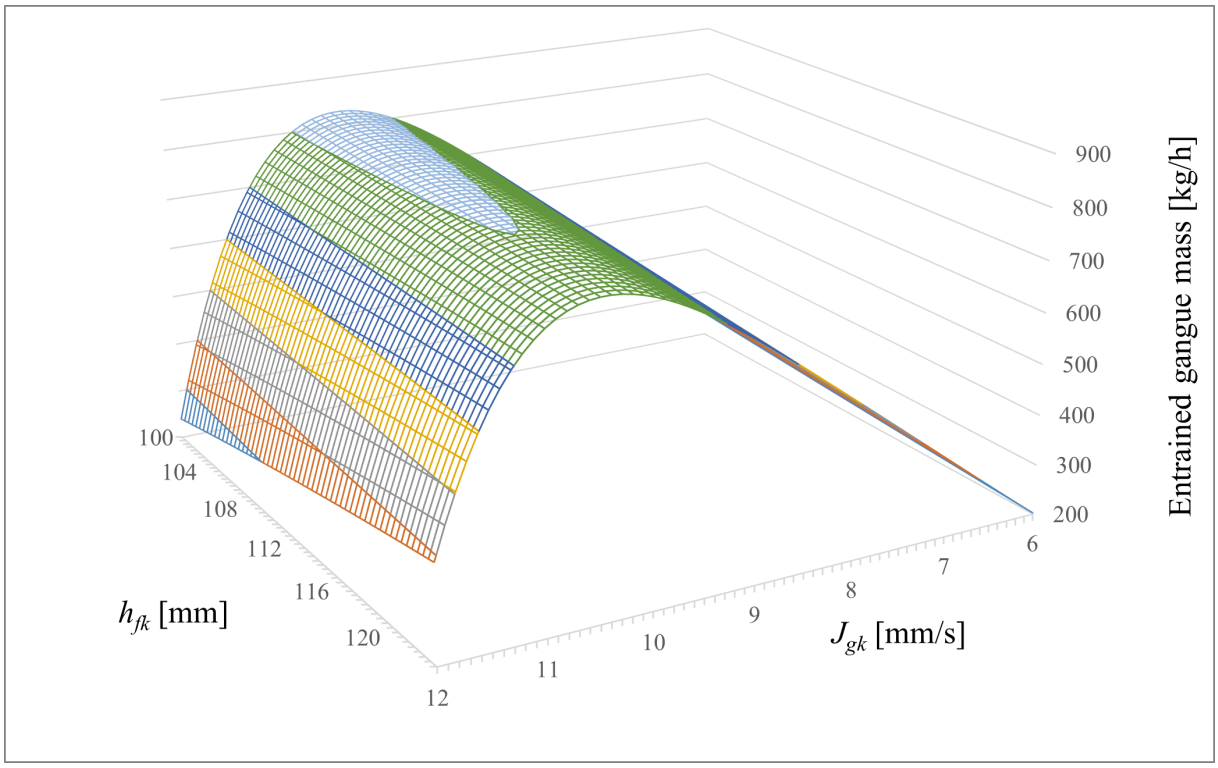

Figure 3.7. Gangue entrainment (second term in (3.24)) as a function of J_{g_k} and h_{f_k}.

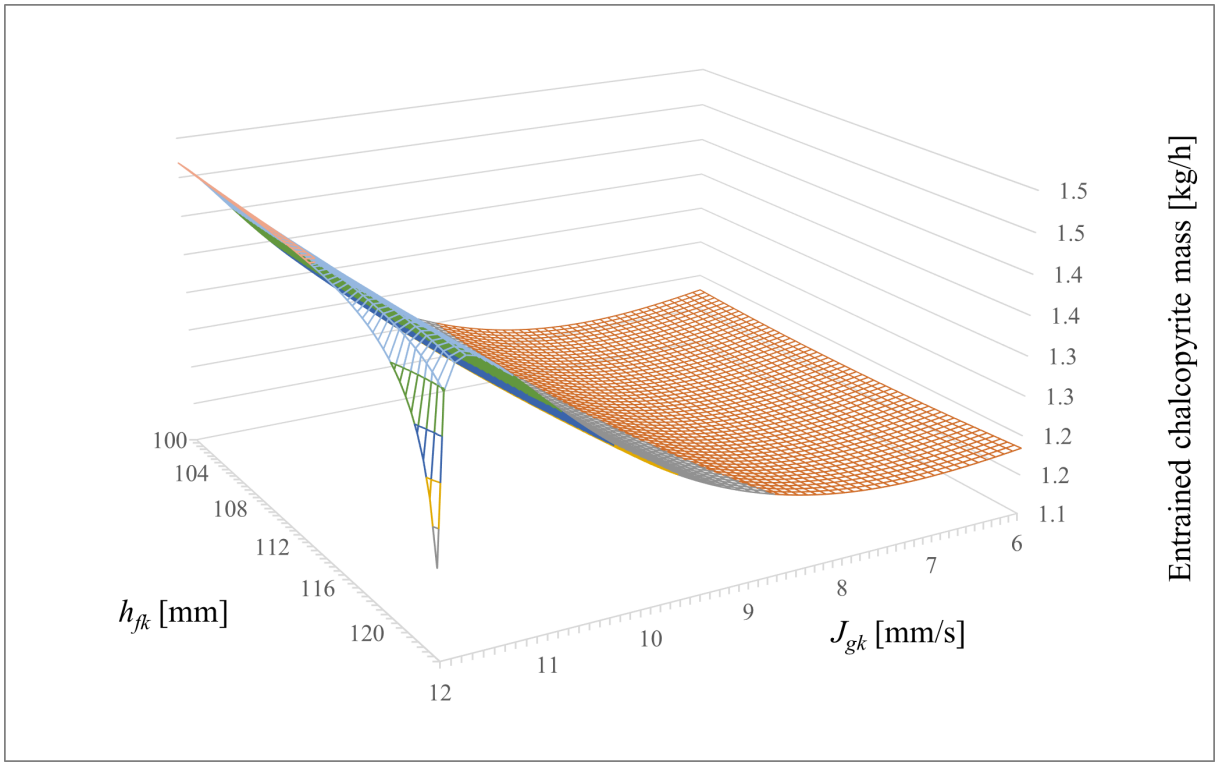

Figure 3.8. Copper-containing mineral entrainment (second term in (3.24)) as a function of J_{g_k} and h_{f_k}.

When true flotation and entrainment components are combined, the concentrate grade, as shown in Figure 3.9, increases with an increase in h_{f_k} and a decrease in J_{g_k} as expected. However, recovery, as shown in Figure 3.10, shows a strong dependence on air recovery. This implies that the same concentrate grade can be obtained at multiple recoveries, which confirms that h_{f_k} and J_{g_k} cannot be considered independently when grade and recovery are optimised in a flotation cell.

The maximum recovery for the single flotation cell simulation shown in Figure 3.10 is 26.2% when the cell is operated at J_{g_k} = 8.6 mm/s and h_{f_k} = 100 mm. Figure 3.9 shows a grade of 26.4% at this operating point, which can also be achieved at various other operating points. If the flotation cell was, for example, operated at J_{g_k} = 8.7 mm/s and h_{f_k} = 120 mm, the same grade of 26.4% would have been achieved but at a recovery of only 23.5%. In a flotation section with multiple flotation cells, there is still an opportunity to recover more of the desired minerals in downstream cells where upstream cells are not operated at their recovery peaks. The masses of desired minerals that are available in downstream cells are also dependent on the recoveries in upstream cells, as indicated by the mass balance (3.4). This quantitative example provides an indication of the potential benefit that model-based control could

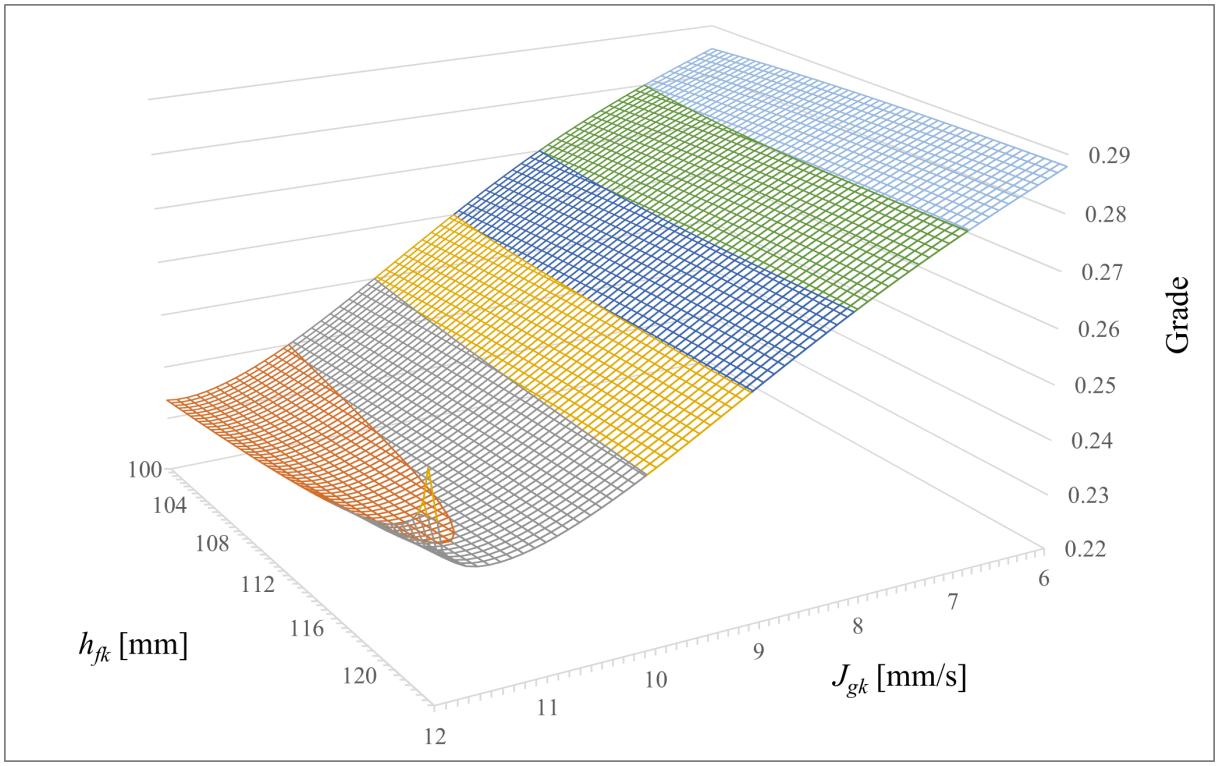

Figure 3.9. Concentrate grade, G_{C_k}, (3.26) as a function of J_{g_k} and h_{f_k}.

have on improving recoveries in flotation processes.

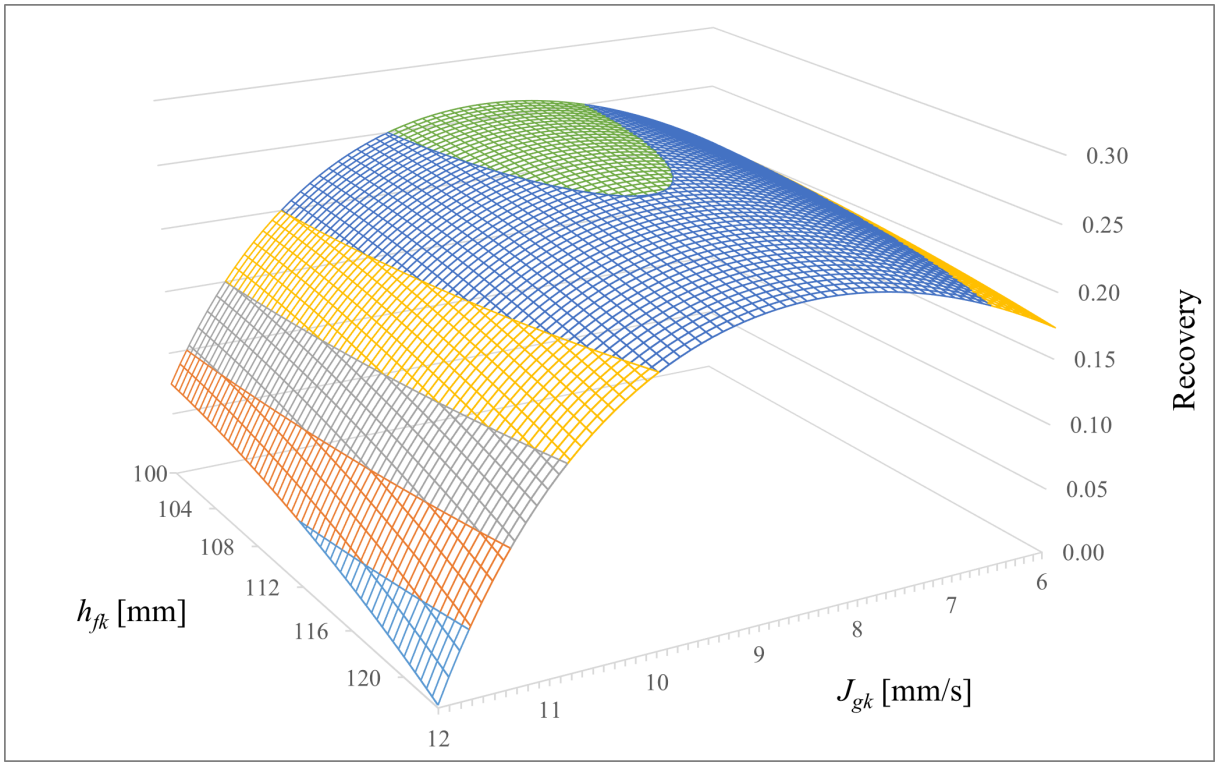

Figure 3.10. Concentrate Recovery, R_{C_k}, (3.27) as a function of J_{g_k} and h_{f_k}.

3.7 DISCUSSION

The flotation model described in Section 3.2 can model the effect of variations in aeration rate, J_{g_k}, and froth depth, h_{f_k}, on multiple mineral species and show how the contribution from each species influences the concentrate hopper and tailings grades, and the recovery of a flotation section. The model was compared to the key variables for flotation processes that were identified in Chapter 2, and it was shown in Section 3.3 that the flotation model is comprehensive enough to cover the majority of the key variables that have been identified. Where variables were not modelled due to the absence of a real-time measurement device or experimental data, a motivation was provided and it was discussed how the effect of unmeasured variables will be included in the model by real-time adjustment of model parameters. For example, the effect of all factors contributing to the attachment and detachment of particles in the pulp are lumped together in a pseudo rate constant, $K^{i,j}$, as defined in (3.15). In addition, it was shown that the model outputs correspond with real-time measurements that are commonly available on industrial flotation circuits.

The fact that all modelled outputs correspond with real-time measurements that are commonly available on industrial flotation circuits, does not imply that all model parameters and states can be estimated

from available real-time measurements. An observability and controllability analysis is performed in Chapter 4 to evaluate if the model states and parameters can be estimated continuously and hence automatically adjust to changes in operating conditions, rather than relying on manual sampling campaigns to adjust model parameters.

A key aspect of the model described in this chapter is the ability to continuously estimate (and hence update) model parameters using real-time measurements (as shown in Chapter 4). Future work to expand the model should ensure that any additional model parameters that are added can also be estimated from real-time (or frequently updated) measurements to ensure that model accuracy is maintained over time.

D_{BF_k} shown in Figure 3.4 varies by less than 2 mm over the simulated operating range, which seem small compared to variability in D_{BF_k} that is commonly observed on industrial flotation circuits. Additional parameters (potentially reagents) could be included in future models to enhance the existing model of D_{BF_k} as a function of h_{f_k} and J_{g_k}.

An *instantaneous* recovery was defined in (3.26) using a steady-state approximation to quantify flotation circuit performance. The *instantaneous* recovery could differ from *true* recovery during transient (non steady-state) periods and in the presence of noise or short-term variations in the feed or concentrate streams. Such discrepancies between *instantaneous* and *true* recovery is not a reason for concern, as all the simulation studies presented in Chapter 5 were done over sufficiently long periods to allow the flotation circuit to reach a steady state, at which point differences between *instantaneous* and *true* recoveries would be negligible.

CHAPTER 4 MODEL ANALYSIS

4.1 CHAPTER OVERVIEW

A froth flotation model was derived in Chapter 3, showing that the key variables that are required to model froth flotation are included in the model and that the model outputs correspond with real-time measurements that are commonly available on industrial flotation plants. While the model described in Chapter 3 is not the most comprehensive model available in the literature, the model was designed with the aim of estimating key model parameters from real-time data rather than relying on potentially infrequent sampling campaigns to update model parameters.

In this chapter, a state observability and state controllability analysis is performed on the model described in Chapter 3 to confirm that the model is suitable for real-time parameter estimation and dynamic control and optimisation applications. Observability is a modelling property that describes the possibility of inferring the internal state of a system from observations of its output. A related property, structural identifiability, refers to the theoretical possibility of determining the parameter values from the output (Xia and Moog, 2003). The benefit of having a state observable and parameter identifiable system is that variations in model parameters can be observed from real-time measured model outputs, and model parameters can be updated in real time. In addition, the model parameters can adjust to short-term variations in operating conditions instead of using outdated parameters in a model that is used for automatic control, or configuring parameters conservatively to ensure safe operation at a worst-case operating point.

In Section 4.2, the key equations of the flotation model described in Chapter 3 are repeated. The theory of state observability and state controllability is summarised in Section 4.3. In Section 4.4, a state observability analysis is performed to show that the model parameters and states can be estimated from the available set of real-time measurements. This is followed by a state controllability analysis in

Section 4.5 to show that the variables defined as model inputs can drive the process states towards a desired operating region. The results are discussed in Section 4.6 and concluding remarks are given in Section 4.7.

4.2 FLOTATION MODEL SUMMARY

The objective of a state observability analysis is to determine if all the model states that are defined in Tables 3.6 and 3.7, and the model parameters defined in Table 3.5 can be estimated from real-time measurements that are typically available on industrial flotation circuits, as shown in Table 3.8. Tables 3.5, 3.6, 3.7 and 3.8 in Chapter 3 are repeated as Tables 4.1, 4.2, 4.3 and 4.4.

Table 4.1. Model parameters to be estimated.

Symbol	Unit	Description
$K_{BF_{J_g}}$	s	Effect of the superficial gas velocity on the mean top-of-froth bubble diameter
K_{BF_λ}	mm/s	Effect of the average froth residence time on the mean top-of-froth bubble diameter
$K_{\alpha_{J_{g_k}}}$	mm/s	Value of the superficial air velocity in cell k where air recovery is maximised when $h_{f_k} = 0$
$K_{\alpha_{J_g}}$	s^2/mm^2	Effect of the difference between J_{g_k} and J_{g0} squared on air recovery
$K_{\alpha_{h_f}}$	1/s	Effect of a change in h_{f_k} on the superficial air velocity where air recovery is maximised
α_{OS_k}	-	Offset included in steady-state air recovery equation, α_{SSk} in cell k
D_{OS_k}	mm	Offset included in the steady-state top-of-froth bubble diameter equation, D_{BFSS_k} in cell k
C_{v_k}	$m^{5/2}/h$	Valve constant for cell k
C_{PB}	-	Plateau border drag coefficient
$K^{i,j}$	-	Flotation rate-constant for species i, class j

Table 4.2. States for each flotation cell.

Symbol	Unit	Description	State equation	Online measured
D_{BF_k}	mm	Top of froth bubble diameter	$\frac{d}{dt}D_{BF_k} = \frac{D_{BFSS_k} - D_{BF_k}}{\lambda_{air_k}}$	Yes
α_k	-	Air recovery	$\frac{d}{dt}\alpha_k = \frac{\alpha_{SS_k} - \alpha_k}{\lambda_{air_k}}$	Yes*
L_k	m	Cell pulp level	$\frac{d}{dt}L_k = (Q_{F_k} - Q_{T_k} - Q_{C_k})/A_k$	Yes
$M_k^{i,j}$	kg	Masses in flotation cell	$\frac{d}{dt}M_k^{i,j} = \dot{M}_{F_k}^{i,j} - \dot{M}_{T_k}^{i,j} - \dot{M}_{C_k}^{i,j}$	No
J_{g_k}	mm/s	Superficial gas velocity	$\frac{d}{dt}J_{gk} = \frac{J_{gSP_k} - J_{g_k}}{\tau_{Jg_k}}$	No**

*'measured' as indicated in (2.1)

**J_{gSP_k} is 'measured' as per (3.12) **J_{g_k} is an unmeasured transient

Table 4.3. States for the concentrate hopper.

Symbol	Unit	Description	State equation	Online measured
L_H	m	Hopper level	$A_H \frac{dL_H}{dt} = \sum_{k=1}^{N} Q_{C_k} - Q_H$	Yes
$M_H^{i,j}$	kg	Masses in hopper	$\frac{d}{dt}M_H^{i,j} = \sum_{k=1}^{N} \dot{M}_{C_k}^{i,j} - \frac{M_H^{i,j}}{L_H A_H} Q_H$	No

Table 4.4. Additional measured model outputs.

Symbol	Unit	Description	Output equation
G_H	-	Grade in hopper	$G_H = \frac{\sum_{j=1}^{n} M_H^{0,j}}{\sum_{i=1}^{m}\sum_{j=1}^{n} M_H^{i,j}}$
G_{T_4}	-	Grade in cell 4 tailings stream	$G_{T_4} = \frac{\sum_{j=1}^{n} M_4^{0,j}}{\sum_{i=1}^{m}\sum_{j=1}^{n} M_4^{i,j}}$
C_{w_H}	%	Percent solids by mass in the hopper	$C_{w_H} = 100\frac{\sum_{i=1}^{m}\sum_{j=1}^{n} M_H^{i,j}}{\sum_{i=1}^{m}\sum_{j=1}^{n} M_H^{i,j} + \rho\left(A_H L_H - \sum_{i=1}^{m}\sum_{j=1}^{n} \frac{M_H^{i,j}}{\rho_s^{i,j}}\right)}$
C_{w_T}	%	Percent solids by mass in the tailings	$C_{w_T} = 100\frac{\sum_{i=1}^{m}\sum_{j=1}^{n} M_4^{i,j}}{\sum_{i=1}^{m}\sum_{j=1}^{n} M_4^{i,j} + \rho\left(A_4 L_4 - \sum_{i=1}^{m}\sum_{j=1}^{n} \frac{M_4^{i,j}}{\rho_s^{i,j}}\right)}$

4.3 THEORETICAL BACKGROUND

The non-linear flotation model can be represented in a state-space format, with $\mathbf{x}$ as the states, $\mathbf{u}$ as the manipulated variables and $\mathbf{y}$ as the measured outputs

$$\begin{aligned} \frac{d\mathbf{x}}{dt} &= \mathbf{f}(t,\mathbf{x},\mathbf{u}) \\ \mathbf{y} &= \mathbf{h}(t,\mathbf{x},\mathbf{u})\,. \end{aligned} \tag{4.1}$$

The non-linear system can be linearised at a steady-state operating point, $(\mathbf{x}_0,\mathbf{u}_0)$, with the deviation variables defined as $\delta\mathbf{x} = \mathbf{x} - \mathbf{x}_0$, $\delta\mathbf{u} = \mathbf{u} - \mathbf{u}_0$ and $\delta\mathbf{y} = \mathbf{y} - \mathbf{y}_0$, as

$$\begin{aligned} \frac{d}{dt}\delta\mathbf{x} &= \mathbf{A}\delta\mathbf{x} + \mathbf{B}\delta\mathbf{u} \\ \delta\mathbf{y} &= \mathbf{C}\delta\mathbf{x} + \mathbf{D}\delta\mathbf{u}\,. \end{aligned} \tag{4.2}$$

The system matrices, $\mathbf{A}$, $\mathbf{B}$, $\mathbf{C}$ and $\mathbf{D}$ can be calculated as

$$\begin{aligned} \mathbf{A} &= \left.\frac{\partial \mathbf{f}(t,\mathbf{x},\mathbf{u})}{\partial \mathbf{x}}\right|_{\mathbf{x}_0,\mathbf{u}_0} & \mathbf{B} &= \left.\frac{\partial \mathbf{f}(t,\mathbf{x},\mathbf{u})}{\partial \mathbf{u}}\right|_{\mathbf{x}_0,\mathbf{u}_0} \\ \mathbf{C} &= \left.\frac{\partial \mathbf{h}(t,\mathbf{x},\mathbf{u})}{\partial \mathbf{x}}\right|_{\mathbf{x}_0,\mathbf{u}_0} & \mathbf{D} &= \left.\frac{\partial \mathbf{h}(t,\mathbf{x},\mathbf{u})}{\partial \mathbf{u}}\right|_{\mathbf{x}_0,\mathbf{u}_0}\,. \end{aligned} \tag{4.3}$$

Skogestad and Postlehwaite (2005) describe how state observability and state controllability can be determined for linear systems by calculating the rank of an observability ($\mathcal{O}$) and controllability ($\mathcal{C}$) matrix respectively. If the linearised system is observable or controllable, it implies that the non-linear system is also observable or controllable (Hermann and Krener, 1977; le Roux *et al.*, 2017). All the states $\mathbf{x}$ are said to be observable or controllable from the input vector $\mathbf{u}$ and output vector $\mathbf{y}$ if $\mathcal{O}$ or $\mathcal{C}$ has full rank, n, where n is the dimension of the state vector $\mathbf{x}$. This technique can also be used to determine if model parameters can be estimated from $\mathbf{u}$ and $\mathbf{y}$, by augmenting the state vector $\mathbf{x}$, with the model parameters as states without any dynamics (Simon, 2006). The state observability matrix $\mathcal{O}$ is defined as

$$\mathcal{O} = \begin{bmatrix} \mathbf{C} \\ \mathbf{CA} \\ \vdots \\ \mathbf{CA}^{n-1} \end{bmatrix}, \tag{4.4}$$

and the state controllability matrix $\mathcal{C}$ as

$$\mathcal{C} = \begin{bmatrix} \mathbf{B} & \mathbf{AB} & \mathbf{A}^2\mathbf{B} & \dots & \mathbf{A}^{n-1}\mathbf{B} \end{bmatrix}. \tag{4.5}$$

If the rank of $\mathcal{O}$ as described in (4.4) does not confirm that the linearised system described in (4.2) is state observable, it might still be possible to estimate the model states and parameters by using a non-linear observer, such as a moving horizon estimator (MHE). For the non-linear observability analysis, the flotation model must be described in a multi-input-multi-output control-affine form as

$$\begin{aligned} \frac{d\mathbf{x}}{dt} &= \mathbf{f}(t,\mathbf{x}) + \mathbf{g}(t,\mathbf{x})\mathbf{u} \\ \mathbf{y} &= \mathbf{h}(t,\mathbf{x}), \end{aligned} \tag{4.6}$$

where $dim(x) = n$ and $dim(y) = m$.

The observability co-distribution for the system described in (4.6) is defined by Hermann and Krener (1977) as

$$d\mathcal{O} = span\left\{dh_j, dL_f h_f, \ldots, dL_f^{n-1} h_j\right\}, \tag{4.7}$$

where L_f^k is the k-th repeated Lie derivative of the scalar function $h_j(x)$ along the vector field $f(x)$, and d is the exterior derivative (Doyle and Henson, 1997). If the system defined in (4.6) satisfies the observability rank condition in that the $d\mathcal{O}$ that is defined in (4.7) has dimension n, the system is locally (weakly) observable in a region around x_0 where (4.7) is evaluated.

4.4 OBSERVABILITY ANALYSIS

The observability analyses shown in Sections 4.4.1 and 4.4.2 evaluate different combinations of model states and measurements to show which measurements are required to estimate specific sets of parameters. Should an observability analysis return a negative result, the interpretation is that all model states and parameters can not be estimated using the defined model equations and measurements. An alternative model definition with additional measurements (which may include derivatives of existing measurements), a reduced parameter set or alternative model equations would be necessary to estimate all the model states and parameters. The observability analysis is performed using the linearised system and $\mathcal{O}$, as defined in (4.4). $d\mathcal{O}$ as defined in (4.7) is only used if the rank of $\mathcal{O}$ is less than n, i.e. the linearised system is not observable.

The dynamic flotation model described in Chapter 3 can be analysed by dividing it into two parts: the parameter estimation for froth bubble size, D_{BF_k}, and air recovery, α_k (see Section 4.4.1), and the volume and the mass balances (see Section 4.4.2).

4.4.1 Parameter estimation of froth bubble size and air recovery

The state equations for D_{BF_k} and α_k are shown in Table 4.2. In Section 3.2.6 $K_{BF_{J_g}}$, K_{BF_λ} and D_{OS_k} were estimated from multiple steady-state measurements of D_{BF_k}, J_{g_k} and h_{f_k}. Similarly, linear regression was used to estimate $K_{\alpha_{J_g}}$ and $K_{\alpha_{h_f}}$ based on multiple steady-state measurements of α_k, J_{g_k} and h_{f_k} and experimentally determined values for α_{OS_k} and $K_{\alpha_{J_{g_k}}}$.

In this section an observability analysis is performed to verify that the model parameters $K_{BF_{J_g}}$, K_{BF_λ}, $K_{\alpha_{J_{g_k}}}$, $K_{\alpha_{J_g}}$, $K_{\alpha_{h_{f_k}}}$, $K_{\alpha_{h_f}}$, D_{OS_k} and α_{OS_k} can be estimated from continuously varying measurements, rather than relying on steady-state approximations and experimental results. Note that the *measurement* of α_k uses the froth height above the lip h, as defined in (2.1). The state equation for α_k was defined in (3.34) as a function of h_{f_k}, which only depends on the flotation cell level, L_k.

For a flotation cell k, the state ($\mathbf{x}_{ck}$), output ($\mathbf{y}_{ck}$), input ($\mathbf{u}_{ck}$) and parameter ($\mathbf{x}_{p0}$ and $\mathbf{x}_{pk}$) vectors are given by

$$\begin{aligned}
\mathbf{y}_{ck} &= [D_{BF_k}, \alpha_k, L_k]^T \\
\mathbf{x}_{ck} &= [D_{BF_k}, \alpha_k, L_k, J_{g_k}]^T \\
\mathbf{u}_{ck} &= [J_{gSP_k}, z_k]^T \\
\mathbf{x}_{p0} &= [K_{BF_{J_g}}, K_{BF_\lambda}, K_{\alpha_{J_g}}, K_{\alpha_{h_f}}]^T \\
\mathbf{x}_{pk} &= [K_{\alpha_{J_{g_k}}}, D_{OS_k}, \alpha_{OS_k}]^T .
\end{aligned} \tag{4.8}$$

For a single flotation cell, the linearised system matrices described in (4.3) can be calculated from the vectors $\mathbf{y}_1$, $\mathbf{u}_1$, $\mathbf{x}_1$, and $\mathbf{x}_{aug1}$ that are defined as

$$\begin{aligned}
\mathbf{y}_1 &= [\mathbf{y}_{c1}] \\
\mathbf{x}_1 &= [\mathbf{x}_{c1}] \\
\mathbf{u}_1 &= [\mathbf{u}_{c1}] \\
\mathbf{x}_{aug1} &= [\mathbf{x}_1^T, \mathbf{x}_{p0}^T, \mathbf{x}_{p1}^T]^T
\end{aligned} , \tag{4.9}$$

where $\mathbf{x}_{aug1}$ is the augmented state matrix comprising the state ($\mathbf{x}_1$) and parameter ($\mathbf{x}_{p0}$ and $\mathbf{x}_{p1}$) vectors.

For two flotation cells, the linearised system matrices described in (4.3) can be calculated from the vectors $\mathbf{y}_2$, $\mathbf{u}_2$, $\mathbf{x}_2$, and $\mathbf{x}_{aug2}$ that are defined as

$$\begin{aligned} \mathbf{y}_2 &= [\mathbf{y}_{c1}^T, \mathbf{y}_{c2}^T]^T \\ \mathbf{x}_2 &= [\mathbf{x}_{c1}^T, \mathbf{x}_{c2}^T]^T \\ \mathbf{u}_2 &= [\mathbf{u}_{c1}^T, \mathbf{u}_{c2}^T]^T \\ \mathbf{x}_{aug2} &= [\mathbf{x}_2^T, \mathbf{x}_{p0}^T, \mathbf{x}_{p1}^T, \mathbf{x}_{p2}^T]^T \end{aligned} . \tag{4.10}$$

Similarly, for three flotation cells, the vectors are given by

$$\begin{aligned} \mathbf{y}_3 &= [\mathbf{y}_{c1}^T, \mathbf{y}_{c2}^T, \mathbf{y}_{c3}^T]^T \\ \mathbf{x}_3 &= [\mathbf{x}_{c1}^T, \mathbf{x}_{c2}^T, \mathbf{x}_{c3}^T]^T \\ \mathbf{u}_3 &= [\mathbf{u}_{c1}^T, \mathbf{u}_{c2}^T, \mathbf{u}_{c3}^T]^T \\ \mathbf{x}_{aug3} &= [\mathbf{x}_3^T, \mathbf{x}_{p0}^T, \mathbf{x}_{p1}^T, \mathbf{x}_{p2}^T, \mathbf{x}_{p3}^T]^T \end{aligned} , \tag{4.11}$$

and for four flotation cells, as for the industrial data provided by Hadler *et al.* (2010b), the vectors are given by

$$\begin{aligned} \mathbf{y}_4 &= [\mathbf{y}_{c1}^T, \mathbf{y}_{c2}^T, \mathbf{y}_{c3}^T, \mathbf{y}_{c4}^T]^T \\ \mathbf{x}_4 &= [\mathbf{x}_{c1}^T, \mathbf{x}_{c2}^T, \mathbf{x}_{c3}^T, \mathbf{x}_{c4}^T]^T \\ \mathbf{u}_4 &= [\mathbf{u}_{c1}^T, \mathbf{u}_{c2}^T, \mathbf{u}_{c3}^T, \mathbf{u}_{c4}^T]^T \\ \mathbf{x}_{aug4} &= [\mathbf{x}_4^T, \mathbf{x}_{p0}^T, \mathbf{x}_{p1}^T, \mathbf{x}_{p2}^T, \mathbf{x}_{p3}^T, \mathbf{x}_{p4}^T]^T \end{aligned} . \tag{4.12}$$

The results of the state observability analysis for one, two, three and four flotation cells are shown in Table 4.5.

Table 4.5. Results of the state observability analysis for α_k and D_{BF_k}.

Number of cells (q)	dim($x_{aug\,q}$)	Rank of $\mathcal{O}$	Rank of d$\mathcal{O}$	Observable
1	11	6	9	No
2	18	12	17	No
3	25	18	24	No
4	32	24	31	No

From Table 4.5, it can be seen that the augmented state vector is not observable using a linear or non-linear observer. The analysis was thus repeated with a smaller parameter set. It is assumed that the

parameter determining the curvature of the air recovery α_k ($K_{\alpha_{h_f}}$) does not change significantly over time and that the position of the peak in air recovery is a more important parameter to estimate over time. $K_{\alpha_{J_g}}$ was thus removed from the definition of $\mathbf{x}_{p0}$ in (4.8), and (4.8) was replaced with

$$\begin{aligned}
\mathbf{y}_{ck} &= [D_{BF_k}, \alpha_k, L_k]^T \\
\mathbf{x}_{ck} &= [D_{BF_k}, \alpha_k, L_k, J_{g_k}]^T \\
\mathbf{u}_{ck} &= [J_{gSP_k}, z_k]^T \qquad . \\
\mathbf{x}_{p0} &= [K_{BF_{Jg}}, K_{BF_\lambda}, K_{\alpha_{h_f}}]^T \\
\mathbf{x}_{pk} &= [K_{\alpha_{J_{g_k}}}, D_{OS_k}, \alpha_{OS_k}]^T
\end{aligned} \tag{4.13}$$

The results of the observability analysis of the system described in (4.9), (4.10), (4.11) and (4.12), using the definition of $\mathbf{x}_{p0}$ in (4.13), are shown in Table 4.6.

Table 4.6. Results of the state observability analysis for α_k and D_{BF_k} with a reduced parameter set.

Number of cells (q)	dim($x_{aug\,q}$)	Rank of $\mathcal{O}$	Rank of d$\mathcal{O}$	Observable
1	10	6	9	No
2	17	12	17	Yes
3	24	18	24	Yes
4	31	24	31	Yes

From Table 4.6, it can be seen that the augmented state vector is state observable for two or more flotation cells but only when a non-linear estimator such as an MHE is used, as only $d\mathcal{O}$ meets the rank requirements. The model parameters ($K_{BF_{Jg}}$, K_{BF_λ}, $K_{\alpha_{J_{g_k}}}$, $K_{\alpha_{h_f}}$, D_{OS_k} and α_{OS_k}) that are used in the models for α_k and D_{BF_k} can thus only be estimated from dynamic process data using a non-linear estimator.

Alternative output vectors (y_{ck}), including derivatives of measurements, were not considered, as the measurements of α_k and D_{BF_k} are expected to be noisy. Should only a linear state estimator be available, the use of derivatives of α_k or D_{BF_k} in the output vectors may need to be considered, or simpler models could be used for α_k or D_{BF_k}, as used by Oosthuizen *et al.* (2021) to obtain a state observable and parameter identifiable system when three flotation cells were considered.

$K_{BF_{J_g}}$ is only identifiable if the dynamic response of J_{g_k} as shown in (3.35) is included in the model. When J_{g_k} does not vary $K_{BF_{J_g}}$ would not be identifiable and the estimate of $K_{BF_{J_g}}$ could drift over time. By adding a small perturbation to J_{gSP_k} it could be ensured that J_{g_k} would change over time and that $K_{BF_{J_g}}$ would remain identifiable. However, this is a limitation of the model which—together with the limited sensitivity of D_{BF_k} to variations in J_{g_k} and λ_{air_k}—cast some doubt on the value of including D_{BF_k} in the model. D_{BF_k} will be included in subsequent model analyses and simulations, but it is recommended that the model for D_{BF_k} be revised in future versions.

4.4.2 Parameter estimation including the mass and volume balances

In this section, the observability analysis done in Section 4.4.1 is extended to include all the model parameters listed in Table 4.1, all the states listed in Tables 4.2 and 4.3, and the model outputs listed in Table 4.4. Note that the parameter $K_{\alpha_{J_g}}$ is excluded from the parameter vector, similar to the model definition in (4.13).

For the full flotation model shown in Tables 4.2–4.4, the state ($\mathbf{x}_{ck}$), output ($\mathbf{y}_{ck}$), input ($\mathbf{u}_{ck}$) and parameter ($\mathbf{x}_{pk}$) vectors for a flotation cell k are given by

$$\begin{aligned}
\mathbf{y}_{ck} &= [D_{BF_k}, \alpha_k, L_k]^T \\
\mathbf{x}_{ck} &= [D_{BF_k}, \alpha_k, L_k, M_k^{0,0}, M_k^{1,0}, J_{g_k}]^T \\
\mathbf{u}_{ck} &= [J_{gSP_k}, z_k]^T \\
\mathbf{x}_{pk} &= [C_{v_k}, K_{\alpha_{J_{g_k}}}, D_{OS_k}, \alpha_{OS_k}]^T
\end{aligned} \quad . \tag{4.14}$$

Compared to (4.13), the state vector ($\mathbf{x}_{ck}$) has been extended to also include the states for the two mineral species $M_k^{0,0}$ (chalcopyrite) and $M_k^{1,0}$ (gangue minerals), as used by Hadler *et al.* (2010a).

Some variables are relevant to the entire flotation section, such as the states and measurements of the concentrate hopper and the measurements of the tailings stream from the last flotation cell in the rougher section. For the rougher flotation section model that is evaluated in this section, the state ($\mathbf{x}_H$),

output ($\mathbf{y}_H$), input ($\mathbf{u}_H$) and parameter ($\mathbf{x}_{pH}$) vectors are given by

$$\begin{aligned}\mathbf{y}_H &= [L_H, C_{wH}, G_H, C_{wT}, G_{T4}]^T \\ \mathbf{x}_H &= [L_H, M_H^{0,0}, M_H^{1,0}]^T \\ \mathbf{u}_H &= [Q_H]^T \\ \mathbf{x}_{pH} &= [K_{BF_{Jg}}, K_{BF_\lambda}, K_{\alpha_{h_f}}, C_{PB}, K^{0,0}, K^{1,0}]^T\end{aligned}, \tag{4.15}$$

with all the variables defined in Tables 4.1-4.4.

The linearised system matrices described in (4.3) for the flotation section comprising four flotation cells and a concentrate hopper can be calculated by combining (4.14) and (4.15) to yield the vectors $\mathbf{y}_5$, $\mathbf{u}_5$, $\mathbf{x}_5$ and $\mathbf{x}_{aug3}$ that are defined as

$$\begin{aligned}\mathbf{y}_5 &= [\mathbf{y}_{c1}^T, \mathbf{y}_{c2}^T, \mathbf{y}_{c3}^T, \mathbf{y}_{c4}^T, \mathbf{y}_H^T]^T \\ \mathbf{x}_5 &= [\mathbf{x}_{c1}^T, \mathbf{x}_{c2}^T, \mathbf{x}_{c3}^T, \mathbf{x}_{c4}^T, \mathbf{x}_H^T]^T \\ \mathbf{u}_5 &= [\mathbf{u}_{c1}^T, \mathbf{u}_{c2}^T, \mathbf{u}_{c3}^T, \mathbf{u}_{c4}^T, \mathbf{u}_H^T]^T \\ \mathbf{x}_{aug5} &= [\mathbf{x}_5^T, \mathbf{x}_{p1}^T, \mathbf{x}_{p2}^T, \mathbf{x}_{p3}^T, \mathbf{x}_{p4}^T, \mathbf{x}_{p_H}^T]^T\end{aligned}. \tag{4.16}$$

The dimensions of the vectors defined in (4.14), (4.15) and (4.16) are summarised in Table 4.7.

The observability analysis was performed for the system of four flotation cells and a concentrate hopper. Linear system matrices **A**, **B**, **C** and **D** were calculated as described in (4.3), using the model variables defined in Table 4.16. The observability matrix $\mathcal{O}$, as shown in (4.4), was calculated for the linear observability analysis, and the matrix $d\mathcal{O}$ for the non-linear analysis. The results of the observability analyses are shown in Table 4.8.

The rank of the observability matrix $\mathcal{O}$, as defined in (4.4), was calculated to be 42 when the matrices **C**, **CA** and $\mathbf{CA}^2$ were included in $\mathcal{O}$. As the dimension of $\mathbf{x}_{aug5}$ is 49, the states and parameters can not be estimated for the system defined in (4.16) by using a linear state estimator.

A non-linear observability analysis was performed using the matrix $d\mathcal{O}$ as described in (4.7). The span of $d\mathcal{O}$ was calculated to be 49, which means that the states and parameters that are defined in (4.16) can be estimated using the real-time measurements that were defined in (4.16), using a non-linear estimator such as an MHE. Note that the parameter quantifying the shape of the peak

Table 4.7. Vector dimensions of the flotation model.

Vector	Dimension	Description
$\mathbf{y}_{ck}$	3×1	Measured outputs per flotation cell
$\mathbf{y}_H$	5×1	Additional measured outputs per section
$\mathbf{y}_5$	17×1	Total number of measured outputs for the section
$\mathbf{x}_{ck}$	6×1	States per flotation cell
$\mathbf{x}_H$	3×1	Additional model states per section
$\mathbf{x}_5$	27×1	Total number of model states for the section
$\mathbf{u}_{ck}$	2×1	Manipulated variables per flotation cell
$\mathbf{u}_H$	1×1	Additional manipulated variables for the section
$\mathbf{u}_5$	9×1	Total number of manipulated variables for the section
$\mathbf{x}_{pk}$	4×1	Estimated parameters per flotation cell
$\mathbf{x}_{pH}$	6×1	Additional estimated parameters for the section
$\mathbf{x}_{pH}$	22×1	Total number of estimated parameters for the section
$\mathbf{x}_{aug5}$	49×1	Augmented state vector with all states and estimated parameters

Table 4.8. Results of the state observability analysis for the rougher section.

Variable	
$\mathbf{x}_{aug5}$	dim = 49
$\mathcal{O}$	rank = 42
$d\mathcal{O}$	span = 49
Observable (linear)	No
Observable (non-linear)	Yes

in air recovery ($K_{\alpha_{J_g}}$) was assumed to remain relatively constant and was not included in $\mathbf{x}_{aug5}$ in (4.16).

4.5 CONTROLLABILITY ANALYSIS

The objective of the state controllability analysis is to determine if the model states can be driven towards desired setpoints using the defined model inputs. Similar to the observability analysis performed in Section 4.4, if all the states are not controllable, it means that the states cannot be driven to a specific operating condition given the available inputs. The controllability analysis does not provide any conclusion on the operating ranges of the model inputs relative to the desired model states.

The state controllability of the linear system is analysed to determine if the states $\mathbf{x}_5$, described in (4.16), are controllable using the manipulated variables $\mathbf{u}_5$ in (4.16). The flotation cell level states, L_k, and hopper level state, L_H, are typically controlled to user-defined setpoints when basic stabilisation controllers are implemented, as described by Saffy *et al.* (2019). A grade control strategy, as implemented by Saffy *et al.* (2019), controls the grade in the concentrate hopper G_H to a desired setpoint. The grade can be calculated from the states describing the masses of different minerals in the concentrate hopper ($M_H^{i,j}$), as shown in Table 3.15. Hadler *et al.* (2010a) showed how the maximum recovery for each flotation cell, k, is achieved when the air recovery, α_k, is maximised. It is therefore important that all the states defined in Tables 4.2 and 4.3 are controllable using the model inputs defined in Table 4.9 to ensure that all the control objectives described in this paragraph can be achieved. Note that the state vector $\mathbf{x}_5$ defined in (4.16) is used in the controllability analysis—not the augmented state vector, $\mathbf{x}_{aug5}$, that also includes model parameters, as used in the observability analysis performed in Section 4.4.

Table 4.9. Model inputs.

Symbol	Unit	Description	Equation
J_{gSP_k}	mm/s	Superficial air velocity setpoint for cell k	$J_{g_k} = \frac{Q_{air_k}}{A_k}$
z_k	%	Tailings valve position for cell k	-
Q_H	m^3/h	Flow rate out of the concentrate hopper	-

The dimensions of the sub-matrices of the controllability matrix $\mathcal{C}$ are given in Table 4.10. The state vector $\mathbf{x}_5$ has a length of 27, as shown in Table 4.7. If the state controllability matrix $\mathcal{C}$ as defined in

(4.5) has a rank of 27, all the states defined in $\mathbf{x}_5$ are controllable using the model inputs defined in $\mathbf{u}_5$.

Table 4.10. Results of the state controllability analysis for the rougher section.

Matrix	Rank
$\mathbf{B}$	9
$\mathbf{AB}$	8
$[\mathbf{B}, \mathbf{AB}]$	17
$[\mathbf{B}, \mathbf{AB}, \mathbf{A}^2\mathbf{B}]$	25
$[\mathbf{B}, \mathbf{AB}, \mathbf{A}^2\mathbf{B}, \mathbf{A}^3\mathbf{B}]$	27

From Table 4.10, it can be seen that a full rank of 27 is achieved for the state controllability matrix, $\mathcal{C}$, as defined in (4.5), when the terms $\mathbf{B}$, $\mathbf{AB}$, $\mathbf{A}^2\mathbf{B}$ and $\mathbf{A}^3\mathbf{B}$ are included. This confirms that all 27 states in $\mathbf{x}_5$ can be driven towards desired setpoints using the superficial air velocity (J_{g_k}) and valve positions (z_k) for each flotation cell, k, in combination with the concentrate hopper outflow rate (Q_H).

4.6 DISCUSSION

The ability to estimate model parameters for α_k and D_{BF_k} from online measurements provide valuable information on how close each cell is operating to the maximum air recovery point and in what direction the superficial air velocity, J_{g_k}, and froth depth, h_{f_k}, should be adjusted to maximise the recovery of each cell. By combining the estimated maximum air recovery point with a model for D_{BF_k} (which has a strong influence on entrainment and, hence, grade), differences in operation between flotation cells in a section can be identified and compensated for, and options are available to expand the model described in Chapter 3 to include additional manipulated variables, such as reagent addition, into an optimisation strategy.

One parameter, $K_{\alpha_{J_g}}$, was removed from the parameter vector shown in (4.8) to obtain a state observable and parameter identifiable system shown in (4.13). A constant value thus needs to be specified for $K_{\alpha_{J_g}}$, which will affect the estimated values of $K_{\alpha_{J_{g_k}}}$ and $K_{\alpha_{h_f}}$. While the curvature of the peak in air recovery is expected to be less important than the location of the peak (defined by $K_{\alpha_{J_{g_k}}}$ and $K_{\alpha_{h_f}}$), the sensitivity of the parameter estimation function to an error in $K_{\alpha_{J_g}}$ needs to be considered.

The volume balance and associated observability analysis allow the water recovery from each cell to be calculated. This provides a good indication of the relative contribution of each cell to the total entrained mass. A reduction in the water recovery, Q_{W_k}, to the concentrate stream of a flotation cell, k, generally results in an increase in the concentrate grade. The quadratic relationship between water recovery and D_{BF_k} that is shown in Figure 3.6 highlights the importance of including a real-time measure of froth bubble size as part of an optimisation strategy.

The mass balance and the parameters that can be estimated from the full flotation model provide invaluable information to distinguish between true flotation and entrainment in the concentrate streams from each flotation cell. This is the key to optimising reagent addition. Low concentrate grades can be caused by insufficient suppression of gangue minerals $M_k^{1,0}$, excessive entrainment of gangue minerals or insufficient flotation of the valuable mineral $M_k^{0,0}$, which may in turn require an adjustment of reagents (collectors or activators) or an adjustment to the grind size. The ability to estimate the flotation rate constants of the desired and gangue minerals ($K^{0,0}$ and $K^{1,0}$) from online measurements opens a range of opportunities to optimise reagent additions and respond to short-term variations in ore characteristics that occur between sampling campaigns. An estimate of the relative contribution from each cell to the overall concentrate stream allows for optimisation across multiple cells to achieve optimal operation of a flotation section or, potentially, a flotation plant.

While the observability analysis confirms that valuable process parameters can be estimated from real-time measurements, the controllability analysis confirms that a model-based automatic control strategy can be used to stabilise and optimise the state variables of a flotation process, as defined by the model in Chapter 3. Control variables that are commonly available on industrial flotation plants (J_{gSP_k}, z_k and Q_H) are sufficient to control the concentrate grade and air recovery, α_k, while stabilising the concentrate hopper level, L_H, and flotation cell levels, L_k. The ability to control α_k in each cell implies that each cell can be controlled at its peak air recovery, α_k, at all times, using a model-based controller instead of relying on an iterative stepping algorithm.

The objective of a flotation plant is to maximise the production of a product of a desired grade. By controlling the overall concentrate grade to a desired setpoint while each flotation cell is operated at the maximum air recovery (α_k) (which is associated with maximum mineral recovery (Hadler *et al.*, 2012)), an important step towards optimising flotation operation is achieved.

4.7 CONCLUSION

A flotation model was described in Chapter 3 to model the key flotation variables that were identified in Chapter 2. Only variables that are commonly manipulated on industrial flotation circuits (see Table 4.9) were defined as manipulated variables for use in the controllability analysis, and only measurements that are commonly available on industrial flotation circuits were used in the observability analysis for state and parameter estimation. The observability analysis in Section 4.4 indicates that all the model parameters defined in Table 4.1, except for $K_{\alpha_{Jg}}$, can be estimated using online measurements—including floatability constants of desired and gangue minerals that are normally calculated as part of lab analyses, based on spot or averaged samples. The controllability analysis confirms that all the modelled states defined in Tables 4.2 and 4.3 can be driven towards desired values using manipulated variables that are commonly available on industrial flotation circuits. This implies that a model-based control strategy based on the model states defined in Tables 4.2 and 4.3 can be used to optimise flotation operation by taking interactions between states and non-linear relationships into account to ensure that each state is driven towards an operating condition that would maximise performance of the flotation section.

The combination of fundamental dynamic mass and volume balances, steady-state flotation froth models and empirical relations for air recovery and froth bubble size, allows key characteristics of flotation processes to be estimated from real-time measurements, supporting the first hypothesis in Section 1.5. This opens up opportunities to control the flotation process more efficiently, optimise the flotation process across multiple flotation cells and expand the model in future to include additional variables such as reagent additions.

CHAPTER 5 CONTROLLER DESIGN

5.1 CHAPTER OVERVIEW

It was shown in Chapter 4 that the states of the froth flotation model described in Chapter 3 are observable and the parameters are identifiable. This implies that the unmeasured process states, such as the mineral masses in each flotation cell $M_k^{i,j}$ and in the concentrate hopper $M_H^{i,j}$, can be estimated. In addition, the model parameters that are used in the model to distinguish between mineral recovery due to true flotation compared to recovery due to entrainment (e.g., the floatability constants $K^{0,0}$ and $K^{1,0}$, and C_{PB}) can be estimated from real-time measurements that are commonly available on industrial flotation plants. The ability to estimate model states and parameters from real-time measurements is a key aspect of the model structure described in Chapter 3, as changes in process parameters could be detected in real-time and be used in a model-based control strategy, rather than depending on infrequent manual sampling results to update model parameters.

The design of an automatic controller implementation based on the model described in Chapter 3 has two components: the design of a state and parameter estimator and the design of the model-based control strategy. In this chapter a simulation study is presented that uses the flotation model described in Chapter 3 in a non-linear model predictive controller implementation. The simulation framework that includes the MPC and an MHE is first described in Section 5.2. In Section 5.3, the design of the MHE is described, followed by simulation results showing the performance of the MHE. In Section 5.4, the design of an MPC is described, with the objective of maximising recovery while maintaining a target concentrate grade. In Section 5.5, the simulation results of three simulation studies are shown. The first simulation study in Section 5.5.1 shows how an increase in the air recovery that a bank of flotation cells is operated at relates to a series of grade-recovery curves of increasing recovery. The second simulation study in Section 5.5.2 demonstrates the MPC's performance in rejecting typical disturbances and variability in model parameters on a flotation circuit. The third

simulation study in Section 5.5.3 compares the performance of the MPC to a conventional proportional integral derivative (PID) control strategy that does not explicitly take process non-linearities into account. Results are discussed in Section 5.6 and concluding remarks are given in Section 5.7.

5.2 SIMULATION FRAMEWORK

A modular scheme for a non-linear MPC controller implementation is described by Lucia, Tătulea-Codrean, Schoppmeyer and Engell (2017), which includes function blocks for a model, an optimiser, an observer and a simulator. A Python library (*do-mpc*) provides an environment to implement the function blocks and data exchange mechanisms between function blocks and data visualisation interfaces. The *do-mpc* Python library was used in the simulation studies shown in Section 5.5 to implement the controller and simulator for the flotation circuit and to estimate unmeasured states and model parameters using an MHE.

The model framework is shown in Figure 5.1, including vectors for measured and unmeasured disturbances, measured outputs, states, parameters, setpoints and control actions specific to the model described in Chapter 3.

5.2.1 Flotation simulator

The flotation plant block shown in Figure 5.1 simulates the dynamic flotation model described in Chapter 3. Initial conditions and model parameters were chosen based on data that were collected from an industrial flotation circuit as described by Hadler *et al.* (2010b) to ensure that simulation results are representative of typical operation on an industrial flotation circuit. Random noise with a uniform distribution was added to the measured model outputs. Details of the noise levels that were simulated are provided for each simulation study. Some of the model parameters in the flotation simulator were varied in Section 5.5.2 to simulate the effect of unmeasured disturbances.

5.2.2 Moving horizon estimator

An extended Kalman Filter or MHE is often used to perform state and parameter estimation (Lucia *et al.*, 2017). For this simulation study, the MHE that was available in the *do-mpc* Python library was used for state and parameter estimation, as the observability analysis that was described in Chapter 4 indicated that a non-linear observer was required to estimate the states and parameters. A comparison of different state and parameter estimation techniques is outside the scope of this work, but additional

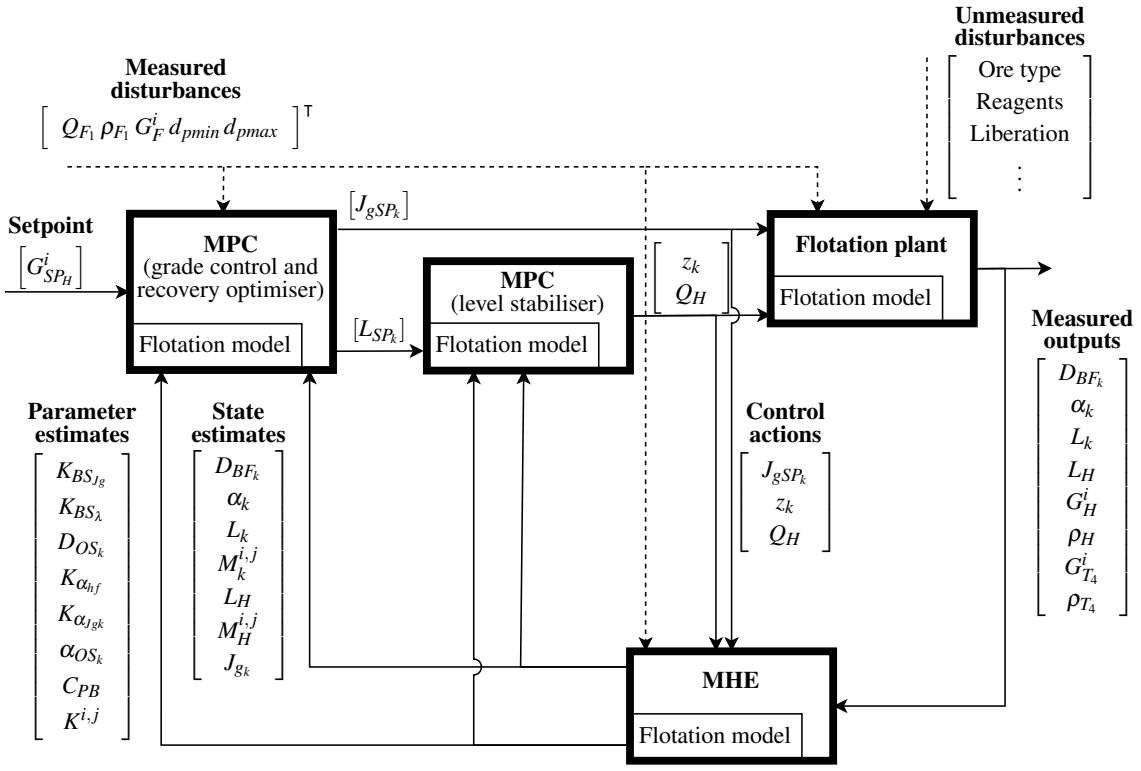

Figure 5.1. Block diagram of MPC controller implementation.

advantages of an MHE (e.g., the ability to include constraints on model states) and disadvantages (e.g., computational cost) are described by Haseltine and Rawlings (2005). The MHE design is described in detail in Section 5.3.

5.2.3 Model predictive controller

The non-linear MPC implementation that is shown in Figure 5.1 was separated into two controllers:

- A slave MPC (level stabiliser) to stabilise the flotation cell levels, L_k, and the concentrate hopper level, L_H.
- A master MPC (grade control and recovery optimiser) to calculate the optimal combinations of level setpoints, L_{SP_k}, and aeration rate setpoints, J_{gSP_k}, for each flotation cell to achieve a target concentrate grade while maximising recovery.

This is consistent with the approach that is commonly employed in industrial flotation control and optimisation applications. Model-based stabilisation controllers such as the FloatStar Level Stabiliser that is described by Schubert *et al.* (1995) are common in industry, while grade and

recovery optimisation is commonly implemented as a higher-level master (grade control and recovery optimisation) controller that provide setpoints to a slave (stabilisation) controller, as described by Saffy *et al.* (2019). The option exists to integrate the stabilisation and optimisations controllers into a single MPC controller. For this study, the functionality of level stabilisation and grade control and recovery optimisation was separated to allow the same stabilisation controller to be used in a comparison of different grade control strategies in Section 5.5.3, thereby removing any bias as a result of using different stabilisation controllers.

5.2.3.1 Level stabilisation strategy

Figure 5.2 shows the implementation of the stabilisation controllers. Circles indicate instrumentation, solid arrows indicate process flows and dashed lines indicate signals that form part of the controller implementation. The slave MPC (level stabiliser) stabilises the flotation cell levels, L_k, at desired level setpoints, L_{SP_k}, by manipulating the tailings flow control valves, z_k. Stabilisation of the concentrate hopper level, L_H, at a desired setpoint, L_{SP_H}, by manipulating the concentrate flow rate, Q_H, also forms part of the stabilisation controller. PID controllers are used to manipulate the air flow rate, Q_{Air_k} into each flotation cell, k, to control the superficial gas velocity, J_{g_k} to a desired setpoint, J_{gSP_k}.

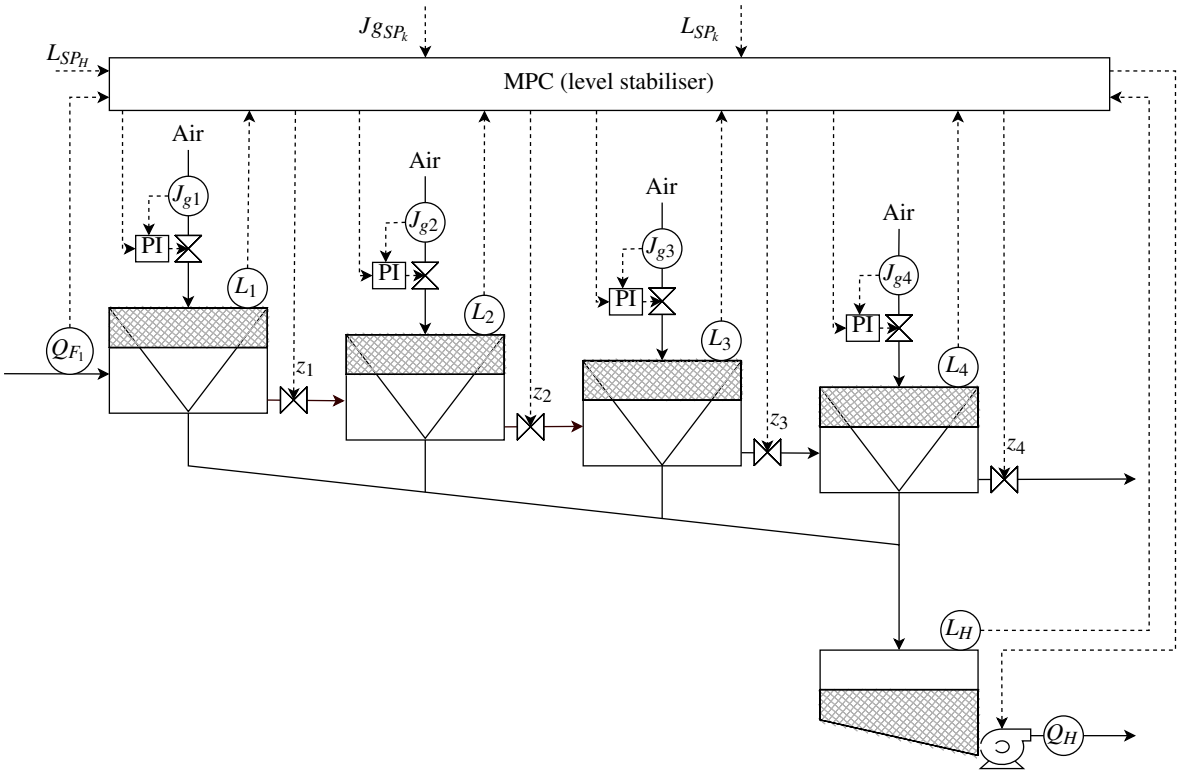

Figure 5.2. Level and air stabilisation implementation.

5.2.3.2 Grade control and optimisation strategy

Figure 5.3 shows the implementation of the master (grade control and recovery optimisation) strategy. ρ_F and ρ_H are the feed and concentrate densities that are equivalent to C_{wF} and C_{wT}. Q_{F_1} and Q_H are the feed and concentrate volumetric flow rates, and G_F and G_H are the feed and concentrate grades.

The grade control strategy does not explicitly specify a concentrate mass flow rate setpoint. Variations in pulp level setpoints and aeration rate setpoints for the flotation cells would affect concentrate mass flow, which would result in a change in hopper level, L_H, and/or ρ_H. The concentrate hopper level controller will respond to a change in L_H by adjusting the pump speed, which will result in a change in the measured volumetric flow rate, Q_H from the hopper.

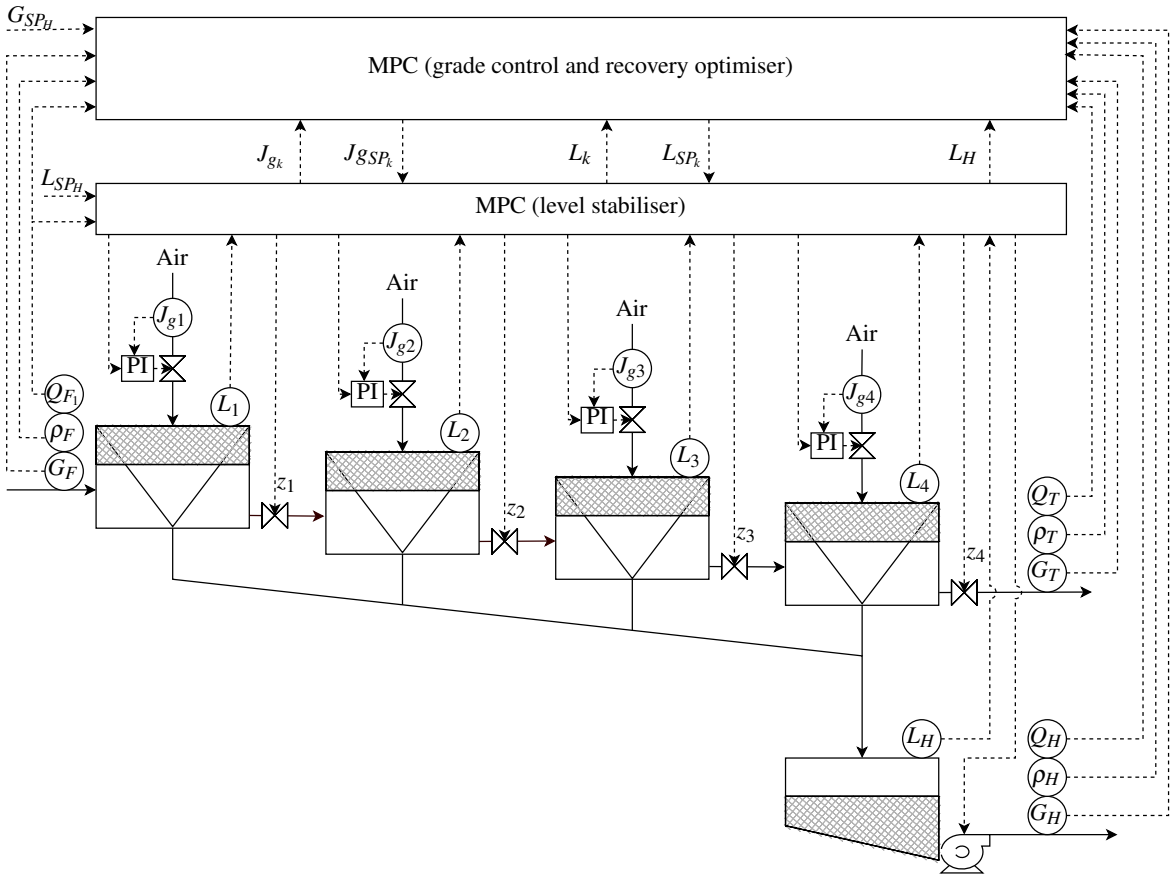

Figure 5.3. Grade control and optimisation implementation.

5.3 MOVING HORIZON ESTIMATOR DESIGN

The MHE implementation uses a system with the form

$$\begin{aligned} \dot{\mathbf{x}}(t) &= f(\mathbf{x}(t),\mathbf{u}(t),\mathbf{p}(t)) + \mathbf{w}(t), \\ \mathbf{y}(t) &= g(\mathbf{x}(t),\mathbf{u}(t),\mathbf{p}(t)) + \mathbf{v}(t), \end{aligned} \tag{5.1}$$

with the variables defined in Table 5.1. The measurement noise, $\mathbf{v}(t)$, quantifies the error between the measured output, $\mathbf{y}(t)$ and the modelled output, $g(\mathbf{x}(t),\mathbf{u}(t),\mathbf{p}(t))$. The MHE objective function for a discretised system is given by Rao and Rawlings (2002) as

$$\begin{aligned} \min_{\substack{\mathbf{x}_0,\mathbf{p},\\ \{\mathbf{w}_k\}_{k=0}^{N-1}}} \quad & \|\mathbf{x}_0-\tilde{\mathbf{x}}_0\|^2_{P_x} + \|\mathbf{p}-\tilde{\mathbf{p}}\|^2_{P_p} + \sum_{k=0}^{N-1}\left(\|\mathbf{v}_k\|^2_{P_v} + \|\mathbf{w}_k\|^2_{P_w}\right), \\ \text{subject to} \quad & \left.\begin{aligned} \mathbf{x}_{k+1} &= f_k(\mathbf{x}_k,\mathbf{u}_k,\mathbf{p},k) + \mathbf{w}_k, \\ \mathbf{y}_k &= g_k(\mathbf{x}_k,\mathbf{u}_k,\mathbf{p},k) + \mathbf{v}_k, \\ h_k(\mathbf{x}_k,\mathbf{u}_k,\mathbf{p}) &\le 0 \end{aligned}\right\} k=0,\ldots,N \end{aligned} \tag{5.2}$$

with the variables defined in Table 5.2.

Table 5.1. Parameters used in the system equations.

Variable	Description
$\mathbf{x}$	State vector
$\mathbf{u}$	Input vector
$\mathbf{y}$	Measured output vector
$\mathbf{p}$	Estimated parameter vector
$\mathbf{w}$	Process noise vector
$\mathbf{v}$	Measurement noise vector

Each weighting matrix (P_x, P_p, P_v and P_w) is defined as a diagonal matrix, with the entries on the diagonal determining the penalties applied to variations in the corresponding state (for P_x and P_w), output (P_v) or parameter (P_p) in (5.2). Since process noise, $\mathbf{w}_k$, was not included in the models described in Chapter 3, P_w was not defined for this study.

Table 5.2. Parameters used in the MHE objective function.

Variable	Description
N	MHE horizon
k	Iterator for MHE objective function
$\tilde{\mathbf{x}}_0$	Previous estimate of $\mathbf{x}_0$
$\tilde{\mathbf{p}}$	Previous estimate of $\mathbf{p}$
P_x	Weighting matrix on $\mathbf{x}_0$
P_p	Weighting matrix on $\mathbf{p}$
P_v	Weighting matrix on $\mathbf{v}$
P_w	Weighting matrix on $\mathbf{w}$
$\mathbf{v}_k$	Measurement noise
$f_k(\ldots)$	Non-linear state-space function
$g_k(\ldots)$	Non-linear output function
$h_k(\ldots)$	Model constraints (state, parameter and output)

Typical operating ranges for the model states ($\mathbf{x}$), inputs ($\mathbf{u}$) and parameters ($\mathbf{p}$) are shown in Table 5.3, and were used to normalise the diagonal elements of the weighting matrices, P_x, P_p and P_v. In addition, the normalised diagonal elements in P_x, P_p and P_v were multiplied by weighting factors to obtain the desired response. Where measurement noise was added to the simulated process outputs, the noise was calculated as a percentage of the *operating range* values in Table 5.3. The final values of the weighting matrices P_x, P_p and P_v (excluding normalisation) are shown in Table 5.3.

Simulation results of the MHE estimating model parameters are shown in Figures 5.4 - 5.9 for scenarios with no noise and with uniformly distributed measurement noise of 1%, 3% and 5% of the variable ranges added to the model outputs. The model parameters in Table 5.4 were increased linearly to a maximum of 5% above their default values and then decreased again to their default values. $K^{1,0}$ was increased over a larger range to 20% above its original value, as the noise levels that were simulated masked the relatively small quantities of gangue minerals that report to the concentrate stream through the mechanism of true flotation. A 5% step change was made to the output offset parameters, α_{OS_k} and D_{OS_k}, to simulate an unmeasured disturbance in reagent addition.

Table 5.3. MHE parameter ranges and weights.

Variable	Notes	Operating range (max-min)	P_x	P_v	P_p
States					
D_{BF_k}	mm	2.0	1×10^{-1}	1×10^{1}	
α_k		0.05	1×10^{1}	1×10^{1}	
L_k	m	0.1	1×10^{2}	1×10^{2}	
$M_k^{0,0}$	Chalcopyrite	50.0	1×10^{-1}		
$M_k^{1,0}$	Gangue	10000	1×10^{-1}		
J_{g_k}	mm/s	1.0	5×10^{1}		
L_H	m	0.1	1×10^{2}	1×10^{0}	
$M_H^{0,0}$	Chalcopyrite	500	1×10^{2}		
$M_H^{1,0}$	Gangue	100	1×10^{2}		
Parameters					
$K_{BF_{Jg}}$	s	0.529			1×10^{2}
K_{BF_λ}	mm/s	0.313			1×10^{1}
D_{OS_k}	mm	10.0			1×10^{1}
$K_{\alpha_{J_{gk}}}$	mm/s	7.20			1×10^{-2}
$K_{\alpha_{h_f}}$	1/s	0.01			1×10^{3}
α_{OS_k}		0.1			1×10^{2}
C_{PB}		50.0			1×10^{-2}
$K^{0,0}$	Chalcopyrite	2.3			1×10^{-1}
$K^{1,0}$	Gangue	2.1×10^{-4}			1×10^{0}
Outputs					
G_H		0.005		1×10^{0}	
G_T		0.0005		1×10^{0}	
C_{wH}		2.0		1×10^{0}	
C_{wT}		0.1		1×10^{-1}	

Table 5.4. Model parameters to be estimated.

Symbol	Unit	Description
$K_{BF_{J_g}}$	s	Effect of the superficial gas velocity on the mean top-of-froth bubble diameter
K_{BF_λ}	mm/s	Effect of the average froth residence time on the mean top-of-froth bubble diameter
$K_{\alpha_{J_{g_k}}}$	mm/s	Value of the superficial air velocity in cell k where air recovery is maximised when $h_{f_k} = 0$
$K_{\alpha_{h_f}}$	1/s	Effect of a change in h_{f_k} on the superficial air velocity where air recovery is maximised
α_{OS_k}	-	Offset included in steady-state air recovery equation, α_{SSk} in cell k
D_{OS_k}	mm	Offset included in the steady-state top-of-froth bubble diameter equation, D_{BFSS_k} in cell k
C_{v_k}	$m^{5/2}/h$	Valve constant for cell k
C_{PB}	-	Plateau border drag coefficient
$K^{i,j}$	-	Flotation rate-constant for species i, class j

The sampling interval was chosen based on the shortest process time constant and the prediction horizon was chosen based on the time to steady-state. The same sampling interval and prediction horizon were used for the MHE and MPCs described in Section 5.4. In terms of the choice of the sampling interval, the shortest time constant in the model relates to the average froth residence time, λ_{air_k}. At a froth depth $h_{f_k} = 120$ mm and superficial gas velocity $J_{g_k} = 7.5$ mm/s, the average froth residence time is approximately 16 s. In terms of the choice of the prediction horizon, the residence time of a flotation cell for the operating conditions reported in Hadler *et al.* (2010a) is approximately 60 s, and four cells are connected in series for the rougher bank. Therefore, to include the fastest system dynamics in the froth, but also allow the prediction horizon of the MPC controller to capture most of the steady-state response for the mass transfer between cells, the sampling interval was chosen as 10 s and the prediction horizon P as 30 samples (300 s).

Oosthuizen *et al.* (2021) showed two sets of simulation results: the first set assuming that grade and flow measurements are available on the tailings stream and the second set using a steady-state

approximation to estimate *measurements* on the tailings stream. The main difference between the model used in the simulations by Oosthuizen *et al.* (2021) compared to the model that was used in the simulation results shown in this chapter is that Oosthuizen *et al.* (2021) assumed that the peaks in air recovery would occur at the same values of J_{g_k} for all the flotation cells, k, while the model that was used in this chapter allows for the peaks in air recovery to occur at different values of J_{g_k} for each flotation cell, k, as was observed on industrial trials (Hadler and Cilliers, 2009; Smith *et al.*, 2010).

A comparison of scenarios with and without grade (G_{T_4}) and density (C_{wT}) measurements on the final tailings stream, similar to what was described by Oosthuizen *et al.* (2021), is repeated in this chapter. For the scenario where a grade measurement is not available on the final tailings stream, Figures 5.4 - 5.6 compare the model described in Chapter 3 to a model that does not have a measurement of grade available on the final tailings stream, G_{T_4}, but uses a steady-state approximation based on the feed grade, G_F, and concentrate grade, G_H, instead. For this study, the benefit of the additional instrumentation on the tailings stream is not significant. However, it is clear that with the more conservative configuration of the MHE for the model using a steady-state approximation on tailings flow and grade, the parameter $K^{0,0}$ is slower to respond to changes. Factors such as the residence time of the concentrate hopper and fast varying process disturbances could potentially reduce the accuracy of the steady-state estimate, but for the set of disturbances considered and their rates of change, the model and set of measurements shown in Chapter 3—both with and without measurements on the tailings stream—provide a viable solution using instrumentation that is commonly available on industrial sites.

Figures 5.7 - 5.9 show the effect of noise on the accuracy with which the parameters are estimated, using the models described in Chapter 3. Noise on the parameter estimates can be reduced further by increasing the MHE horizon, but the delay in response will increase as the MHE horizon is increased. The MHE performed well under all noise levels considered, tracking 5% variations in model parameters reasonably well, even with 5% measurement noise.

An interesting observation is that the estimate of $K_{\alpha_{hf}}$ in Figure 5.8 becomes less accurate at higher noise levels, while undesired offsets in the estimates of K_{BFJg}, $K_{BF\lambda}$ and D_{OS_k} in Figure 5.9 reduce as noise levels increase. As the identifiability of K_{BFJg} is dependent on variability in J_{g_k}, higher noise levels potentially increase the variability in J_{g_k}, thereby improving the estimation accuracy of K_{BFJg} (which also affects the estimates of $K_{BF\lambda}$ and D_{OS_k}). It is concerning that an offset in estimated

parameters (K_{BFJg}, $K_{BF\lambda}$ and D_{OS_k}) could develop under certain conditions, and a careful design of the MHE would be required to ensure that these parameters are only estimated under suitable conditions.

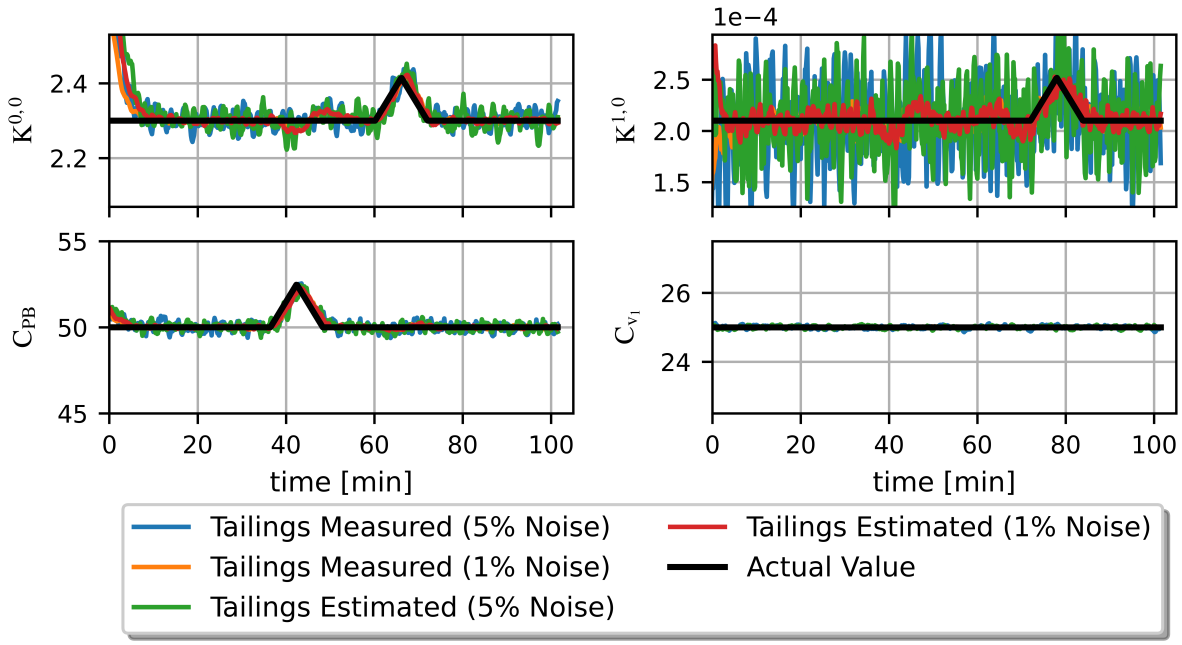

Figure 5.4. Model parameter estimation—comparing responses of models with and without grade and density measurements on Q_{T_4}.

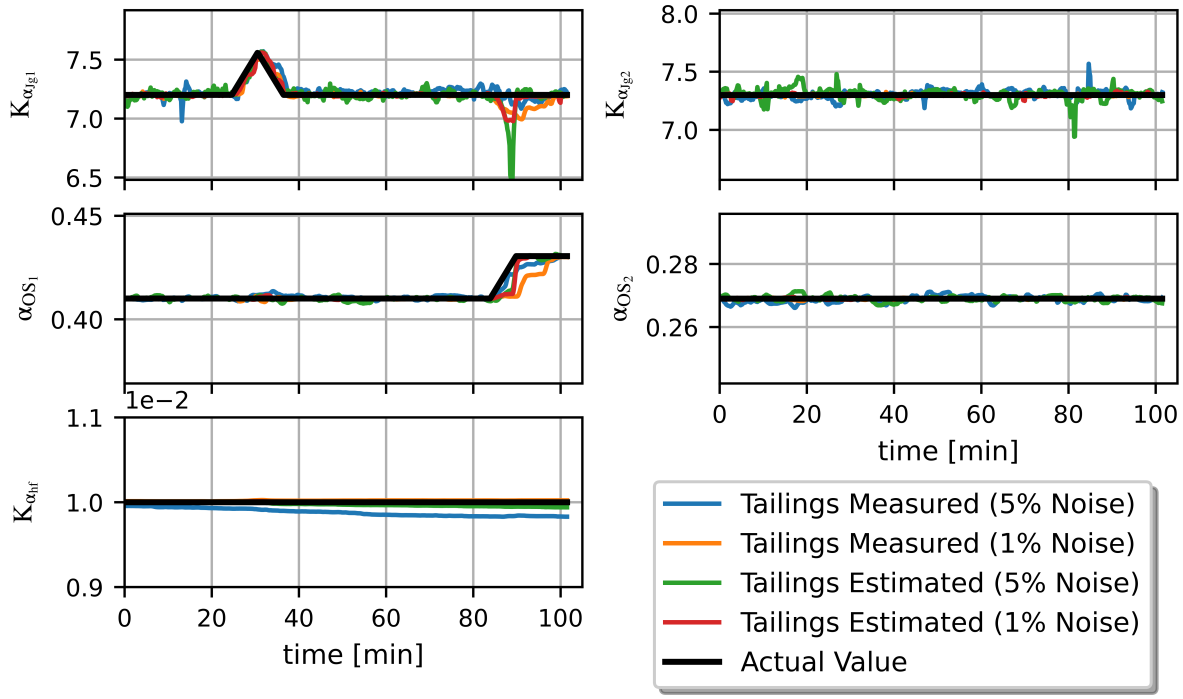

Figure 5.5. Model parameter estimation related to α_k—comparing responses of models with and without grade and density measurements on Q_{T_4}.

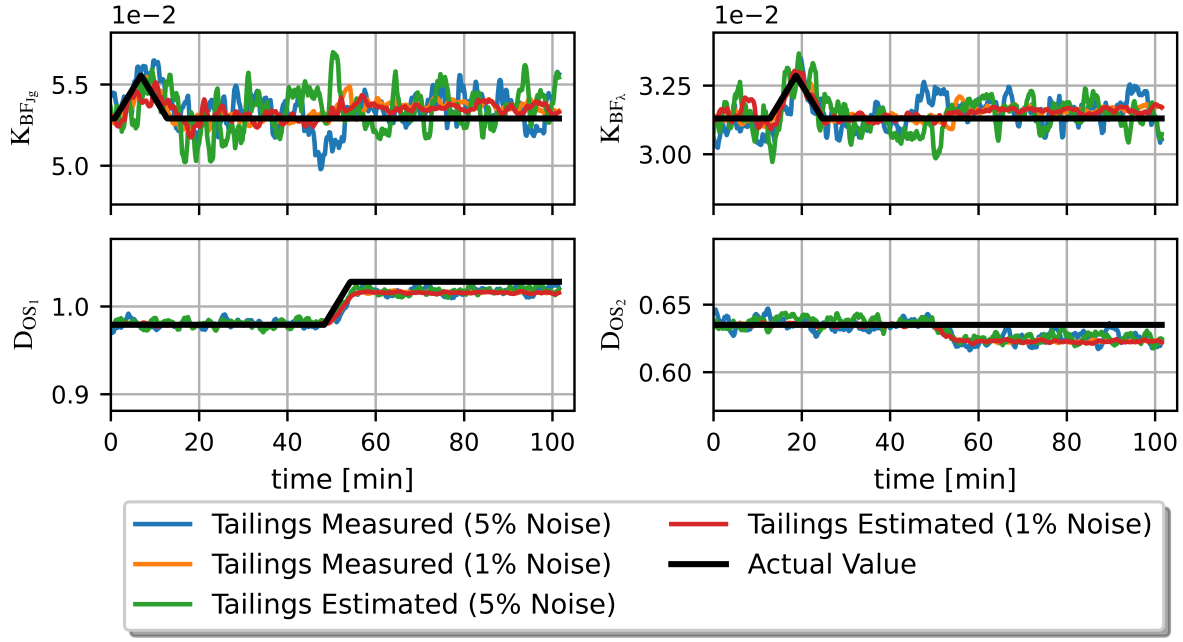

Figure 5.6. Model parameter estimation related to D_{BF_k}—comparing responses of models with and without grade and density measurements on Q_{T_4}.

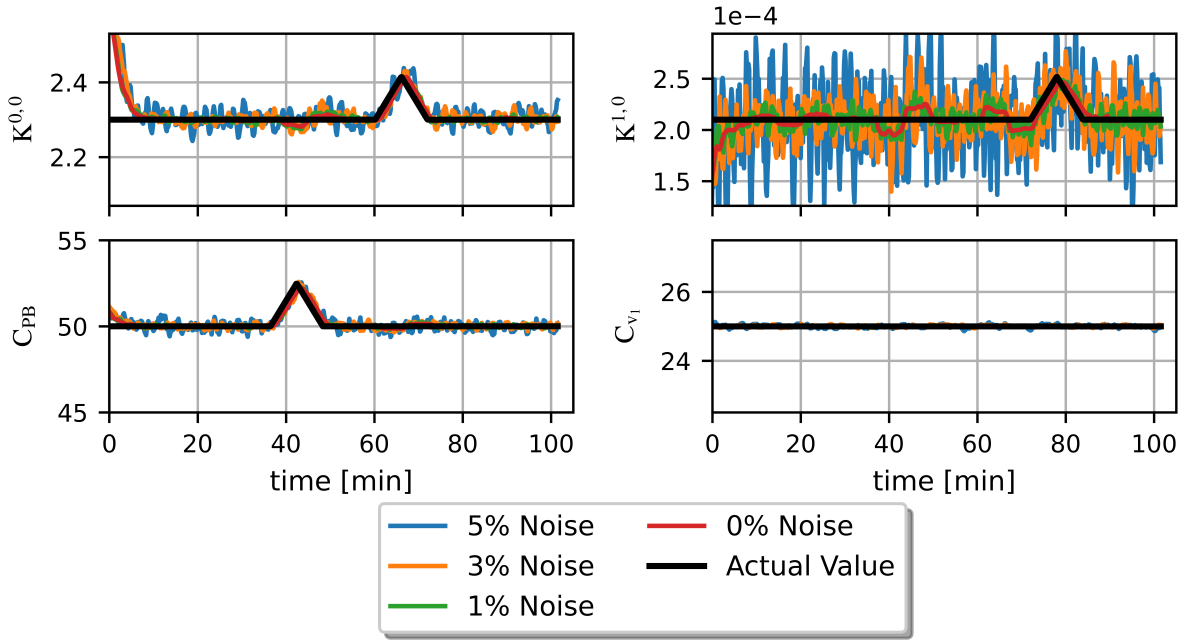

Figure 5.7. Model parameter estimation—performance with different noise levels.

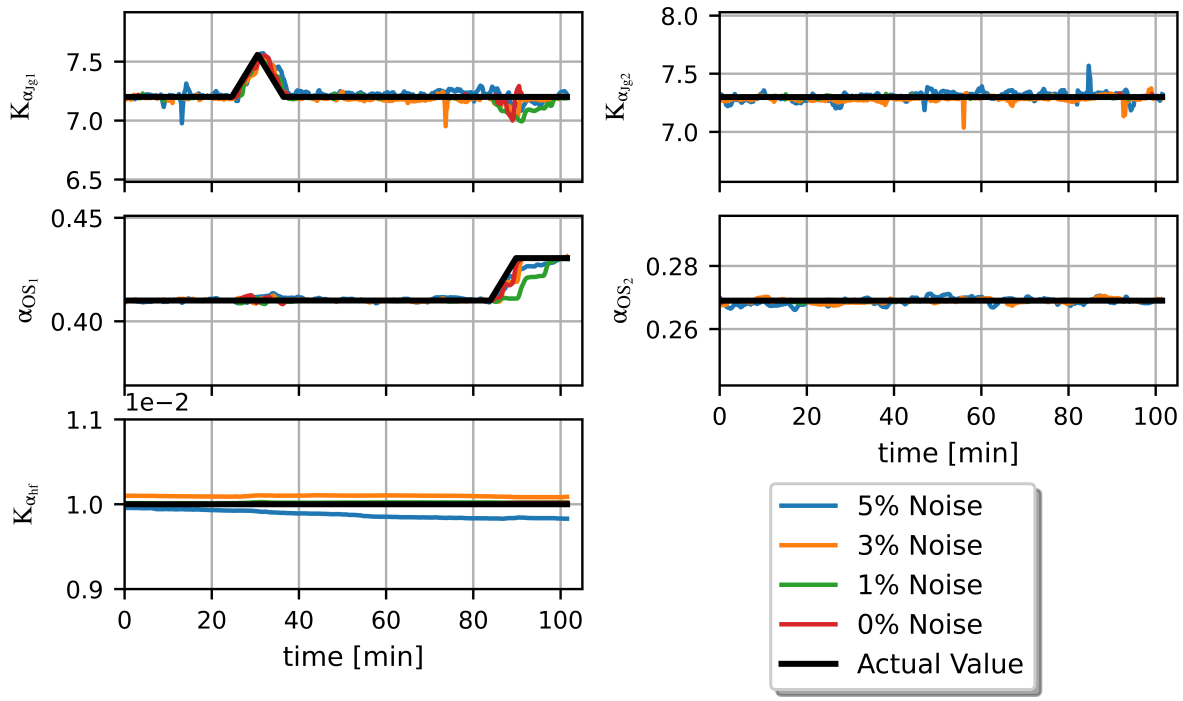

Figure 5.8. Model parameter estimation related to α_k—performance with different noise levels.

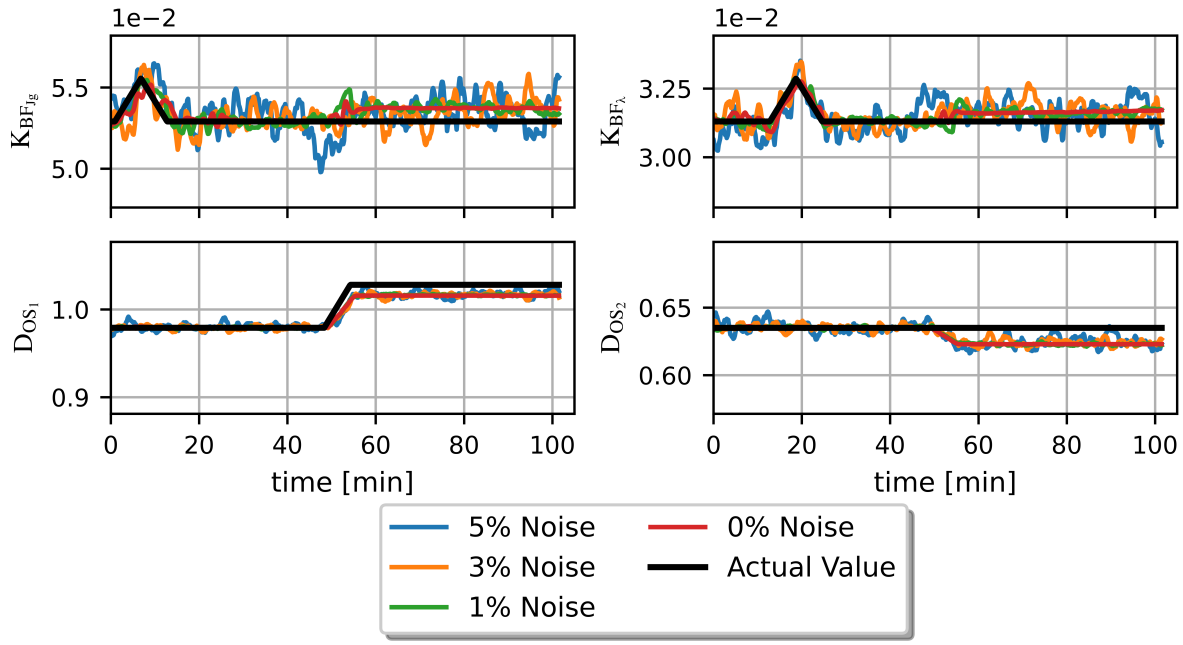

Figure 5.9. Model parameter estimation related to D_{BF_k}—performance with different noise levels.

5.4 CONTROLLER DESIGN

Two MPCs were designed as depicted in Figure 5.1. These two controllers are connected in a master-slave configuration:

1. The slave MPC is the stabilisation controller depicted in Fig. 5.2 and discussed in Section 5.2.3.1.
2. The master MPC is the grade controller and recovery optimiser depicted in Fig. 5.3 and discussed in Section 5.2.3.2.

The stabilisation controller (slave MPC) has the objective to maintain all flotation cell levels, L_k, and hopper level, L_H, at setpoints by manipulating tailings flow rates of the flotation cells by adjusting tailings valves z_k and the hopper flow rate, Q_H. The master MPC (grade control and recovery optimiser) calculates the flotation cell level setpoints (L_{SP_k}) and superficial gas velocity setpoints (J_{gSP_k}) which are sent as inputs to the slave MPC controller.

Simplified models of L_k and L_H were defined for the master controller:

$$\begin{aligned} \frac{d}{dt}L_k &= \frac{L_{SP_k} - L_k}{\tau_L} \\ \frac{d}{dt}L_H &= \frac{L_{SP_H} - L_H}{\tau_L}, \end{aligned} \tag{5.3}$$

where τ_L is an estimated time constant of the stabilisation controller and L_{SP_H} is a user-defined setpoint for the concentrate hopper level.

The grade controller and recovery optimiser (master MPC) have the following objectives:

- control the grade in the hopper (G_H) to a desired setpoint by manipulating the aeration rates (J_{SPg_k}) and froth depths (h_{f_k}) for each cell by adjusting the flotation cell level setpoints (L_{SP_k})
- maximise circuit recovery (R_C).

The MPC minimises a dynamic objective function of the following form (Qin and Badgwell, 2003):

$$J(\mathbf{u}^M) = \sum_{j=1}^{P} \left\{ \|\mathbf{e}^y_{k+j}\|^q_{\mathbf{Q}_j} + \|\mathbf{s}_j\|^q_{\mathbf{T}} \right\} + \sum_{j=0}^{M-1} \left\{ \|\mathbf{e}^u_{k+j}\|^q_{\mathbf{R}_j} + \|\Delta\mathbf{u}_{k+j}\|^q_{\mathbf{S}_j} \right\} \tag{5.4}$$

subject to a model constraints:

$$\begin{aligned} \mathbf{x}_{k+j} &= f(\mathbf{x}_{k+j-1}, \mathbf{u}_{k+j-1}) \quad \forall j = 1, P, \\ \mathbf{y}_{k+j} &= g(\mathbf{x}_{k+j}, \mathbf{u}_{k+j}) \quad \forall j = 1, P \end{aligned} \tag{5.5}$$

and subject to inequality constraints:

$$\begin{aligned} \underline{\mathbf{y}} - \mathbf{s}_j \leq \mathbf{y}_{k+j} &\leq \overline{\mathbf{y}} + \mathbf{s}_j \quad \forall j = 1, P, \\ \mathbf{s}_j &\geq 0 \quad \forall j = 1, P, \\ \underline{\mathbf{u}} \leq \mathbf{u}_{k+j} &\leq \overline{\mathbf{u}} \quad \forall j = 1, M-1, \\ \Delta\underline{\mathbf{u}} \leq \Delta\mathbf{u}_{k+j} &\leq \Delta\overline{\mathbf{u}} \quad \forall j = 1, M-1. \end{aligned} \tag{5.6}$$

Deviations from the desired output trajectory, $\mathbf{y}^r_{k+j}$, are penalised in (5.4) through the error term, $\mathbf{e}^y_{k+j}$, defined as

$$\mathbf{e}^y_{k+j} \equiv \mathbf{y}^r_{k+j} - \mathbf{y}_{k+j}\,. \tag{5.7}$$

Similarly, deviations from a desired steady-state input vector, $\mathbf{u}_s$, are penalised in (5.4) through the error term, $\mathbf{e}^u_{k+j}$, defined as

$$\mathbf{e}^u_{k+j} \equiv \mathbf{u}_{k+j} - \mathbf{u}_s\,. \tag{5.8}$$

Other variables used in (5.4) - (5.6) are defined in Table 5.5.

The default MPC objective function in the *do-mpc* library (Lucia *et al.*, 2017) uses a simplified version of (5.4) with $M = P$ and $\mathbf{R}_j = \mathbf{0}$. $\mathbf{Q}_j$, $\mathbf{R}_j$, $\mathbf{S}_j$ and $\mathbf{T}$ were defined as positive semi-definite weighting matrices to set the relative importances of the four components in the MPC objective function shown in (5.4).

Table 5.5. Parameters used in the MPC objective function.

Variable	Description
P	Prediction horison
M	Control horison
q	q=1 for an L_1 vector norm and q=2 for an L_2 vector norm
$\mathbf{s}_j$	Output constraint slack variables
$\Delta\mathbf{u}_{k+j}$	Change in input values, $\mathbf{u}$, over the control horison, M
$\mathbf{Q}_j$, $\mathbf{R}_j$, $\mathbf{S}_j$ and $\mathbf{T}$	Weighting matrices to set relative importances of components in $J(\mathbf{u}^M)$
$\underline{\mathbf{y}}$ and $\overline{\mathbf{y}}$	Minimum and maximum limits for $\mathbf{y}$
$\underline{\mathbf{u}}$ and $\overline{\mathbf{u}}$	Minimum and maximum limits for $\mathbf{u}$
$\Delta\underline{\mathbf{u}}$ and $\Delta\overline{\mathbf{u}}$	Minimum and maximum limits for $\Delta\mathbf{u}$

For the slave MPC (stabilisation controller) in Figure 5.1, $\|\mathbf{e}^y_{k+j}\|^q_{\mathbf{Q}_j}$ in (5.4) is given by

$$\|\mathbf{e}^y_{k+j}\|^q_{\mathbf{Q}_j} = \sum_{k=0}^{4} (L_{SP_k} - L_k)^2 + (L_{SP_H} - L_H)^2 \,, \tag{5.9}$$

where L_{SP_k} [m] is the pulp level setpoint for each flotation cell k, and L_{SP_H} [m] is the concentrate hopper level setpoint. $\|\mathbf{e}^y_{k+j}\|^q_{\mathbf{Q}_j}$ in (5.9) is minimised by manipulating z_k and Q_H.

For the master MPC (grade control and recovery optimisation) in Figure 5.1, $\|\mathbf{e}^y_{k+j}\|^q_{\mathbf{Q}_j}$ is given by

$$\|\mathbf{e}^y_{k+j}\|^q_{\mathbf{Q}_j} = 100 \times (SP_{G_C} - G_H)^2 - 0.01 \times (1.0 - R_C) \,, \tag{5.10}$$

where SP_{G_C} is the concentrate grade target, and R_C is the *instantaneous* recovery of the flotation section that is modelled. $\|\mathbf{e}^y_{k+j}\|^q_{\mathbf{Q}_j}$ in (5.10) is minimised by manipulating L_{SP_k} and J_{gSP_k}. R_C is calculated as the ratio of the desired element mass flow rate in the concentrate stream relative to the desired element mass flow rate in the feed stream $\dot{M}_{DF}$ (Oosthuizen *et al.*, 2021). Note, an L_1 vector norm was used to maximise R_C in (5.10) to reduce the impact of R_C at lower values on the setpoint-following performance of G_H.

Default values of the diagonal elements of the $\mathbf{S}_j$-term that is used in (5.4) are shown in Table 5.6. The relative scaling between the weightings on the control actions (see Table 5.6) and the controlled

variables in (5.9) and (5.10) were determined experimentally for each experiment to obtain the desired response.

Table 5.6. Default weightings on control actions (diagonal elements of $\mathbf{S}_j$ in (5.4)).

Variable	Weight
J_{gSP_k}	0.1
L_{SP_k}	0.01
z_k	0.01
Q_H	0.01

5.5 SIMULATION STUDY

5.5.1 Simulation Study 1: The link between air recovery and mineral recovery

The experimental trials conducted by Hadler *et al.* (2010a), Smith *et al.* (2010) and Phillpotts *et al.* (2021) indicated that the recovery of a flotation sections increased when α_k is maximised. This implies that operation at higher air recoveries when all other operating conditions remain constant should result in grade recovery curves of higher metallurgical efficiency. The grade setpoint for the concentrate hopper was configured to increase linearly from 0.26 to 0.31. A range of target values was specified for the air recoveries (α_k). Three different scenarios were investigated:

- Scenario 1: Control α_k to a set of target values and manipulate both J_{gSP_k} and L_{SP_k}
- Scenario 2: Control α_k above a set of target values and manipulate both J_{gSP_k} and L_{SP_k}
- Scenario 3: Control α_k to a set of target values and manipulate only J_{gSP_k}

5.5.1.1 Scenario 1: Control α_k to a set of target values and manipulate both J_{gSP_k} and L_{SP_k}

The master and slave MPCs (stabilisation and optimisation) designed in Section 5.4 were used to simulate the response of a control system. The objective function of the master MPC (grade control and recovery optimiser) was modified to control α_k explicitly (instead of maximising recovery as in (5.10)), as

$$\|\mathbf{e}^{y}_{k+j}\|^{q}_{\mathbf{Q}_j} = 10 \times (G_{SP_H} - G_H)^2 + 10 \times \sum_{k=0}^{4} (\alpha_{SP_k} - \alpha_k)^2 \,, \tag{5.11}$$

where α_{SP_k} is a target air recovery defined as a fraction of the maximum α_k for each cell, k.

Figure 5.10 shows the resulting grade-recovery curves when the ranges of J_{gSP_k} and L_{SP_k} are not constrained. From these curves, it is clear how higher air recoveries correspond with grade-recovery curves of increased efficiency (higher recovery at the same grade). These graphs also indicate that high recoveries can be maintained over a range of grades by manipulating both J_{g_k} and L_{SP_k}.

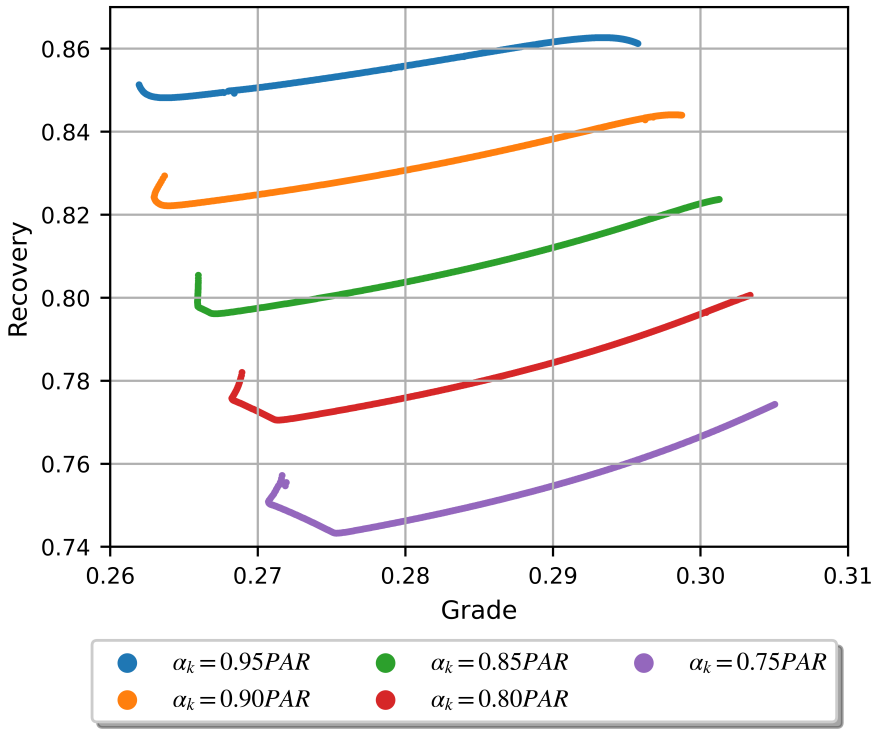

Figure 5.10. Grade-recovery curves at different air recoveries (unconstrained).

5.5.1.2 Scenario 2: Control α_k above a set of target values and manipulate both J_{gSP_k} and L_{SP_k}

To highlight the effect that α_k has on controller behaviour, a second simulation was performed where both J_{gSP_k} and L_{SP_k} are allowed to vary - but where α_k is only penalised in the objective function when below a defined target - not above the target, as shown by

$$\|\mathbf{e}^{y}_{k+j}\|^{q}_{\mathbf{Q}_j} = 10 \times (G_{SP_H} - G_H)^2 + 10 \times \sum_{k=0}^{4} \left(\max\{\alpha_{SP_k} - \alpha_k, 0\}\right)^2 . \tag{5.12}$$

The grade-recovery curves shown in Figure 5.11 confirms that the same concentrate grade can be obtained at different air recoveries and that in general, higher air recoveries result in higher mineral recoveries. The smooth grade-recovery curve in Figure 5.11 also shows the expected relationship between grade and recovery—similar to what was shown in Figure 1.3. However, any point on the smooth grade-recovery curve shown in Figure 5.11—where α_k was not explicitly controlled—

represents sub-optimal behaviour. The horizontal lines on the right-hand side of the smooth curve consistently achieve higher recoveries at the same grade as the smooth grade-recovery curve where α_k was not controlled, highlighting the importance of considering α_k in grade and recovery optimisation strategies.

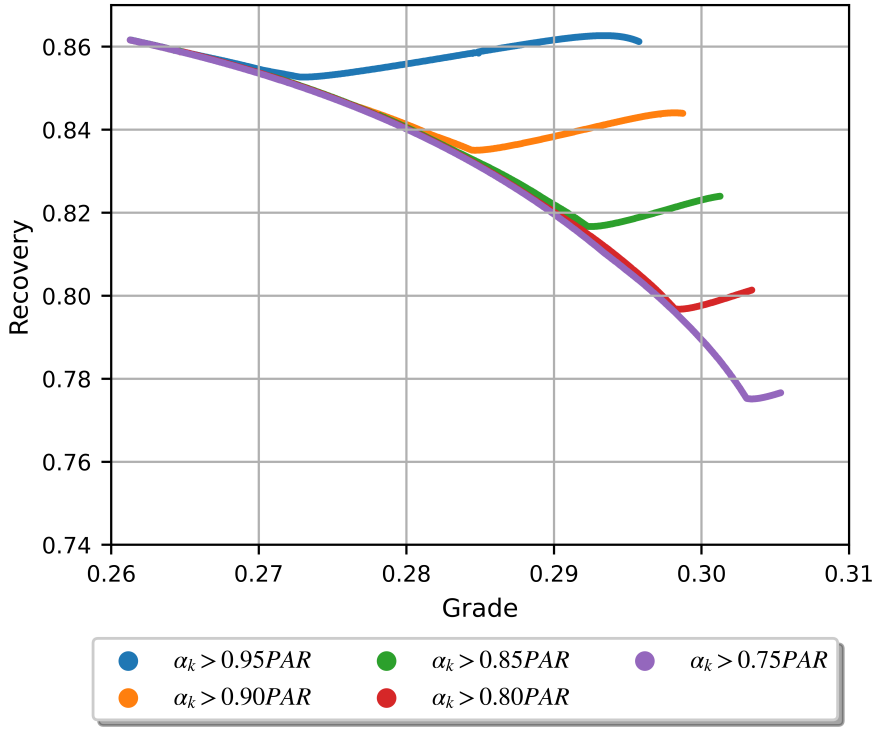

Figure 5.11. Grade-recovery curves at different minimum air recoveries (unconstrained).

5.5.1.3 Scenario 3: Control α_k to a set of target values and manipulate only J_{gSP_k}

The experimental trial conducted by Hadler *et al.* (2010a) focused on varying J_{g_k} only. The simulation was hence repeated to only allow variation in J_{gSP_k} while keeping L_{SP_k} constant at values that would yield $h_{f_k} = 120$ mm for Rougher Cells 1 and 2 and $h_{f_k} = 110$ mm for Rougher Cells 3 and 4, to be consistent with the froth depths that were measured during the trial conducted by Hadler *et al.* (2010a). The objective function (5.11) described for Scenario 1 was used for this simulation.

The results are shown in Figure 5.12. When the froth depths, h_{f_k}, are kept constant, the ranges of grades and recoveries that can be achieved at a specific air recovery, α_k, are limited, and the resulting grade-recovery curves at different values of α_k can be approximated as a single curve. The recoveries for the scenario when h_{fk} is not varied (see Figure 5.12) are lower than when h_{fk} is varied (see Figure 5.10), with the difference in recoveries being a function of the choice of h_{fk} and the target concentrate grade G_C. Figure 5.12 still shows how higher air recoveries, α_k, correspond with higher

mineral recoveries R_C. However, different to the results shown in Figure 5.10 where h_{fk} was adjusted to maximise air recovery (α_k) for a desired grade (G_C), there is much less scope to maximise air recovery (α_k) at a target grade (G_C) when froth depths (h_{fk}) are fixed.

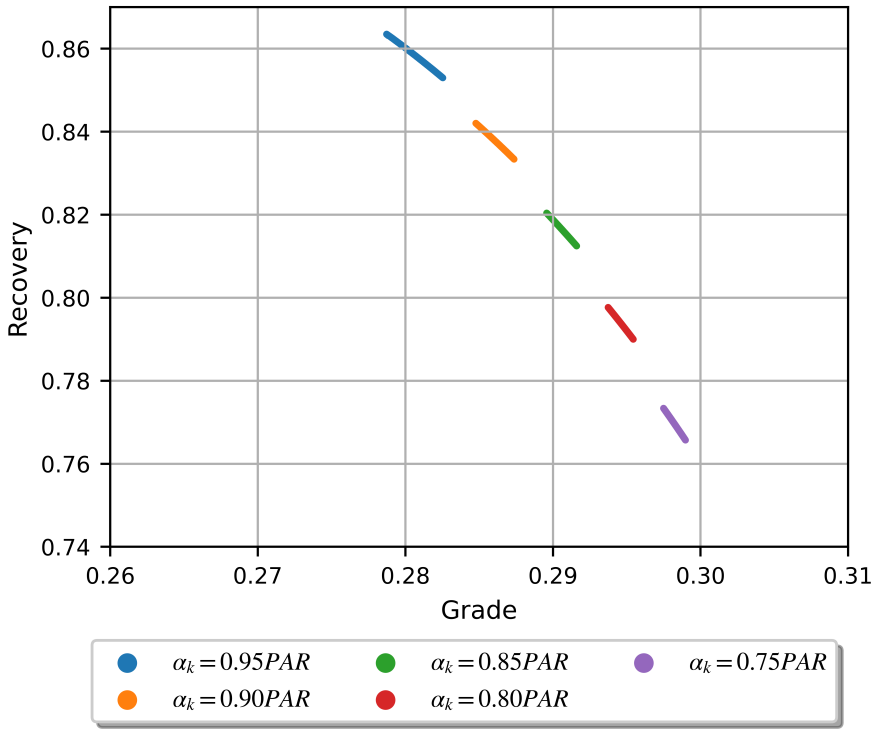

Figure 5.12. Grade-recovery curves at different air recoveries (h_{f_k} not varied).

The ranges of J_{g_k} and h_{f_k} for the three scenarios are compared in Table 5.7. The ranges of J_{g_k} in Scenario 3, where L_{SP_k} was not varied, were similar to the ranges used in the industrial trial conducted by Hadler *et al.* (2010a) and did not extrapolate beyond the reported dataset. Although caution should be used in interpreting simulation results based on an extrapolated data range (as done in the simulation where L_{SP_k} and J_{gSP_k} were varied), it is clear that by keeping h_{f_k} constant and only adjusting J_{gSP_k}, the range of achievable grades and recoveries are restricted considerably, and such a configuration could potentially prevent the peak in air recovery from being obtained, as described by Hadler *et al.* (2012).

Table 5.7. Ranges of manipulated variables.

Variable	Unit	Scenario 1 (Figure 5.10)	Scenario 2 (Figure 5.11)	Scenario 3 (Figure 5.12)
J_{g_k}	mm/s	6.3 - 9.6	6.6 - 9.6	7.0 - 7.9
h_{f_k}	mm	26 - 322	26 - 322	110 - 120

5.5.2 Simulation Study 2: Disturbance rejection

In this section, the ability of the MPC controller to reject typical disturbances that are expected to occur on an industrial flotation site is evaluated. The controller design and objectives described in Section 5.4 are used, and the model described in Chapter 3 is used for the controller, MHE and simulator. Relative weights of the **Q** and **S** matrices as part of the MPC objective function shown in (5.4) are listed in Tables 5.8 and 5.9.

Table 5.8. Weightings on controlled variables (diagonal elements of $\mathbf{Q}_j$ in (5.4)).

Variable	Weight
L_k	1.0
L_H	1.0
G_H	1000
R_C	0.01

Table 5.9. Weightings on control actions (diagonal elements of $\mathbf{S}_j$ in (5.4)).

Variable	Weight
J_{gSP_k}	1.0
L_{SP_k}	100
z_k	0.1
Q_H	0.1

Disturbances in volumetric feed rate to the flotation circuit (Q_{F_1}), feed density (ρ_F) and feed grade (G_F^i) could occur due to ore variability, or constraints or variability in upstream processes such as the grinding circuit. Variations in the feed particle size distribution received from the grinding circuit would affect the minimum (d_{pmin}) and maximum (d_{pmax}) particle sizes, and also the floatability constants ($K^{i,j}$), as variability in the particle size distribution is likely to cause variability in mineral liberation. The effect of gangue minerals, such as talc and mica, on the concentrate grade, froth stability and bubble size is described by Farrokhpay, Ndlovu and Bradshaw (2018) and is modelled as a disturbance in the floatability of the gangue minerals ($K^{i,j}$) and a step change in froth stability (α_k) and bubble size (D_{BF_k}). The disturbances that are included in this simulation study are summarised in Table 5.10. Note that the step disturbances on α_{OS_k} and D_{OS_k} were applied sequentially to the four cells, k, spaced 5 minutes apart.

Table 5.10. Simulated disturbances.

Time	Disturbance	Magnitude	Measured
30 min	Q_{F_1}	-5%	Yes
60 min	ρ_F	-5%	Yes
90 min	G_F^i	-5%	Yes
120 min	d_{pmin} and d_{pmax}	-50%	Yes
150 min	$K^{0,0}$ (Chalcopyrite)	$+10\%$	No
180 min	$K^{1,0}$ (Gangue)	$+20\%$	No
$210-225$ min	α_{OS_k}	$+0.05$	No
$240-255$ min	D_{OS_k}	$+0.2$cm	No

The measured disturbances that are shown in Table 5.10 are used both by the MHE to estimate process parameters and by the MPC controller to feed-forward the impact of disturbances and predict model responses. By measuring Q_{F_1} together with the measured states shown in Tables 4.2 - 4.4, the tailings flow rates, Q_{T_k}, can be estimated for all flotation cells, k, as shown by Oosthuizen *et al.* (2021), from which the valve constants, C_{v_k}, can be calculated. The measurement of the volumetric feed flow rate, Q_{F_1}, allows the MPC controller to compensate for the effect of feed flow rate disturbances on flotation cell levels and compensate for variations in residence times and variations in the mass transfers between flotation cells and between the pulp and froth phases. The combination of the measured volumetric feed flow rate (Q_{F_1}), feed density (ρ_F) and the feed grade (G_F^i) allows the total mass flow rate and

the mass flow rates of all the defined mineral species to the first flotation cell to be calculated. The MHE uses these measurements to estimate the flotation rate constants of all the species and classes ($K^{i,j}$). The feed size distribution (d_{pmin} and d_{pmax}) affects entrainment and need to be measured to allow the MHE to distinguish between particles reporting to the concentrate hopper due to entrainment and particles reporting to the concentrate hopper due to true flotation. The effect of the feed size distribution (d_{pmin} and d_{pmax}) can also be used to define different floatability classes within mineral species (e.g., fast and slow floating minerals due to different levels of liberation) but were not used in this simulation study.

Figure 5.13 illustrates the ability of the MPC controller to reject the disturbances that are listed in Table 5.10, with the control actions and resulting flow rates shown in Figure 5.14. The measured disturbance in volumetric feed flow rate (Q_{F_1}) at $t = 30$ minutes resulted in large controller responses, but the grade was maintained close to the setpoint, and the *instantaneous* recovery increased slightly. The disturbance in particle sizes (d_{pmin} and d_{pmax}) at $t = 120$ minutes was rejected, but the *instantaneous* recovery reduced by approximately 1% as a result. The unmeasured disturbances affecting $K^{0,0}$ at $t =$ 150 minutes and $K^{1,0}$ at $t = 180$ minutes were both rejected, resulting in an increase of approximately 2.5% in the *instantaneous* recovery. A control philosophy that can increase $K^{0,0}$ (potentially using reagent addition or improving the size distribution d_{pmin} and d_{pmax}) could thus have a significant impact on circuit performance. The increase in air recovery (α_k) at $t = 210$ minutes and bubble size (D_{BF_k}) at $t = 240$ minutes were both rejected and resulted in an increase in the *instantaneous* recovery of approximately 2.5% for each disturbance. Significant gains in *instantaneous* recovery can be realised by maximising α_k and controlling D_{BF_k} to a target (using revised models for D_{BF_k}), rather than responding to unmeasured disturbances in α_{OS_k} and D_{OS_k}. Overall, the concentrate grade was controlled in a narrow band with less than 0.5% deviation from the setpoint for all the simulated disturbances, while the calculated *instantaneous* recovery remained above 0.84 for the duration of the simulation.

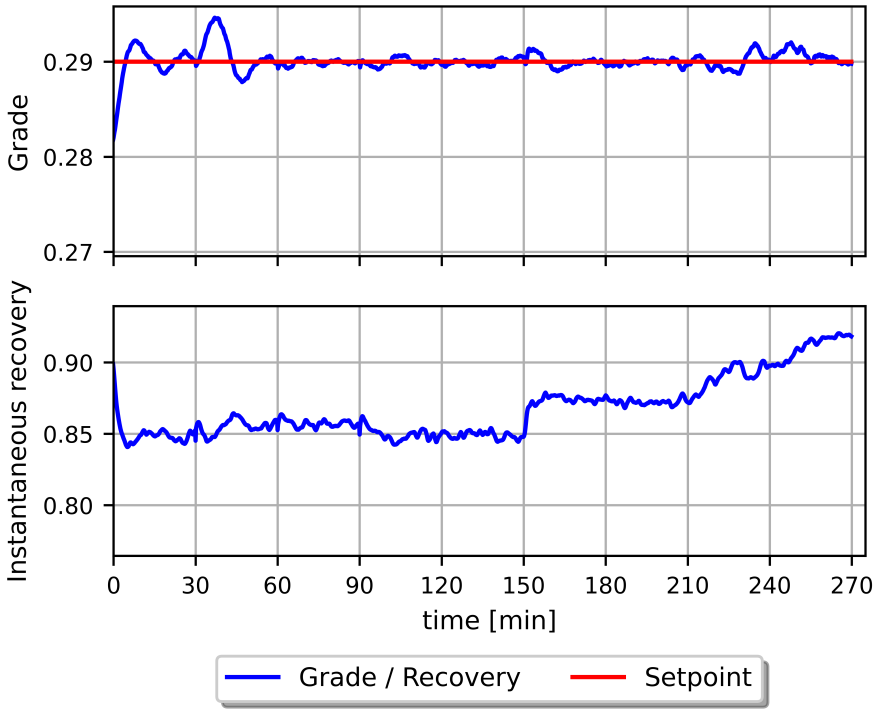

Figure 5.13. Grade and instantaneous recovery for the disturbances shown in Table 5.10.

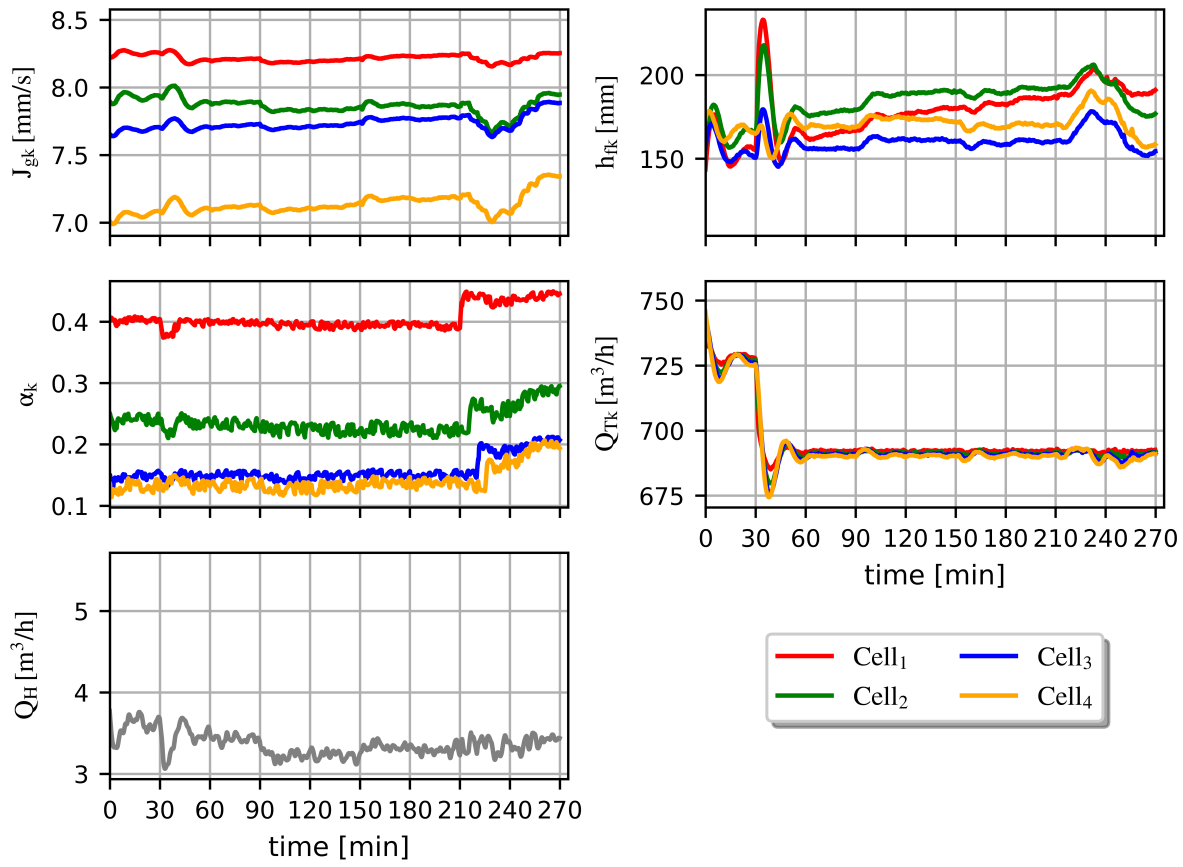

Figure 5.14. Control actions to reject the disturbances shown in Table 5.10 and α_k.

5.5.3 Simulation Study 3: A comparison of grade controllers

Grade control strategies employed on industrial sites can include reagent addition, control of recirculating loads and mass pull control (Shean and Cilliers, 2011). The aeration rate setpoint (J_{gSP_k}) and froth depth (h_{f_k}) (by adjusting L_{SP_k}) are often manipulated to achieve a desired concentrate mass pull rate from a flotation cell by relying on the principle that an increase in a concentrate mass pull rate will result in an increase in recovery and a decrease in concentrate grade. Without a measurement of air recovery and a model to take the effect of air recovery into account, a linear grade controller will typically increase the mass pull rate in an attempt to increase recovery by increasing J_{gSP_k} and decreasing h_{f_k} independently. However, Hadler *et al.* (2010b) showed how the peak in air recovery determines if a higher mass pull rate results in an increase or a decrease in recovery. By not accounting for the effect of air recovery on the resulting mass pull rate, grade, and recovery, a linear (i.e., PI or PID) controller could operate a flotation cell in a sub-optimal region where an increase in the mass pull rate reduces recovery (Hadler *et al.*, 2010b). Without additional condition monitoring strategies or models to intervene when the recovery decreases excessively, the linear controller could potentially operate at a significantly reduced efficiency for extended periods.

In this simulation study, the benefit of a non-linear model-based control strategy (using the structure shown in Figure 5.1) for grade control is illustrated by comparing its performance to that of a linear mass pull-based control strategy that does not take the effect of air recovery into account. For the control of a single rougher flotation bank in isolation, recirculating streams are not considered. The mass pull controller of the non-model-based control strategy is implemented as a set of PI controllers on J_{gSP_k} and L_{SP_k} for each flotation cell, as shown in Figure 5.15. The shaded PID controllers for L_{SP_k}, as shown in Figure 5.15, are disabled for the simulations in Section 5.5.3.2, where only J_{gSP_k} is varied. The PI controllers and MPC were initialised at the same operating point that intersects with a data point from industrial data described by Hadler *et al.* (2010a) to ensure that the performance of the PI controllers and MPC are representative of typical plant operation.

The PI controllers were implemented using the velocity form of the PI controller algorithm (Seborg, Edgar and Mellichamp, 1989):

$$\Delta p_n = p_n - p_{n-1} = K_c \left[(e_n - e_{n-1}) + \frac{\Delta t}{\tau_I} e_n \right], \tag{5.13}$$

where Δp_n is the change in control action at sampling interval n, e_n and e_{n-1} are the errors between the grade setpoint and grade measurement at sampling intervals n and $n-1$ respectively, K_c is the

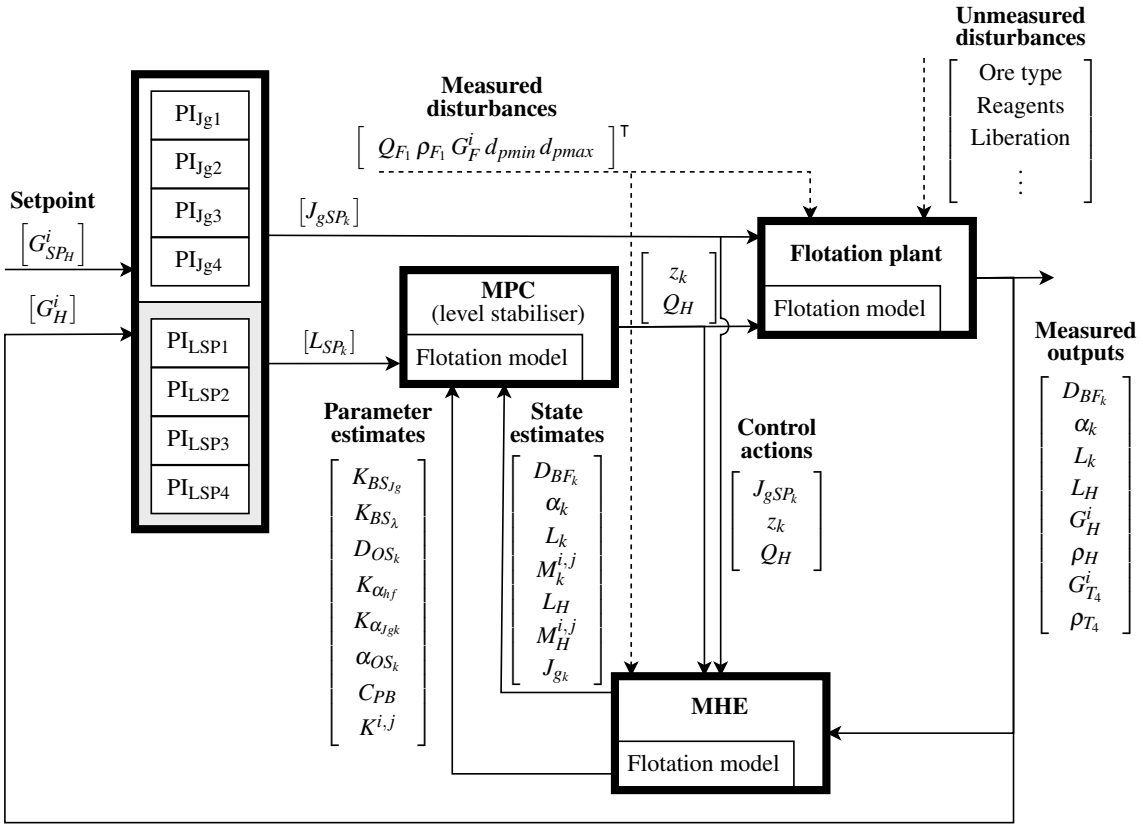

Figure 5.15. Using PI controllers to manipulate pulp levels L_{SP_k} and superficial air velocity J_{gSP_k} for grade control.

PI controller gain, τ_I is the controller integral time, and Δt is the period between successive control actions (p_n and p_{n-1}).

The signs of the controller gains were chosen to increase J_{gSP_k} and L_{SP_k} (to decrease h_{f_k}) when the grade is above the setpoint, thereby increasing mass pull. The same controller gains were used for four single-loop PI controllers—one for each cell— for J_{gSP_k} or L_{SP_k}. For the first scenario (where J_{gSP_k} and L_{SP_k} were manipulated) the controller gains were chosen to ensure a similar control range as that of the MPC controller, and for the second scenario (where only J_{gSP_k} was manipulated) controller gains were increased to obtain acceptable setpoint tracking. The PI controller configurations for the two scenarios are summarised in Table 5.11 and controller tuning settings for the two scenarios are summarised in Table 5.12.

Table 5.11. Simulation configurations (for MPC, see Figure 5.1, and for PI, see Figure 5.15).

Variable	Simulation 1	Simulation 2
PI L_{SP_k}	Manipulated	Fixed
PI J_{g_k}	Manipulated	Manipulated
PI Levels	Stabilised	Stabilised
MPC L_{SP_k}	Manipulated	Fixed
MPC J_{gSP_k}	Manipulated	Manipulated
MPC Levels	Stabilised	Stabilised

Table 5.12. PI controller tuning parameters.

Variable	Simulation 1 (K_c)	Simulation 1 (τ_I)	Simulation 2 (K_c)	Simulation 2 (τ_I)
PI J_{gSP_k}	-0.2	60 s	-5.0	120 s
PI L_{SP_k}	-0.1	30 s	-	-

5.5.3.1 Scenario 1: Manipulating J_{gSP_k} and L_{SP_k}

The concentrate grade setpoint was linearly increased over a period of ten hours from 0.285 to 0.310 for the simulation results shown in Sections 5.5.3.1 and 5.5.3.2. Figure 5.16 shows a graph of the linear change in the concentrate grade setpoint, and the resulting recoveries when PI controllers are used (see Figure 5.15) and when an MPC is used (see Figure 5.1) when both J_{gSP_k} and L_{SP_k} are manipulated.

The grade-recovery curves for the first scenario are shown in Figure 5.17, comparing a linear PI-based grade control strategy (see Figure 5.15) to a non-linear MPC grade control strategy (see Figure 5.1), varying both J_{gSP_k} and L_{SP_k}. The master MPC (grade controller and recovery optimiser) was configured to control the grade to setpoint (see Figure 5.16) and maximise recovery. The same slave MPC (stabilisation controller) was used for both simulations to stabilise flotation cell and concentrate hopper levels. It is clear that the non-linear MPC controller outperforms the linear controller by a large margin by consistently achieving higher recoveries than the linear controllers at the same grade. Figure 5.18

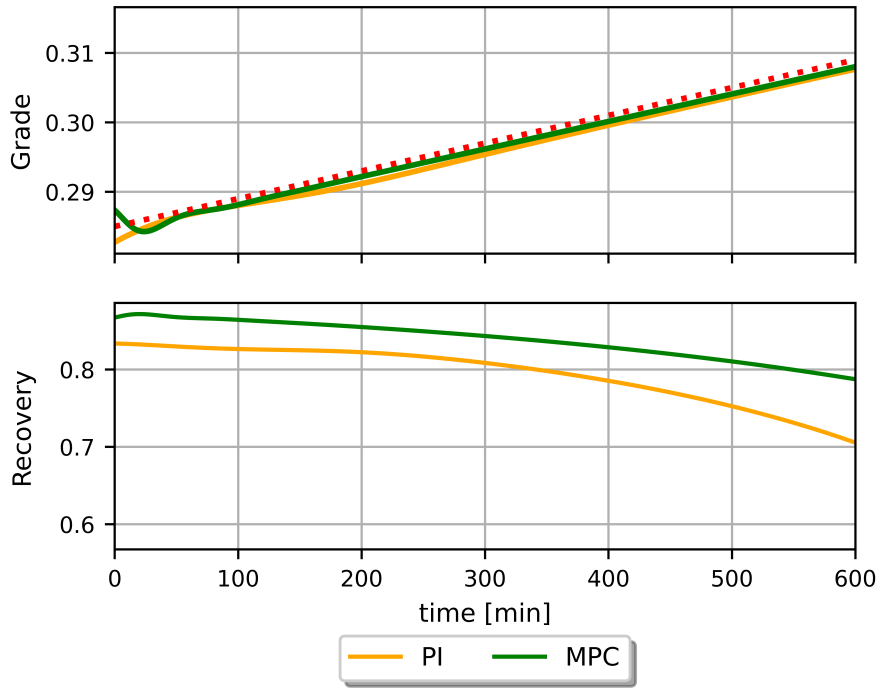

Figure 5.16. Scenario 1: Linear change in grade setpoint to compare controllers (scenario 1).

shows the changes in J_{g_k}, h_{f_k} and α_k over time to achieve the grade setpoint that is shown in Figure 5.16.

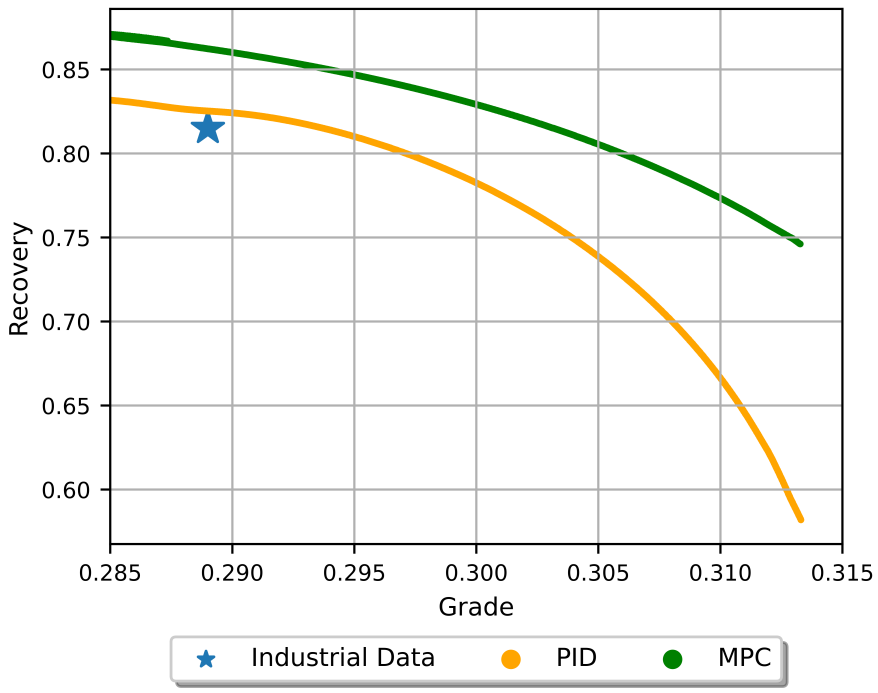

Figure 5.17. Scenario 1: Grade-recovery curves for PI control compared to MPC control (J_{g_k} and L_{SP_k} manipulated).

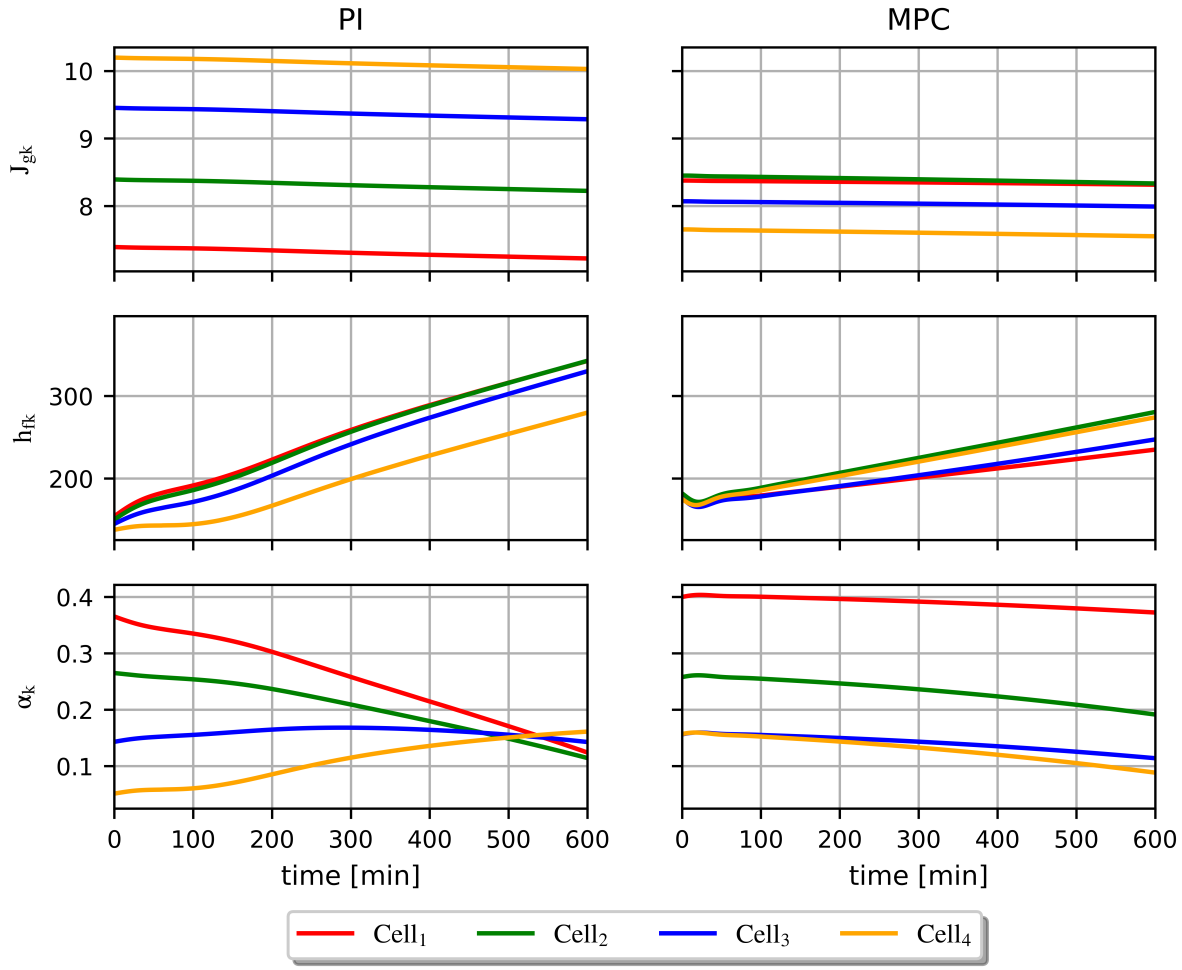

Figure 5.18. Scenario 1: Changes in J_{g_k}, h_{f_k} and α_k over time, comparing PI control to MPC control (J_{g_k} and L_{SP_k} manipulated).

5.5.3.2 Scenario 2: Manipulating J_{g_k} only

The grade-recovery curves for the scenario where only J_{gSP_k} is varied are shown in Figure 5.19, including an operating point from the dataset used by Hadler *et al.* (2010a). The master MPC (grade controller and recovery optimiser) was configured to control the grade to setpoint and maximise recovery, in addition to maintaining stable flotation cell and concentrate hopper levels. h_{f_k} was set to the default values of 120 mm for the first two cells, and 110 mm for Cells 3 and 4, as described by Hadler *et al.* (2010a). L_{SP_k} was kept constant for both simulations and the starting points for the PI controllers were chosen to correspond with the average PAR points that the model fit was based on.

Although the recoveries shown in Figure 5.17 (where both J_{gSP_k} and L_{SP_k} were manipulated) are higher than the recoveries shown in Figure 5.19 (where only J_{gSP_k} was manipulated), the non-linear MPC controller also outperforms the linear controller when only J_{g_k} is manipulated, consistently achieving higher recoveries than the linear controllers at the same grade. Figure 5.20 shows the changes in J_{gSP_k} and α_k over time to achieve the grade setpoint shown in Figure 5.21. h_{f_k} remained constant as L_{SP_k} was not changed for this simulation.

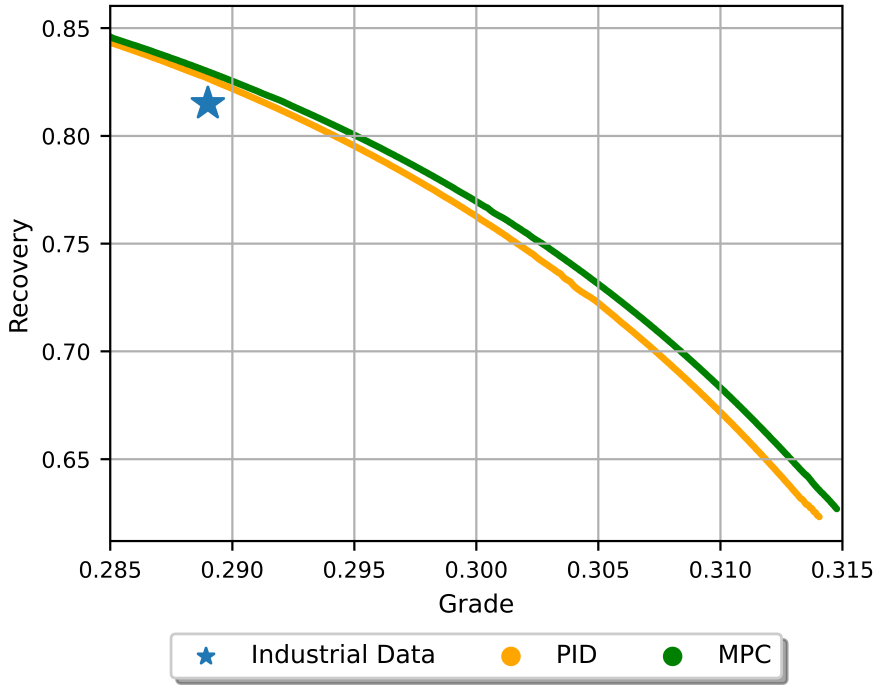

Figure 5.19. Scenario 2: Grade-recovery curves for PI control compared to MPC control (only J_{g_k} manipulated).

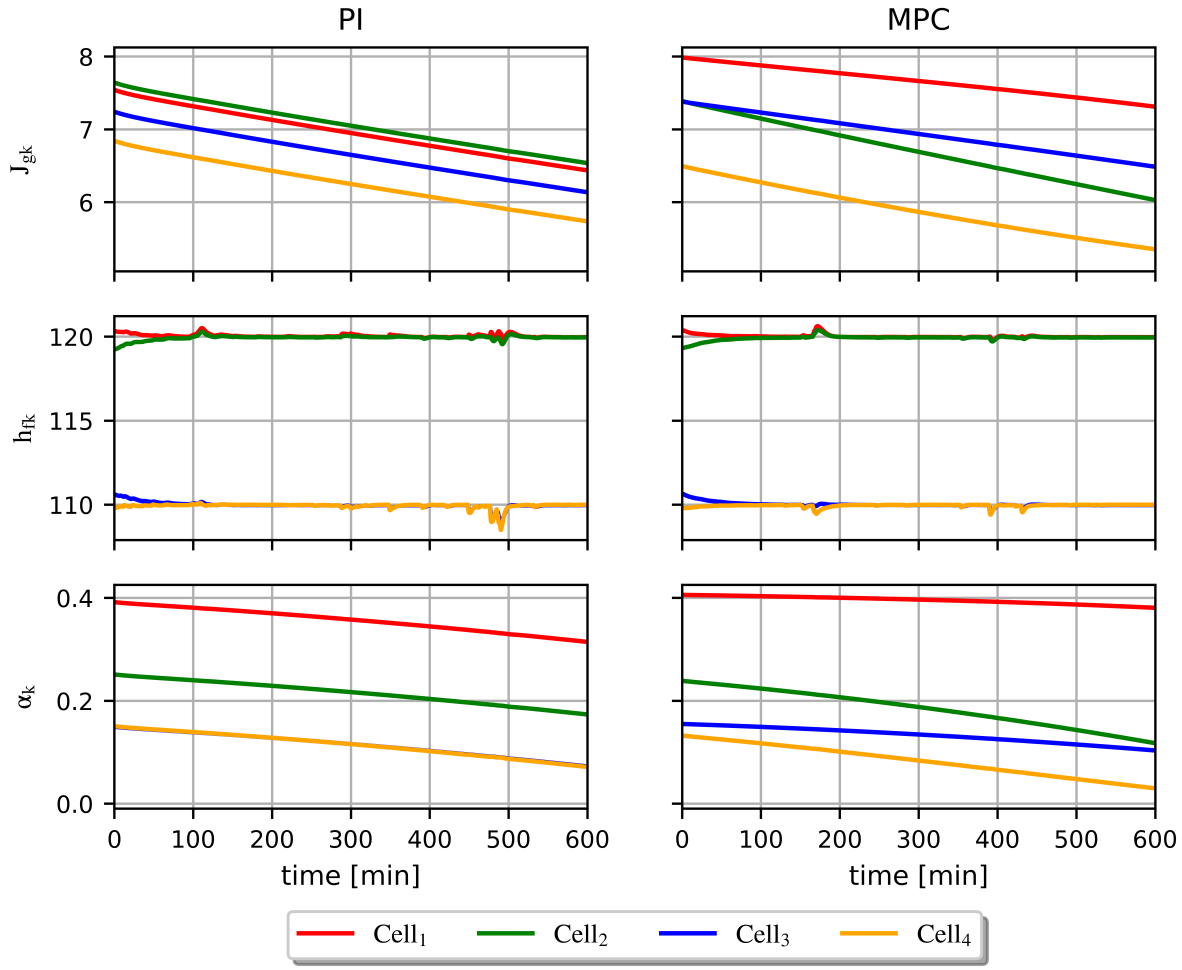

Figure 5.20. Scenario 2: Changes in J_{g_k}, h_{f_k} and α_k over time, comparing PI control to MPC control (only J_{g_k} manipulated).

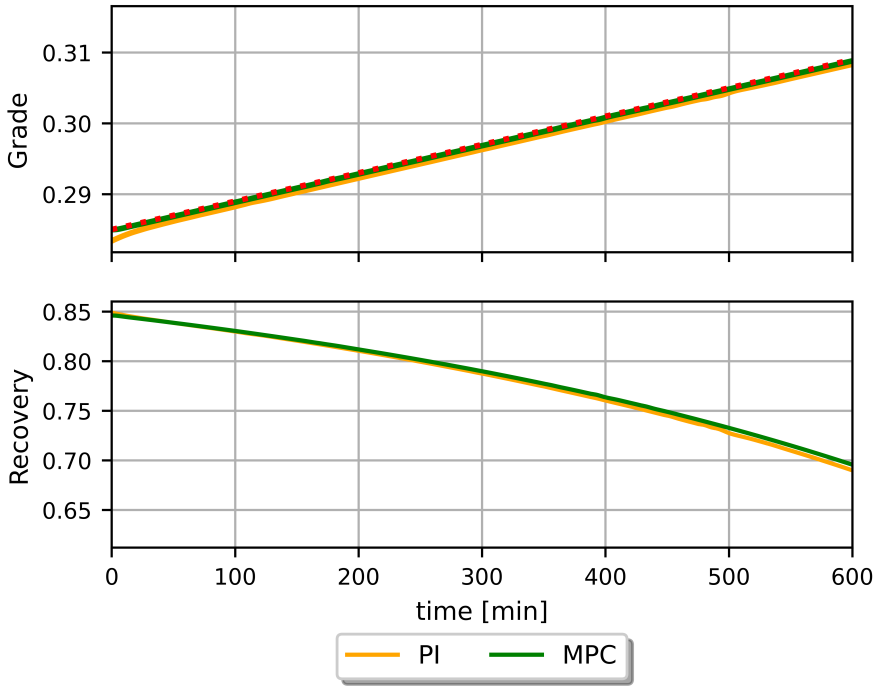

Figure 5.21. Scenario 2: Linear change in grade setpoint to compare controllers (scenario 2).

5.5.3.3 Scenario 3: Best case scenario for a linear PI control strategy

When the performances of different controllers are compared numerous factors can contribute to one controller outperforming the other, potentially biasing the result. In this section it was investigated whether an operating point and tuning parameters could be chosen where the linear PI control strategy described in Section 5.5.3.1 could match or exceed the performance of the non-linear MPC strategy. The following factors were considered:

- PI controller parameters in Section 5.5.3.1 were chosen to obtain similar ranges for the manipulated variables (J_{gSP_k} and L_{SP_k}) in both the MPC and PI control strategies while achieving acceptable setpoint following. The same PI controller parameters (that were used in Section 5.5.3.1) were used in this section.
- An increasing grade setpoint was simulated to ensure that the PI control actions (as a function of the control parameters and initial operating points) would reduce. This is required to prevent the linear PI control strategy from operating in a region relative to the PAR where the gain between recovery and J_{gSP_k} or L_{SP_k} is reversed.
- The initial values of J_{gSP_k} and L_{SP_k} for both the PI controllers and the MPC were chosen to correspond with the PAR values used in the model fit. This is different to the simulation results shown in Section 5.5.3.1 where the initial values for both controllers were set equal to a different data-point reported by Hadler *et al.* (2010a) - not the PAR point.

Figure 5.23 shows the grade and recovery trends for the non-linear MPC (Figure 5.1)and linear PI (Figure 5.15) controller strategies under ideal conditions, and confirms that both controllers tracked the grade setpoint adequately. Grade-recovery curves for the MPC and PI controllers are almost identical, confirming that the PI control strategy can achieve similar performance as the MPC strategy under ideal operating conditions (see Figure 5.22). Figure 5.24 compares J_{g_k}, h_{f_k} and α_k for the non-linear MPC and PI control strategies under ideal condition, showing similar trends for J_{g_k}, h_{f_k} α_k. It is thus possible to choose initial operating points, an operating range and controller tuning parameters that would result in a linear non model-based control strategy (PI controllers) matching the performance of a non-linear model-based control strategy (MPC) in a simulated environment. However, in an industrial environment where

- the PAR point and J_{g_k} and h_{f_k} values at the PAR point are not continuously estimated,
- the PAR point changes over time as reported by Phillpotts *et al.* (2021), and
- the PAR point might shift to a point where an increase in J_{g_k} would result in a decrease in recovery,

the non model-based control strategy (PI master controllers shown in Figure 5.15) would under-perform a non-linear model-based control strategy (MPC master controllers shown in Figure 5.1) by a margin dependent on the deviation from ideal operating conditions.

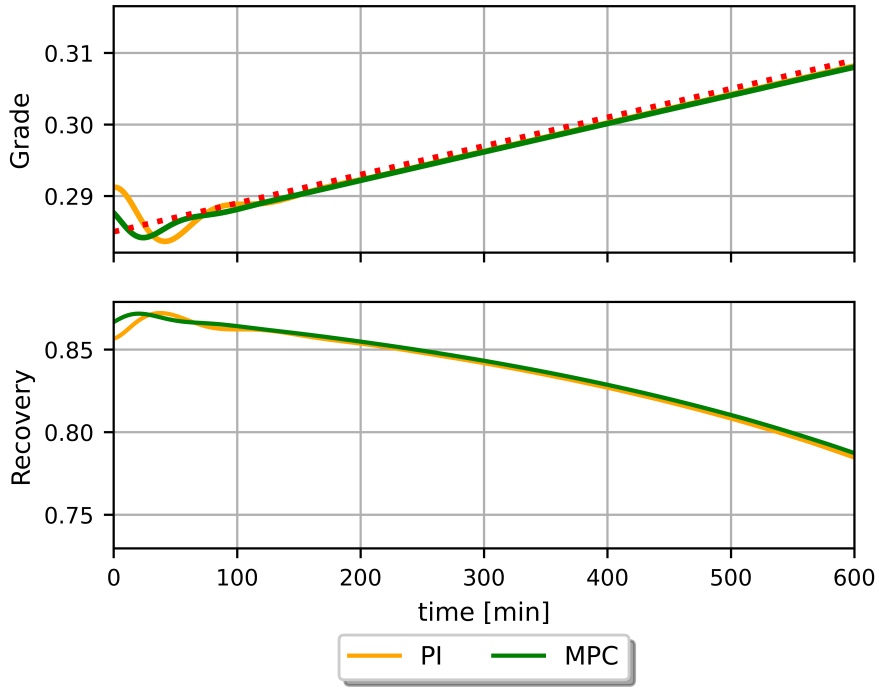

Figure 5.22. Scenario 3: Linear change in grade setpoint to compare controllers under ideal conditions.

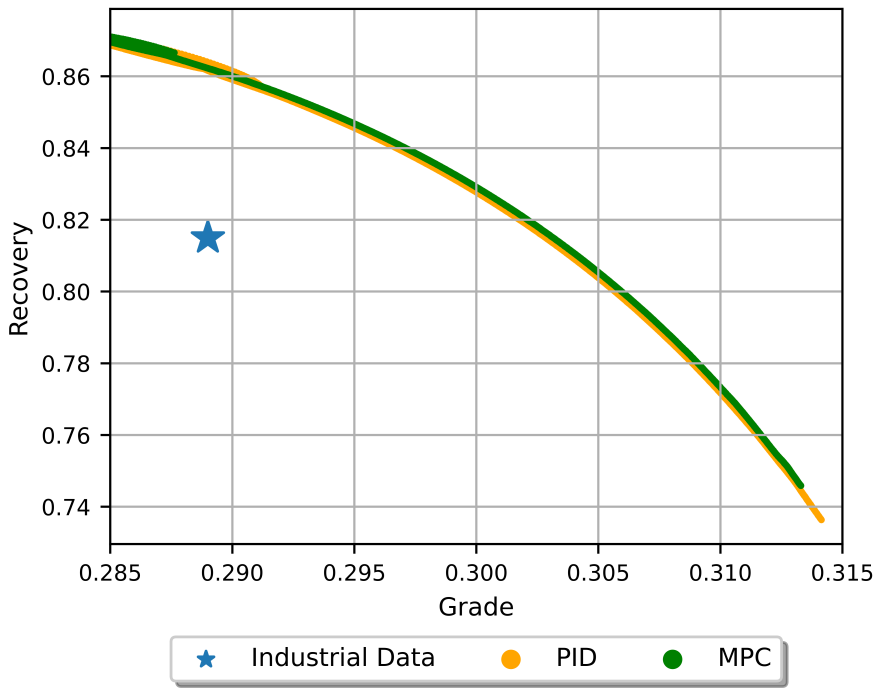

Figure 5.23. Scenario 3: Grade-recovery curves for PI control under ideal conditions compared to MPC control (J_{g_k} and L_{SP_k} manipulated).

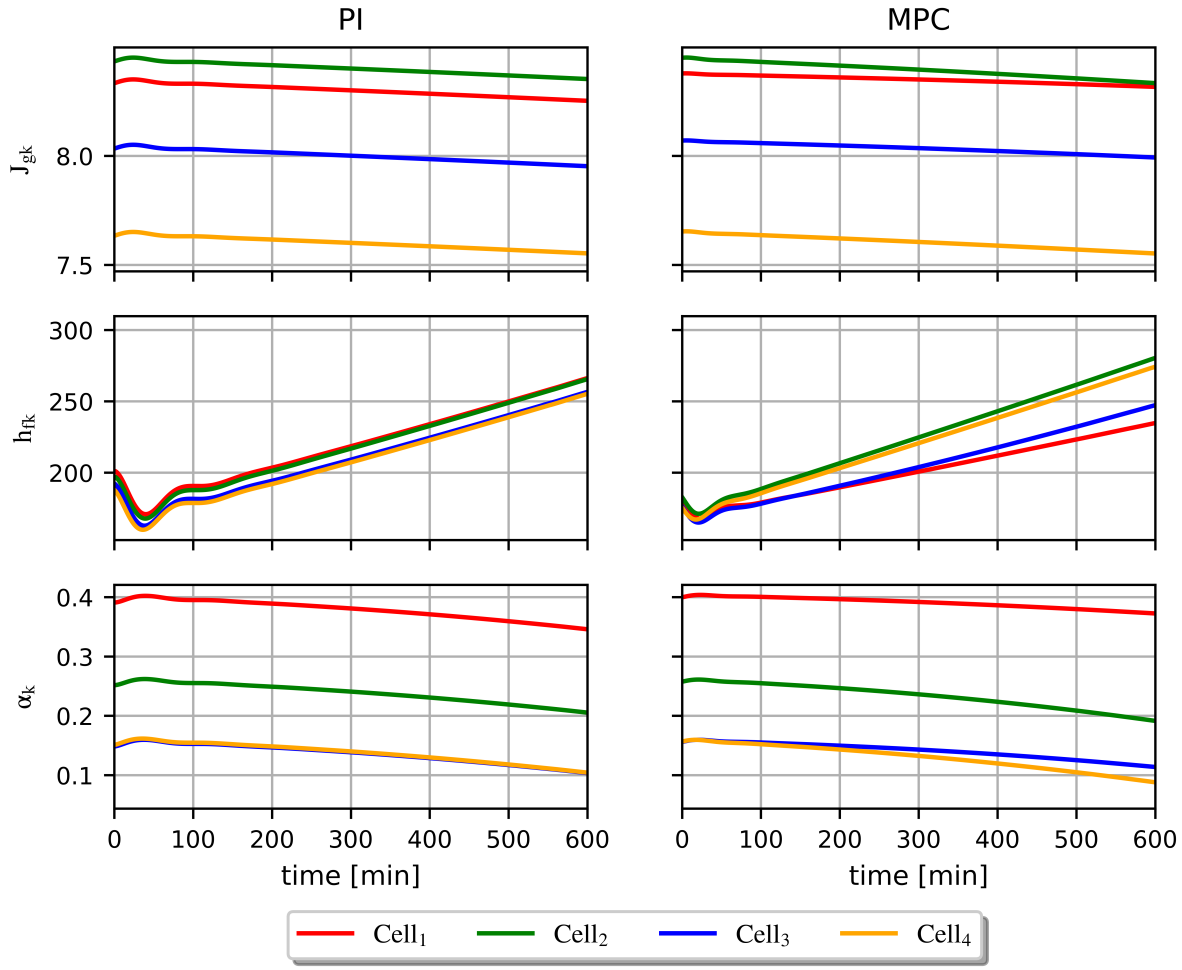

Figure 5.24. Scenario 3: Changes in J_{g_k}, h_{f_k} and α_k over time, comparing PI control under ideal conditions to MPC control (J_{g_k} and L_{SP_k} manipulated).

5.6 DISCUSSION

The peak in air recovery that is described by Hadler and Cilliers (2009) implies that a non-linear model-based control strategy is required to optimise flotation operation by maintaining the operating point as close as possible to the air recovery peak. The non-stationary nature of the peak in air recovery, as reported by Phillpotts *et al.* (2021), requires a strategy capable of dynamically adapting the model to track variability in the air recovery peak position over time. The non-linear flotation model shown in Chapter 3 and described by Oosthuizen *et al.* (2021) provides the basis for model-based control and optimisation implementation to dynamically track variations in the peak in air recovery while using fundamental models to model the transfer of mineral species between flotation cells and between the pulp and froth phases within a flotation cell. Key aspects of the model described in Chapter 3 are that the model uses measurements that are commonly available on industrial flotation circuits and that the unmeasured model states and model parameters can be estimated from commonly available real-time measurements on an industrial site, as confirmed by an observability analysis performed in Chapter 4.

A control framework comprising a robust non-linear MPC and an MHE is described by Lucia *et al.* (2017), which can be used to implement a non-linear model-based control strategy based on the flotation model described in Chapter 3. The MHE is a key component of the control and optimisation solution that is required to track variations in the peak air recovery point and other flotation parameters over time. In Section 5.3, it was demonstrated that the MHE could be used to estimate model parameters—even when the measurement noise is of a similar magnitude as the variability in parameters that are being estimated. The flexible structure of the MHE cost function and the ability to specify constraints on parameters and states allow for a robust solution that can be guaranteed to remain within a feasible operating range in the presence of large disturbances and modelling and measurement errors.

A basic MPC controller design was described in Section 5.4 to combine the stabilisation of flotation cell and concentrate hopper levels with optimisation of aeration rates (J_{g_k}) and froth depth (h_{f_k}) (by adjusting J_{g_k} and L_{SP_k}), to maximise recovery at a target concentrate grade. Additional constraints (e.g., a threshold on minimum recovery, below which, the grade may be compromised) can be added in future to address operational constraints on industrial sites, or the non-linear objective function can be modified to include economic objectives representative of trade-offs between—for example, smelter penalties, reagent cost and recovery.

In Section 5.5.1, a comparison of grade-recovery curves that are generated at different air recoveries clearly shows how operating at higher air recoveries are equivalent to shifting the process to a more efficient grade-recovery curve, which achieves higher recovery at the same grade (see Figure 5.10). The peak in air recovery is thus a key parameter to include in a flotation optimisation strategy. A second set of curves for a scenario where only aeration rates are varied—not froth depth—provided similar results (higher air recovery corresponding to operation at a more efficient grade-recovery curve) but over a smaller operating range (see Figure 5.12). When only J_{g_k} is used as a manipulated variable, the selection of the froth depth profile for the flotation section dictates the range of air recoveries and grades that can be achieved in the circuit. Unless the froth depth profile is optimised and adjusted over time to suit operating conditions, recovery could be considerably lower than what could be achieved when both L_{SP_k} and J_{gSP_k} form part of a non-linear model-based control strategy.

Section 5.5.3 compares the non-linear MPC controller designed in Section 5.4 to a linear PI-based strategy (see Figure 5.16) to maximise recovery while maintaining a target grade. The limitation of a linear non-model based control strategy, as implemented using PI controllers, is that such a strategy does not consider any non-linearities in the inverse relationship between grade and recovery or the sign change in the relation between α_k and Jg_k when the PAR point is crossed. The non-linear MPC controller consistently outperformed the PI controllers on recovery by moving the process to a more efficient grade-recovery curve that maximises recovery over a range of grade setpoints. This is confirmed by the grade-recovery curves shown in Figures 5.17 and 5.19, where the MPC controller consistently achieved higher recoveries at the same grade as the linear PI-based control strategy. However, the benefit provided by the MPC when both J_{gSP_k} and L_{SP_k} are manipulated (Figure 5.17) exceeds the benefit when only J_{gSP_k} is manipulated (Figure 5.19) by a significant margin, with an average increase in recovery of 5.8% shown in Figure 5.17, compared to 0.32% in Figure 5.19. Section 5.5.3.3 showed how—by selecting and ideal set of operating conditions and controller tuning parameters—a linear PI based control strategy can match the performance of the non-linear model-based strategy. Under non-ideal conditions (e.g., on an industrial flotation circuit) the results shown in Section 5.5.3.1 are more representative of the expected benefit that could be achieved by using a non-linear model-based controller.

In Section 5.5.2, Figure 5.13 demonstrates how the MPC controller is able to reject typical disturbances that can be expected to occur on an industrial flotation plant, which include measured disturbances in the feed and unmeasured disturbances as a result of ore changes or variability in the

feed from the grinding process. The controller rejected all the disturbances while maintaining the concentrate grade within a narrow band around the setpoint and maximising recovery. Disturbances, such as the grind size (d_{pmin} and d_{pmax}), volumetric feed flow rate (Q_{F_1}), feed density (ρ_F) and potentially the floatability of minerals ($K^{i,j}$) due to variability in liberation, are directly related to the upstream grinding process, which provides opportunities to integrate optimisation of the grinding and flotation processes (le Roux and Craig, 2019). Although the controller managed to reject the disturbances in froth stability / air recovery (α_k) and bubble size (D_{BF_k}) well, the reagent mixture would typically be adjusted when an increase in specific minerals (e.g., talc in the feed) results in a significant change in froth stability and bubble size, as described by Farrokhpay *et al.* (2018). Future work should expand the flotation model to include reagents as manipulated variables to the controller—potentially replacing the D_{BF_k} model with a model dependent on reagents and with a higher sensitivity to changes in the model inputs than the existing model.

5.7 CONCLUSION

Air recovery is a critical parameter to include in a flotation optimisation strategy. It provides the mechanism to move towards an optimal grade-recovery curve with the highest recovery for a desired grade instead of moving along a sub-optimal grade-recovery curve. A non-linear model-based control strategy combined with a state and parameter estimator are key components of such a flotation optimisation strategy. It provides the means to adapt the model to rapid changes in the peak in air recovery and to control the flotation process at an optimal operating point. The non-linear flotation model, MHE and non-linear MPC presented in this thesis consistently outperformed the linear control strategies, and provide a viable framework to optimise an industrial flotation circuit that relies only on real-time measurements that are commonly available on industrial flotation circuits. This supports the second hypothesis in Section 1.5.

CHAPTER 6 DISCUSSION AND CONCLUSION

6.1 SUMMARY

The aim of this work is to develop a flotation model for real-time control and optimisation applications on industrial flotation circuits that include key flotation mechanisms. The feature that distinguishes the flotation model developed in Chapter 3 from other models that are available in the literature and makes it suitable for real-time control and optimisation applications, is its ability to continuously estimate key flotation parameters and states from real-time measurements that are commonly available on industrial flotation circuits. It was shown through an observability analysis in Chapter 4 and demonstrated through a simulation study in Chapter 5 that model parameters can be estimated from real-time process measurements and that it is viable to include the flotation model in a non-linear model-based controller for control and optimisation applications. The structure that comprises a non-linear flotation model, a state and parameter estimator, and a model predictive controller provides a viable solution to be used in industrial flotation control and optimisation applications.

6.2 FLOTATION MODEL STRUCTURE

Three shortcomings have been identified in flotation models that are available in the literature that limit the extent to which these models can be used in industrial control and optimisation applications:

- Steady-state models are often used for plant design without considering process dynamics.
- Detailed steady-state or dynamic models rely on an extensive set of model parameters that need to be determined through sampling campaigns. While many variables are unlikely to change much over time, parameters related to ore characteristics and operating conditions are expected to vary considerably over time and need to be updated regularly to maintain model accuracy when process characteristics change.

- Flotation models that are used in model-based control applications are often linear empirical models that do not take non-linearities, such as air recovery, into account.

A simple dynamic flotation model was developed that combines fundamental mass and volume balances with froth image properties and empirical models. While more comprehensive and detailed flotation models have been developed, this model distinguishes itself from other models by relying only on measurements that are commonly available in real time on industrial flotation circuits to estimate key flotation parameters and model states. The flotation mechanisms and properties that were identified in Chapter 2 were included in the model, and where specific interactions in the flotation process (e.g., variations in turbulence in the pulp phase) are not modelled explicitly, the effect of such variability can still be observed through variability in flotation parameters. The flotation model described in Chapter 3 provides a minimum viable model definition that describes the key mechanisms that contribute to the flotation process in sufficient detail to be used in real-time control and optimisation applications, and this model can potentially be expanded and built on in future.

6.3 STATE AND PARAMETER ESTIMATION

Real-time measurements of concentrate grades provide information on different mineral species that are present in the concentrate hopper but not on the flotation mechanism that results in each mineral being transferred to the concentrate hopper or on the relative contributions from each flotation cell. Real-time estimation of the model parameters that distinguishes between the mechanisms of true flotation and entrainment for all the mineral species allows for the design of a control and optimisation strategy that is capable of addressing the root cause of deviations from the desired grade or recovery by controlling each flotation cell in an optimal fashion. For the flotation model in its current form, such a control and optimisation strategy could calculate the optimal combination of froth depth and aeration rates on each flotation cell to achieve the desired control and optimisation objectives of maintaining a target concentrate grade while maximising recovery. However, the additional information on flotation parameters opens up opportunities to integrate the control of reagent addition into the existing structure too, as described in Section 6.5.

It has been demonstrated in Chapter 4 that an MHE can be designed for the flotation model of Chapter 3 to estimate the key flotation model parameters reliably in the presence of noisy measurements. A viable solution is thus presented to estimate key flotation parameters from real-time measurements that are commonly available on industrial flotation circuits.

In industrial implementations modelled and measured process responses would differ due to process noise and modelling errors, which could reduce the accuracy of parameter estimates—particularly for the empirical models. An error term for process noise, $\mathbf{w}_k$ could be included in the MHE objective function shown in (5.2) to compensate for model errors. Such an error term, $\mathbf{w}_k$ could reduce the responsiveness of model parameters to rapid process changes, but would also reduce undesired fluctuations in model parameters caused by a mismatch between the measured and modelled process responses.

6.4 SIMULATION RESULTS

Three sets of simulation results were presented in Chapter 5. The first set demonstrated how higher air recoveries result in higher concentrate recoveries for the same grade. This confirms that the non-linear characteristics of air recovery form an important model state that needs to be considered in flotation control and optimisation strategies. Linear optimisation strategies that do not explicitly consider the peak in air recovery need to assume operation on one side of the air recovery peak and include functionality to either restrict the operating range in an attempt to avoid operation on both sides of the peak or include some intervention mechanism when the linear controller does not have the desired effect. In both cases, operation would be sub-optimal.

The second simulation study showed how the system comprising the MHE and MPC could be used in a flotation control and optimisation strategy to maximise mineral recovery for a desired concentrate grade in the presence of typical disturbances. The results showed how the concentrate grade could be maintained close to a target setpoint for most disturbances while mineral recovery was maximised throughout the simulation. The non-linear characteristics of air recovery form a key part of the model-based control and optimisation strategy that leverage the increase in mineral recovery when flotation cells are operated at high air recoveries. However, the peak in air recovery is not stationary and needs to be estimated continuously to maximise the performance of the flotation circuit over a range of operating conditions. This second simulation study confirms that the control and optimisation strategy that was developed in Chapter 5 is capable of maintaining system performance in the presence of noise and measured and unmeasured disturbances that one would expect to find on an industrial flotation circuit.

The third simulation study demonstrated the benefit of using a non-linear model-based control strategy

for flotation optimisation over a linear PI controller-based strategy, to control the concentrate grade to a target while maximising recovery. For the linear control strategy, the controller gains and operating region were chosen conservatively to ensure that the controllers did not exceed the aeration rate or froth depth at which the peak in air recovery occurs. This was to prevent the controllers from entering an operating region where the effect of froth depth or aeration rate on concentrate grade and recovery is reversed. Without such limits or additional logic linked to the control system, a PI-based control strategy could potentially push the circuit to an operating point of low grade and low mineral recovery to the concentrate due to low air recoveries. Given the non-linear characteristics of air recovery, plant optimisation can benefit significantly from a non-linear model-based approach.

6.5 FUTURE WORK

Various enhancements can be considered to include additional flotation mechanisms or include additional manipulated variables, such as the reagent addition rates to the froth flotation model that was described in Chapter 3. Some recommendations are described in this section. For any model enhancements, it remains crucial that the model be re-evaluated for state observability, parameter identifiability and state controllability—similar to the analysis that was done in Chapter 4—to ensure that the model parameters can still be estimated in real time using only real-time measurements that are commonly available on industrial flotation circuits.

6.5.1 Reagent addition

Aeration rates and froth depths are often the first parameters to be automated in grade control strategies, as the direct cost associated with manipulating these variables are minimal. A suitable reagent mixture is critical to provide the desired operating conditions where froth depth and aeration rates can be manipulated within their operating ranges to achieve the desired concentrate grade and recovery. By including reagent addition rates as part of an automatic control and optimisation strategy, the operation of a flotation circuit will not be limited to optimal aeration rates and froth depths for a given combination of reagents but will also include the optimisation of reagents based on the estimated model parameters.

A frother is expected to affect bubble sizes, D_{BF_k}, and froth stability, α_k, in each flotation cell, k. The frother concentration in each flotation cell can be calculated from frother addition rates and volumetric flow rates into and out of each flotation cell, and the models for bubble size D_{BF_k} and α_k can be

expanded to model the effect of frother addition rates. The objective function may need to be revised to penalise frother addition to ensure that the cost of reagents are minimised.

Reagents, such as depressants, activators and collectors, are expected to affect the flotation rate constants, $K^{i,j}$, of the mineral species. Rather than having constant reaction rate constants (that are estimated from real-time measurements) in the model, the reaction rate constants can potentially be defined as a function of the concentrations of depressants, activators and collectors. The concentrations of different reagents in each flotation cell can be calculated from measured reagent addition rates and volumetric flow rates into and out of the flotation cells. Models of reagents will need to take interactions between different reagents into account.

6.5.2 Expanding the true flotation model to include particle size information

Particle size information is currently included in the entrainment model to model the preferential entrainment of light particles over heavy particles. The particle size distribution can also be included in the true flotation model. It is well documented (Wills and Napier-Munn, 2006) that true flotation is most effective within a band of size classes, as larger and heavier particles become detached from bubbles more easily, and smaller and lighter particles are easily swept past bubbles rather than colliding and attaching to the bubbles in the pulp phase.

One option to model the effect of the particle size distribution on true flotation is to define three size classes in the model for coarse, intermediate and fine particles—each with its own floatability characteristics. The simplest approximation is that true flotation only occurs within the defined particle size band and is zero outside it, but the error that is introduced by such an approximation needs to be considered. The alternative is to estimate the flotation rate constants of the coarse, intermediate and fine size classes individually from real-time measurements. The set of real-time measurements that were defined in Chapter 2 will need to be expanded to estimate additional floatability constants, but it may be possible if particle size information is also available on the concentrate streams.

6.5.3 Expanding the flotation model to include additional mechanisms contributing to flotation

Flotation model parameters such as the floatability constants $K^{i,j}$ lump together several mechanisms in the pulp and froth phases that contribute to the resultant minerals reporting to the concentrate hopper.

The effect of turbulence in the pulp phase is, for example, not modelled as was done in the model described by Bascur and Herbst (1982), and the mechanisms of particles attaching and detaching from the bubbles are not modelled separately. While the model parameters that were defined in Chapter 3 will adapt over time (based on real-time measurements) to account for all the flotation mechanisms that contribute to the overall floatability, a more detailed model's predictive capabilities is likely to improve as the fundamental flotation mechanisms are modelled in finer detail.

Should the flotation model described in Chapter 3 be expanded to model additional flotation mechanisms explicitly, maintaining state observability and parameter identifiability would be a key criterion to determine if such a model expansion is viable.

6.5.4 Investigating other flotation section configurations

A rougher flotation section generally has a simple configuration, with the tailings streams flowing sequentially from one flotation cell, k, to the next cell, $k+1$, and the concentrate streams from all the flotation cells combining into a concentrate hopper. For other flotation sections, such as cleaner sections, the concentrate streams typically flow in a counter-current direction relative to the tailings flows, with each flotation cell, k, receiving tailings flow from an upstream cell, $k-1$, and concentrate flow from a downstream cell, $k+1$.

A system analysis was performed in Chapter 4 on a rougher flotation section only, as described by Hadler *et al.* (2010a). The observability and controllability analysis would have to be repeated for different flotation sections and configurations to confirm that model parameters can be estimated from the available real-time measurements and that the process states are controllable for the specific configuration. Should the system not be observable with the real-time process measurements that were defined in Chapter 2, there could still be room to use additional real-time measurements or soft sensors based on, for example, visual froth characteristics to obtain a system that is state observable and parameter identifiable.

6.5.5 Integrating flotation and grinding circuits

Crushing and grinding circuits are commonly installed upstream of a flotation circuit to produce the desired particle size distribution required for the feed to the flotation circuit. Determining the ideal size distribution is not a trivial exercise, as the particles that contain the valuable minerals need to be

sufficiently liberated in the grinding process without over-grinding or using excessive energy in the grinding circuit. As the size distribution of the feed to the flotation process affects both true flotation and entrainment, the effect of finer grinding on both flotation mechanisms need to be considered.

The particle size distribution that is produced by the grinding circuit is only one aspect where there is scope to integrate the control of grinding and flotation processes to optimise the overall process:

- The throughput of the grinding circuit determines the residence time in the flotation circuit. Depending on ore characteristics, bottlenecks in the process and economic considerations, it could be beneficial to reduce throughput from the milling circuit to increase residence times in the flotation circuit to increase recoveries.
- Optimisation objectives of a grinding circuit would typically include the maximisation of grinding efficiency and throughput, subject to bottlenecks in the process. However, it is possible to achieve a finer grind at the same throughput by operating a grinding mill in a less efficient mode that favours attrition grinding over impact breakage. Depending on the economic objectives and relative contributions of the economic factors, it could be beneficial for the combined grinding and flotation processes to operate the grinding circuit in a sub-optimal fashion (in terms of specific energy consumption) to achieve a different feed size distribution to the flotation circuit that would maximise recovery.
- In addition to operating within the operational constraints of the flotation and milling circuits, an integrated automatic control and optimisation strategy can be designed to optimise the combined milling and flotation processes based on the economic objectives. Such an economic objective function needs to consider the cost of deviating from target product specifications and the cost of control actions (e.g., reagents and electricity cost) that can be used to compensate for disturbances that drive the product away from the desired specifications. While fixed costs of production and constraints on other downstream processes may limit the scope of such a strategy, an economic optimisation could potentially trade off strategies that can achieve the same objectives using different combinations of control actions, to maximise the operating profit for the combined grinding and flotation circuits.

REFERENCES

Ai, M., Xie, Y., Tang, Z., Zhang, J. and Gui, W. (2021). Deep learning feature-based setpoint generation and optimal control for flotation processes, *Information Sciences* **578**: 644–658.

Aldrich, C., Marais, C., Shean, B. J. and Cilliers, J. J. (2010). Online monitoring and control of froth flotation systems with machine vision: A review, *International Journal of Mineral Processing* **96**(1–4): 1–13.

Alves Dos Santos, N., Savassi, O., Peres, A. E. C. and Martins, A. H. (2014). Modelling flotation with a flexible approach–Integrating different models to the compartment model, *Minerals Engineering* **66**: 68–76.

Ata, S. (2008). Coalescence of bubbles covered by particles, *Langmuir* **24**(12): 6085–6091.

Baas, D., Hille, S. and Karageorgos, J. (2007). Improved flotation process control at Newcrest's Telfer operation, *Ninth Mill Operators' Conference, 19–21 March 2007*, Fremantle, Australia, pp. 87–93.

Barbian, N., Ventura-Medina, E. and Cilliers, J. J. (2003). Dynamic froth stability in froth flotation, *Minerals Engineering* **16**(11): 1111–1116.

Bascur, O. A. (2005). Example of a dynamic flotation framework, *Centenary of Flotation Symposium, 6–9 June 2005*, Brisbane, pp. 85–91.

Bascur, O. A. and Herbst, J. A. (1982). Dynamic modelling of a flotation cell with a view towards

automatic control, *XIV International Mineral Processing Conference, 17-23 October 1982*, Toronto, Canada, pp. III–11.1–III–11.22.

Bascur, O. and Herbst, J. (1985). On the development of a model-based control strategy for copper ore flotation, *in* E. Forsberg (ed.), *Flotation of Sulphide Minerals*, Elsevier, Netherlands, pp. 409–431.

Bergh, L. and Yianatos, J. (2013). Control of rougher flotation circuits aided by industrial simulator, *Journal of Process Control* **23**: 140–147.

Bergh, L. G. and Yianatos, J. B. (2011). The long way toward multivariate predictive control of flotation processes, *Journal of Process Control* **21**(2): 226–234.

Bhondayi, C. and Moys, M. H. (2014). Measurement of a proxy for froth phase bubble sizes as a function of froth depth in flotation machines Part 1. Theoretical development and testing of a new technique, *International Journal of Mineral Processing* **130**: 8–19.

Bouchard, J., Desbiens, A. and Del Villar, R. (2014). Column flotation simulation: A dynamic framework, *Minerals Engineering* **55**: 30–41.

Bouchard, J., Desbiens, A., del Villar, R. and Nunez, E. (2009). Column flotation simulation and control: An overview, *Minerals Engineering* **22**(6): 519–529.

Brooks, K. and Munalula, W. (2017). Flotation velocity and grade control using cascaded model predictive controllers, *IFAC-PapersOnLine* **50**(2): 25–30.

Coghill, P. J., Millen, M. J. and Sowerby, B. D. (2002). On-line measurement of particle size in mineral slurries, *Minerals Engineering* **15**: 83–90.

Conradie, A. v. E., Bascur, O., Aldrich, C. and Nieuwoudt, I. (2003). Integrated comminution and flotation neurocontrol using evolutionary reinforcement learning, *Application of Computers and Operations Research in the Minerals Industries, SAIMM*, pp. 209–216.

Craig, I. K. and Henning, R. G. (2000). Evaluation of advanced industrial control projects: a framework for determining economic benefits, *Control Engineering Practice* **8**(7): 769–780.

Craig, I. K. and Koch, I. (2003). Experimental design for the economic performance evaluation of industrial controllers, *Control Engineering Practice* **11**(1): 57–66.

Deglon, D. A., Egya-Mensah, D. and Franzidis, J. P. (2000). Review of hydrodynamics and gas dispersion in flotation cells on South African platinum concentrators, *Minerals Engineering* **13**(3): 235–244.

Deglon, D. A., Sawyerr, F. and O'Connor, C. T. (1999). A model to relate the flotation rate constant and the bubble surface area flux in mechanical flotation cells, *Minerals Engineering* **12**(6): 599–608.

Doyle, F. and Henson, M. (1997). Nonlinear systems theory, *in* M. Henson and D. Seborg (eds), *Nonlinear process control*, Prentice Hall, Upper Saddle River, N.J., USA, pp. 111–147.

Du Preez, N. B., Crundwell, F. K. and Knights, B. D. H. (2013). Flotation of PGM-containing minerals: Plant-wide regression and prediction of circuit performance, *Minerals Engineering* **54**: 116–123.

Farrokhpay, S., Ndlovu, B. and Bradshaw, D. (2018). Behavior of talc and mica in copper ore flotation, *Applied Clay Science* **160**: 270–275.

Finch, J. A. and Dobby, G. S. (1990). *Column Flotation*, Pergamon Press, Oxford.

Gallegos-Acevedo, P. M., Espinoza-Cuadra, J., Perez-Garibay, R. and Pecina-Trevino, E. T. (2010). Bubbles coalescence: Hydrofobic particles effect, *Journal of Mining Science* **46**(3): 333–337.

Gaudin, A. M. (1957). *Flotation*, 2nd edn, Mc Graw-Hill, New York.

Geldenhuys, S. and McFadzean, B. (2019). The effect of pulp bubble size on the dynamic froth stability measurement, *Minerals Engineering* **131**: 164–169.

Gomes-Sebastiaõ, G. A., Hearne, Z., Lam, S., Van der Spuy, D. D. V., Thompson, M. and Vines, N. (2018). Nova copper-nickel project optimisation of the copper rougher-scavenger circuit through advanced measurement and control, *14th AusIMM Mill Operators' Conference, 29–31 August 2018*, Brisbane, Australia, pp. 77–92.

Hadler, K. and Cilliers, J. J. (2009). The relationship between the peak in air recovery and flotation bank performance, *Minerals Engineering* **22**(5): 451–455.

Hadler, K., Greyling, M., Plint, N. and Cilliers, J. J. (2012). The effect of froth depth on air recovery and flotation performance, *Minerals Engineering* **36-38**: 248–253.

Hadler, K., Smith, C. and Cilliers, J. (2010a). Flotation performance improvement by air recovery optimisation on roughers and scavengers, *XXV International Mineral Processing Congress, IMPC 2010, 6–10 September 2010* **3**: 1917–1924.

Hadler, K., Smith, C. D. and Cilliers, J. J. (2010b). Recovery vs. mass pull: The link to air recovery, *Minerals Engineering* **23**(11-13): 994–1002.

Haseltine, E. L. and Rawlings, J. B. (2005). Critical evaluation of extended Kalman filtering and moving-horizon estimation, *Industrial and Engineering Chemistry Research* **44**(8): 2451–2460.

He, M., Yang, C., Wang, X., Gui, W. and Wei, L. (2013). Nonparametric density estimation of froth colour texture distribution for monitoring sulphur flotation process, *Minerals Engineering* **53**: 203–212.

Hermann, R. and Krener, A. J. (1977). Nonlinear controllability and observability, *IEEE Transactions on Automatic Control* **22**(5): 728–740.

Hernandez-Aguilar, J. R., Gomez, C. O. and Finch, J. A. (2002). A technique for the direct measurement of bubble size distributions in industrial flotation cells, *Proceedings 34th Annual Meeting of the Canadian Mineral Processors, 22–24 January 2002*, Ottawa, Canada, pp. 389–402.

Hodouin, D., Jämsä-Jounela, S.-L., Carvalho, M. T. and Bergh, L. (2001). State of the art and challenges in mineral processing control, *Control Engineering Practice* **9**(9): 995–1005.

Jämsä-Jounela, S. (1992). Simulation study of self-tuning adaptive control for rougher flotation, *Powder Technology* **69**: 33–46.

Jämsä-Jounela, S. L., Dietrich, M., Halmevaara, K. and Tiili, O. (2003). Control of pulp levels in flotation cells, *Control Engineering Practice* **11**: 73–81.

Kämpjärvi, P. and Jämsä-Jounela, S. L. (2003). Level control strategies for flotation cells, *Minerals Engineering* **16**: 1061–1068.

Kewe, T., Moffat, N. and Schaffer, M. (2014). Porgera flotation circuit upgrade and expert system installation, *12th AusIMM Mill Operators' Conference, 1–3 September 2014*, Townsville, Australia, pp. 345–355.

King, R. P. (ed.) (1982). *Principles of Flotation*, Cape and Transvaal Printers, Cape Town.

Kongas, M. (2003). Mineral slurry on-stream, *Filtration + Separation* **40**(7): 36–37.

Laurila, H., Karesvuori, J. and Tiili, O. (2002). Strategies for instrumentation and control of flotation circuits, *in* A. L. Mular, D. N. Halbe and D. J. Barratt (eds), *Mineral Processing Plant Design, Practise and Control*, Vol. 1, Society for Mining, Metallurgy, and Exploration (SME), pp. 2174–2195.

le Roux, J. D. and Craig, I. K. (2019). Plant-wide control framework for a grinding mill circuit, *Industrial and Engineering Chemistry Research* **58**(26): 11585–11600.

le Roux, J., Steinboeck, A., Kugi, A. and Craig, I. (2017). An EKF observer to estimate semi-autogenous grinding mill hold-ups, *Journal of Process Control* **51**: 27–41.

Liu, J. J. and MacGregor, J. F. (2008). Froth-based modeling and control of flotation processes, *Minerals Engineering* **21**: 642–651.

Lucia, S., Tătulea-Codrean, A., Schoppmeyer, C. and Engell, S. (2017). Rapid development of modular and sustainable nonlinear model predictive control solutions, *Control Engineering Practice* **60**: 51–62.

Lynch, A. J., Johnson, N. W., Manlapig, E. V. and Thorne, C. G. (1981). *Mineral and Coal Flotation Circuits: Their Simulation and Control*, Elsevier Scientific Publishing Company, Amsterdam.

Maldonado, M., Desbiens, A. and del Villar, R. (2009). Potential use of model predictive control for optimizing the column flotation process, *International Journal of Mineral Processing* **93**: 26–33.

Maldonado, M., Sbarbaro, D. and Lizama, E. (2007). Optimal control of a rougher flotation process based on dynamic programming, *Minerals Engineering* **20**: 221–232.

Malinga, T. L. H., Turrer, H. D. G., Nascimento, C. M., Russo, J. F. C., Gonzaga, F., Silva, J., Machado, L. C. d. R. and Sweet, J. (2018). Gas dispersion measurements as a diagnostic tool for the performance of industrial flotation cells at Minas-Rio, *19th Simpósio de Mineração, 2–4 October 2018*, São Paulo, Brazil, pp. 296–307.

Meng, J., Tabosa, E., Xie, W., Runge, K., Bradshaw, D. and Manlapig, E. (2016). A review of turbulence measurement techniques for flotation, *Minerals Engineering* **95**: 79–95.

Morar, S. H., Bradshaw, D. J. and Harris, M. C. (2012). The use of the froth surface lamellae burst rate as a flotation froth stability measurement, *Minerals Engineering* **36–38**: 152–159.

Morar, S., Hatfield, D., Barbian, N., Bradshaw, D., Cilliers, J. and Triffett, B. (2006). A comparison of flotation froth stability measurements and their use in the prediction of concentrate grade, *Proceedings of XXIII International Mineral Processing Congress, 3–8 September 2006*, Istanbul, Turkey, pp. 937–945.

Moys, M. H., Yianatos, J. and Larenas, J. (2010). Measurement of particle loading on bubbles in the flotation process, *Minerals Engineering* **23**(2): 131–136.

Naik, S. and Drunick, W. V. (2007). Anglo Research (AR) experience with integrated comminution and flotation plant modelling, *Fourth Southern African Base Metals Conference, 23-25 July 2007*, Swakopmund, Namibia, pp. 23–27.

Neethling, S. J. and Brito-Parada, P. R. (2018). Predicting flotation behaviour – The interaction between froth stability and performance, *Minerals Engineering* **120**: 60–65.

Neethling, S. J. and Cilliers, J. J. (2003). Modelling flotation froths, *International Journal of Mineral Processing* **72**(1-4): 267–287.

Neethling, S. J. and Cilliers, J. J. (2008). Predicting air recovery in flotation cells, *Minerals Engineering* **21**: 937–943.

Neethling, S. J. and Cilliers, J. J. (2009). The entrainment factor in froth flotation: Model for particle size and other operating parameter effects, *International Journal of Mineral Processing* **93**(2): 141–148.

Neethling, S. J., Lee, H. T. and Cilliers, J. J. (2003). Simple relationships for predicting the recovery of liquid from flowing foams and froths, *Minerals Engineering* **16**(11): 1123–1130.

Nesset, J. E., Hernandez-Aguilar, J. R., Acuna, C., Gomez, C. O. and Finch, J. A. (2006). Some gas dispersion characteristics of mechanical flotation machines, *Minerals Engineering* **19**(6-8): 807–815.

Oosthuizen, D. J. and Craig, I. K. (2018). Flotation modelling based on floatability distributions regressed from routine data, *IFAC-PapersOnLine* **51**(21): 105–110.

Oosthuizen, D. J. and Craig, I. K. (2019). Predicting optimal operating points by modelling different flotation mechanisms, *IFAC-PapersOnLine* **52**(14): 60–65.

Oosthuizen, D. J., Craig, I. K., Jämsä-Jounela, S. L. and Sun, B. (2017). On the current state of flotation modelling for process control, *IFAC-PapersOnLine* **50**(2): 19–24.

Oosthuizen, D. J., le Roux, J. D. and Craig, I. K. (2021). A dynamic flotation model to infer process characteristics from online measurements, *Minerals Engineering* **167**: 106878.

Phillpotts, D., Whitehead, B. and Ramatsoma, S. (2021). Monitoring of air recovery for froth flotation optimisation on an industrial circuit, *XXX International Mineral Processing Congress, 18–22 April 2021*, Cape Town, South Africa, pp. 3348–3357.

Polat, M. and Chander, S. (2000). First-order flotation kinetics models and methods for estimation of the true distribution of flotation rate constants, *International Journal of Mineral Processing* **58**: 145–166.

Putz, E. and Cipriano, A. (2015). Hybrid model predictive control for flotation plants, *Minerals Engineering* **70**: 26–35.

Qin, S. J. and Badgwell, T. A. (2003). A survey of industrial model predictive control technology, *Control Engineering Practice* **11**: 733–764.

Quintanilla, P., Neethling, S. J. and Brito-Parada, P. R. (2021). Modelling for froth flotation control: A review, *Minerals Engineering* **162**: 106718.

Rahman, R. M., Ata, S. and Jameson, G. J. (2013). Froth recovery measurements in an industrial flotation cell, *Minerals Engineering* **53**: 193–202.

Rao, C. V. and Rawlings, J. B. (2002). Constrained process monitoring: Moving-horizon approach, *AIChE Journal* **48**(1): 97–109.

Remes, A., Kongas, M., Saloheimo, K. and Jämsä-Jounela, S. L. (2005). Economical effects of on-line elemental analysis performance on flotation control, *IFAC Proceedings Volumes* **38**(1): 235–240.

Runge, K. and Franzidis, J. P. (2003). Structuring a flotation model for robust prediction of flotation circuit performance, *Proceedings of the XXII International Mineral Processing Congress, 29 September - 3 October 2003*, Cape Town, South Africa, pp. 973–984.

Safari, M. and Deglon, D. (2018). An attachment-detachment kinetic model for the effect of energy input on flotation, *Minerals Engineering* **117**: 8–13.

Saffy, M., Mashakane, T. and Hopstadius, P. (2019). Control and optimisation of a gold milling and flotation circuit, *World Gold Conference, 11–13 September 2019*, Perth, Australia.

Savassi, N., Alexander, D. J. and Johnson, N. W. (1997). Measurement of froth recovery of attached particles in industrial flotation cells, *AusIMM Sixth Mill Operators' Conference, 6–8 October 1997*, Madang, Papua New Guinea, pp. 149–155.

Savassi, O. N. (2005). A compartment model for the mass transfer inside a conventional flotation cell, *International Journal of Mineral Processing* **77**: 65–79.

Schubert, J., Henning, R., Hulbert, D. and Craig, I. (1995). Flotation control - A multivariable stabilizer, *Proceedings of the XIX International Mineral Processing Congress, 22–27 October 1995*, San Francisco, United States of America, pp. 237–241.

Schwarz, S., Alexander, D., Whiten, W., Franzidis, J.-P. and Harris, M. (2006). Jksimfloat v6: Improving flotation circuit performance and understanding, *Proceedings of the XXIII International Mineral Processing Congress, 3–8 September 2006*, Istanbul, Turkey, pp. 1717–1722.

Seborg, D. E., Edgar, T. F. and Mellichamp, D. A. (1989). *Process Dynamics and Control*, John Wiley & Sons, New York, pp. 195–196.

Seguel, F., Soto, I., Krommenacker, N., Maldonado, M. and Becerra Yoma, N. (2015). Optimizing flotation bank performance through froth depth profiling: Revisited, *Minerals Engineering* **77**: 179–184.

Shean, B., Hadler, K. and Cilliers, J. J. (2017). A flotation control system to optimise performance using peak air recovery, *Chemical Engineering Research and Design* **117**: 57–65.

Shean, B. J. and Cilliers, J. J. (2011). A review of froth flotation control, *International Journal of Mineral Processing* **100**(3-4): 57–71.

Simon, D. (2006). *Optimal State Estimation: Kalman, H Infinity, and Nonlinear Approaches*, Wiley-Interscience.

Singh, A., Louw, J. J. and Hulbert, D. G. (2003). Flotation stabilization and optimization, *The Journal of The South African Institute of Mining and Metallurgy* **2003**(9): 581–588.

Skogestad, S. and Postlehwaite, I. (2005). *Multivariable Feedback Control*, 2nd edn, John Wiley & Sons, Chichester, United Kingdom.

Smith, C. D., Hadler, K. and Cilliers, J. J. (2010). Flotation bank air addition and distribution for optimal performance, *Minerals Engineering* **23**(11-13): 1023–1029.

Steyn, C. and Sandrock, C. (2021). Causal model of an industrial platinum flotation circuit, *Control Engineering Practice* **109**: 104736.

Tang, J. and Tan, B. S. (1989). The effect of silica oxide particles upon stabilization of foam, *Journal of Colloid and Interface Science* **131**(2): 498–502.

Vinnett, L., Ledezma, T., Alvarez-Silva, M. and Waters, K. (2016). Gas holdup estimation in flotation machines using image techniques and superficial gas velocity, *Minerals Engineering* **96–97**: 26–32.

Vinnett, L., Yianatos, J. and Alvarez, M. (2014). Gas dispersion measurements in mechanical flotation cells : Industrial experience in Chilean concentrators, *Minerals Engineering* **57**: 12–15.

Wang, L., Peng, Y. and Runge, K. (2016). Entrainment in froth flotation: The degree of entrainment and its contributing factors, *Powder Technology* **288**: 202–211.

Wang, X., Zhou, J., Song, T., Liu, D. and Wang, Q. (2022). FlotGAIL: An operational adjustment framework for flotation circuits using generative adversarial imitation learning, *Minerals Engineering* **183**: 107598.

Wills, B. A. and Napier-Munn, T. (2006). *Mineral Processing Technology: An Introduction to the Practical Aspects of Ore Treatment and Mineral Recovery*, 7th edn, Elsevier Science & Technology Books, Amsterdam.

Xia, X. and Moog, C. H. (2003). Identifiability of nonlinear systems with application to HIV/AIDS models, *IEEE Transactions on Automatic Control* **48**(2): 330–336.

Xu, D., Chen, X., Xie, Y., Yang, C. and Gui, W. (2015). Complex networks-based texture extraction and classification method for mineral flotation froth images, *Minerals Engineering* **83**: 105–116.

Xu, D., Chen, Y., Chen, X., Xie, Y., Yang, C. and Gui, W. (2016). Multi-model soft measurement method of the froth layer thickness based on visual features, *Chemometrics and Intelligent Laboratory Systems* **154**: 112–121.

Yianatos, J. B., Moys, M. H., Contreras, F. and Villanueva, A. (2008). Froth recovery of industrial flotation cells, *Minerals Engineering* **21**(12-14): 817–825.

Zheng, X., Franzidis, J. P. and Johnson, N. W. (2006). An evaluation of different models of water recovery in flotation, *Minerals Engineering* **19**(9): 871–882.

Zhu, J., Gui, W., Liu, J., Xu, H. and Yang, C. (2016). Combined fuzzy based feedforward and bubble size distribution based feedback control for reagent dosage in copper roughing process, *Journal of Process Control* **39**: 50–63.

Zhu, J., Gui, W., Yang, C., Xu, H. and Wang, X. (2014). Probability density function of bubble size based reagent dosage predictive control for copper roughing flotation, *Control Engineering Practice* **29**: 1–12.